地質調査研究報告

BULLETIN OF THE GEOLOGICAL SURVEY OF JAPAN

5 mm

表紙の写真

菱刈金銀鉱山産 輝安鉱（Sb_2S_3）

　本試料は菱刈鉱山・山神鉱床の祥泉 5 脈 10 ML（坑内深度レベル）にて採取された．角柱状または
針状を示す輝安鉱は放射状またはランダムに成長し，その集合体は石英晶洞中で塊状を示した．輝安鉱
鉱化作用は，同深度で金銀鉱化作用に重複していた．本重複鉱化作用は特異な鉱化環境に起因していた
かもしれない（詳細は本文 111〜117 頁を参照のこと）．

（写真・文：清水　徹）

Cover photograph

Stibnite (Sb_2S_3) from the Hishikari gold and silver mine

　This stibnite sample was collected from Shosen 5 vein at 10 ML (mine meter level), Sanjin deposit, Hishikari mine.
Prismatic and/or acicular stibnite crystals radially or randomly grew, forming an aggregate in quartz druses. The
stibnite mineralization was overprinting Au-Ag mineralization at the same depth. The overprinting of stibnite
mineralization on Au-Ag mineralization at depth may have been due to mineralogically exceptional circumstances
(see text 111-117 pages for more information).

（Photograph and Caption by Toru Shimizu）

Article

Influence of different sedimentary environments on multi-elemental marine geochemical maps of the Pacific Ocean and Sea of Japan, Tohoku region

Atsuyuki Ohta[1,*], Noboru Imai[1], Yoshiko Tachibana[1], Ken Ikehara[1],

Hajime Katayama[1] and Takeshi Nakajima[2]

Abstract: The authors present comprehensive terrestrial and marine geochemical maps of the Tohoku region and examine how marine sedimentary environments affect the spatial distribution of elemental concentrations. Marine sediments from the Sea of Japan are relatively enriched in elements abundant in felsic igneous rocks such as K_2O, Ba, and REEs. These elements are highly enriched in sediments around submarine topographic highs, and are products of the denudation of Neogene sedimentary rocks associated with dacitic tuff and barite nodules. The silt and clay in deep basins are abundant in elements such as MnO, Cd, and Pb because of early diagenetic processes. Silty sediments on the continental shelf are supplied by large rivers; however, their geochemical features are influenced not by the adjacent terrestrial materials but simply by the effects of grain size. The sandy sediments that extensively cover the seafloor of the Pacific Ocean in the study area were sampled from depths below wave base (100–1,000 m). Their chemical compositions are homogenous and similar to those of stream sediments that originate from mafic volcanic rocks. Therefore, they are inferred to have been deposited as relict sediments under the influence of Quaternary mafic volcanic activity that have been transported from the shelf to the deep sea by gravity currents. Although 81% of the total terrestrial sediment yield is discharged into the Sea of Japan, the spatial distributions of elemental concentrations are not always continuous between land and sea. Similar findings are recognized for the Pacific Ocean side. Notably, coarse sands distributed offshore from Kamaishi are enriched in elements abundant in sedimentary rocks of the accretionary complexes and granitic rocks that crop out in adjacent terrestrial areas. Because the river system in this region is small and has low sediment yields, these coarse sands may have been produced via coastal erosion or denudation of parent rocks during past regression and transgression.

Keywords: geochemical mapping, sedimentary environment, stream sediment, marine sediment, Tohoku region, Pacific Ocean, Sea of Japan

1. Introduction

The Geological Survey of Japan has conducted research on the spatial distributions of elements across the earth's surface ("geochemical mapping") to elucidate the natural background amounts of these elements (Imai *et al.*, 2004, 2010). A geochemical map provides fundamental geo-information about the elemental cycle in the upper crust, and can be applied for environmental assessment and mineralogical exploration (e.g., Webb *et al.*, 1978; Howarth and Thornton, 1983; Weaver *et al.*, 1983). Recently, cross-boundary and sub-continental-scale geochemical mapping has been an active area of research (e.g., Reimann *et al.*, 2003; Salminen *et al.*, 2005). We conducted the first comprehensive survey of elemental distributions in both terrestrial and marine environments because Japan is surrounded by seas. Previously, we have established a procedure for multi-elemental analysis of geochemical mapping data sets (Ohta *et al.*, 2007) and proposed its application in investigating particle

---

[1] AIST, Geological Survey of Japan, Research Institute of Geology and Geoinformation

[2] AIST, Geological Survey of Japan, Research Institute for Geo-Resources and Environment

[*] Corresponding author: A. Ohta, Central 7,1-1-1 Higashi, Tsukuba, Ibaraki 305-8567, Japan. Email: a.ohta@aist.go.jp

transportation processes from land to sea and within marine environments (Ohta and Imai, 2011), as well in provenance study of marine sediments (Ohta *et al*., 2013).

In this paper, we describe terrestrial and marine geochemical maps for the Tohoku region of northern Japan. The geochemistry of marine sediments in the northeastern Sea of Japan have been studied in detail by Terashima and Katayama (1993), Terashima *et al*. (1995a, b), and Imai *et al*. (1997) as a pilot study for regional marine geochemical mapping. They discussed the geochemical features of heavy elements such as Cr, Mn, Fe, Ni, Cu, Zn, Hg, and Pb in marine sediments, but did not sufficiently examine the relationships between stream and marine sediments. The Pacific Ocean adjacent to the Tohoku region is located in a subduction zone characterized by the Japan Trench, and subduction earthquakes have occurred in this region. In particular, the major earthquake in 2011 caused a catastrophic disaster in the northern Japan. Therefore, scientific interest has been focused primarily on tsunami sediments in the coastal frontal zone and on the deep marine sediments of the Japan Trench. Sedimentation on the continental shelf and slope in the Pacific Ocean near the Tohoku region has been investigated relatively little (Iijima and Kagami, 1961; Nakajima, 1973). Furthermore, the marine environment around the Tohoku region differs considerably between the Sea of Japan and the Pacific Ocean. The Tohoku region is therefore suitable for studying the effects of different sedimentary environments on elemental concentrations. The purpose of this study is to examine how various depositional environments affect the spatial distribution patterns of elements in marine sediments.

2. Study area

2. 1 Riverine system

Figure 1 displays a schematic map of the study area with elevation and water depth. The Ou Mountain Range, with elevations ranging from 1,000 to 2,000 m, extends north–south in the northern part of the Tohoku region and separates the study area into the Pacific Ocean side and the Sea of Japan side. Sixteen major river systems exist in the study area. The potential sediment yields of these rivers are listed in Table 1 (Akimoto *et al*., 2009); 81% of the
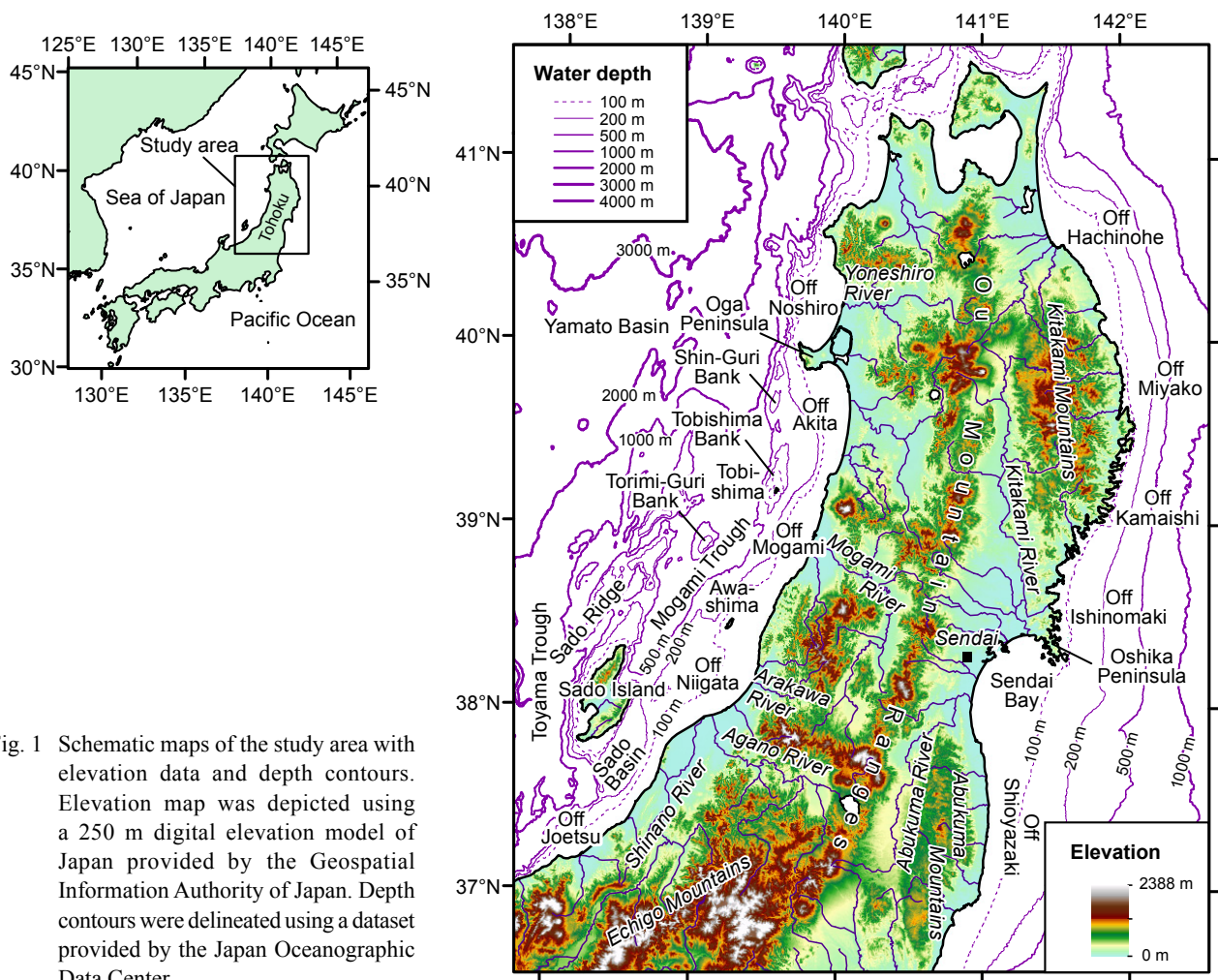

Fig. 1 Schematic maps of the study area with elevation data and depth contours. Elevation map was depicted using a 250 m digital elevation model of Japan provided by the Geospatial Information Authority of Japan. Depth contours were delineated using a dataset provided by the Japan Oceanographic Data Center.

Table 1 Sediment yield and river water discharge data for each river system of the study area.

River system	Average rate of sediment yield[a]	Drainage basin area[b]	Sediment yield	Water discharge in 2000[b]	Discharged area	Relative rate to total sediment yield
	$m^3/km^2/year$	km^2	$m^3/year$ ($\times 10^3$)	$m^3/year$ ($\times 10^6$)		
Iwaki	121	1740	211	2789	Sea of Japan	2.1%
Yoneshiro	180	2109	380	3446	Sea of Japan	3.8%
Omono	183	4035	738	8735	Sea of Japan	7.4%
Koyoshi	170	937	159	2156	Sea of Japan	1.6%
Mogami	217	6271	1361	12503	Sea of Japan	14%
Aka	248	552	137	2390	Sea of Japan	1.4%
Ara	313	905	283	640	Sea of Japan	2.8%
Agano	249	6997	1742	13188	Sea of Japan	17%
Shinano	298	9719	2896	15247	Sea of Japan	29%
Seki	324	703	228	1651	Sea of Japan	2.3%
Takase	n.d.	344	46[c]	559	Pacific Ocean	0.5%
Mabuchi	135	1751	236	1925	Pacific Ocean	2.4%
Kitakami	149	7869	1173	11688	Pacific Ocean (Sendai Bay)	12%
Naruse	106	551	58	893	Pacific Ocean (Sendai Bay)	0.6%
Natori	146	424	62	517	Pacific Ocean (Sendai Bay)	0.6%
Abukuma	136	1865	254	2127	Pacific Ocean (Sendai Bay)	2.5%

[a] Akimoto *et al*. (2009) Proceedings of Hydraulic Engineering 53, 655-660.

[b] Ministry of Land, Infrastructure, Transport and Tourism (http://www.mlit.go.jp/river/toukei_chousa/, accessed in Nov. 19, 2015)

[c] Average rate of sediment yield of Takase River is assumed to be the same as that of Mabuchi River.

total terrestrial sediment yield is discharged into the Sea of Japan. The Shinano and Agano Rivers are the largest of this region; these rivers have high sediment yields to the coast of Niigata: 29% and 17%, respectively, of the total sediment discharge of this region. In contrast, the rivers flowing to the Pacific Ocean supply only 19% of the total sediment yield of the study area. Most of these rivers flow through the Sendai Plain to Sendai Bay area.

2. 2 Geology of the terrestrial area

Figure 2 shows a geological map of northern Japan that has been simplified from the Geological Map of Japan 1:1,000,000 scale (Geological Survey of Japan, 1992). Jurassic sedimentary rocks of accretionary complexes crop out in the Kitakami Mountains, which are called the Kitakami Belt. These strata are associated with Permian–Carboniferous limestone and basalt, Carboniferous–Jurassic chert, and ultramafic rocks. Cretaceous granites were intruded into the southern Kitakami, Abukuma, and Asahi Mountains. Miocene–Pliocene granite is found in the Echigo Mountains. Cretaceous metamorphic rocks associated with Cretaceous granitic rocks are distributed in the regions of the Kitakami, Abukuma and Asahi Mountains. Mafic and felsic volcanic rocks associated with debris and pyroclastic rocks erupted mainly during the Neogene and Quaternary. A third part of the study area is covered by these volcanic rocks. Quaternary mafic volcanic and pyroclastic rocks and debris are distributed along a line to form the Ou Mountains. Neogene and Quaternary sediments are the most widely distributed units in the area; they are exposed across 40% of the study area and form wide plains in the Tohoku region. Carboniferous,

Cretaceous, Jurassic, and Paleogene sedimentary rocks are distributed in the southern Kitakami Mountains.

There are many economically important deposits mined in the study area. Kuroko-type deposits are found in the Kosaka and Hanaoka mines, which bear Cu, Pb, Zn, Au, and Ag ores. Most of these deposits occur in the watershed of the Yoneshiro River. The Oppu, Hosokura and Ohizumi mines are hydrothermal vein-type and bear Zn, Pb, and Cu. In particular, the Au mine on Sado Island mines the largest known hydrothermal vein deposit in Japan. Skarn-type deposits, like that of the Kamaishi mine that bears Fe, Cu and W, are found in granitic intrusions in the regions of the Kitakami and Abukuma Mountains.

2. 3 Coastal areas and marine geology

Figure 1 shows that the seafloor topography of the Sea of Japan is uneven, with a narrow continental shelf, submarine ridges, isolated seamounts, and deep basins. The Sado Basin, Mogami Trough, Toyama Trough, and Yamato Basin are all deep-sea basins of this sea. The Sado Ridge, Shin-Guri Bank, Tobishima Bank, and Torimi-Guri Bank are submarine topographic highs. In contrast, a gentle slope is found in the Pacific Ocean near Tohoku.

Figure 2 also shows marine geology based on the Geological Map of Japan 1:1,000,000 scale (Honza *et al*., 1978; Tamaki *et al*., 1981) and marine faults below the Sea of Japan reported by Okamura (2013). Numerous active faults lie in a NNE–SSW orientation in the Sea of Japan, where many large earthquakes have occurred (Okamura, 2010). Basement rocks in the Sea of Japan are thought to consist of Cretaceous granitic intrusions, Jurassic accretionary complexes, and Miocene to Pliocene
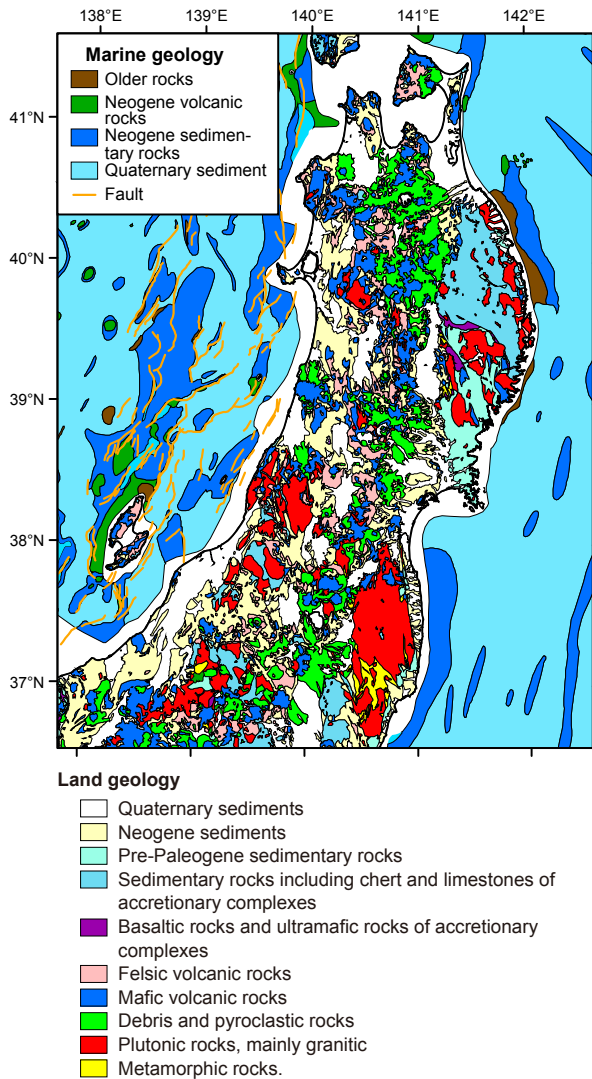
Fig. 2 Geological map of the Tohoku region of Japan, 1:1,000,000 scale (Geological Survey of Japan, 1992; Honza *et al*., 1978; Okamura, 2013; Tamaki *et al*., 1981). The older rocks of the marine geology are Paleogene, Cretaceous, and Jurassic in age (see the text).

siltstone–mudstone (Okamura *et al*., 1995a). These basement rocks form exposed topographic highs. The continental shelf and deep basins are covered with thick deposits of modern sediments.

In the Pacific Ocean, Miocene volcanic rocks are distributed on the continental shelf offshore from Hachinohe (Tamaki, 1978). Basement rocks of the continental shelf off of Hachinohe and Kamaishi are composed of Cretaceous to Paleogene sedimentary rocks (Tamaki, 1978), and offshore basement rocks are Miocene–Pleistocene sedimentary rocks containing volcanic materials (Okamura and Tanahashi, 1983). Basement rocks of the continental shelf off of Shioyazaki

are composed of Pliocene sedimentary rocks. Quaternary sediments overlie these basement rocks (Arita and Kinoshita, 1978, 1984). In contrast to the Sea of Japan, there are few active faults below this region of the Pacific Ocean.

3. Materials

Figure 3 shows the sampling locations of stream and marine sediments. A total of 798 stream sediment samples for combined geochemical mapping were collected from the Tohoku region during 1999–2002 (Imai *et al*., 2004). The mean sampling density is one sample per 100–120 km². Stream sediments were air dried and sieved with an 83 mesh (180 μm) screen. In addition, magnetic minerals were removed from the samples using a hand magnet to minimize the effect of magnetic mineral accumulation (Imai *et al*., 2004). Imai (1987) reported that fine fractions such as these have similar elemental compositions to bulk sediment samples.

First, 392 marine sediment samples were collected from the Pacific Ocean during Cruises GH81-1, GH81-2, and GH81-3 in 1981 (Arita and Kinoshita, 1978, 1984; Nishimura and Saito, 2016). An additional 405 marine sediments were collected from the Sea of Japan during Cruise GH90 in 1990 and Cruise GH91 in 1991 (Ikehara *et al*., 1994a, b; Katayama *et al*., 1994; Nakajima *et al*., 1995). Sixty additional samples were collected from the northern Tohoku region during Cruises GC06-01 and GC06-02 Cruises in 2006. These marine sediment samples were collected using a grab sampler. The uppermost 3 cm of collected sediments was separated, air dried, ground, and retained for analysis. Some samples were predominantly composed of rock fragments and gravels. In such case, we collected the sandy matrix materials.

To characterize marine sediment textures, each sampling location was assigned its own symbol according to grain size; they are classified into four categories based on the median particle diameter (φ-scale) of surface sediments. *Coarse sediments* comprise rock fragments, gravels, and very coarse, coarse and medium sands ($φ ≤ 2$); *fine sand* comprises fine and very fine sands ($2 < φ ≤ 4$); and *silt* and *clay* consist of particles with diameters of $4 < φ ≤ 8$ and $φ ≥ 8$, respectively. An additional 226 samples that were not measured for median particle diameter are classified based on textures identified through visual inspection conducted onboard the research vessel. Figure 3 shows that samples collected from the Pacific Ocean are composed mainly of sandy sediments. Coarse sands are predominantly distributed on the continental shelf off of Hachinohe and in the southern part of Sendai Bay. Silt is deposited in Sendai Bay, in the region offshore from Ishinomaki and Shioyazaki, and on the deep continental slope (>500 m). In contrast, more than half of the samples from the Sea of Japan are composed of clay. Silt and clay samples were collected from deep-sea basins, particularly from the continental shelf off of Niigata and Akita. Sandy
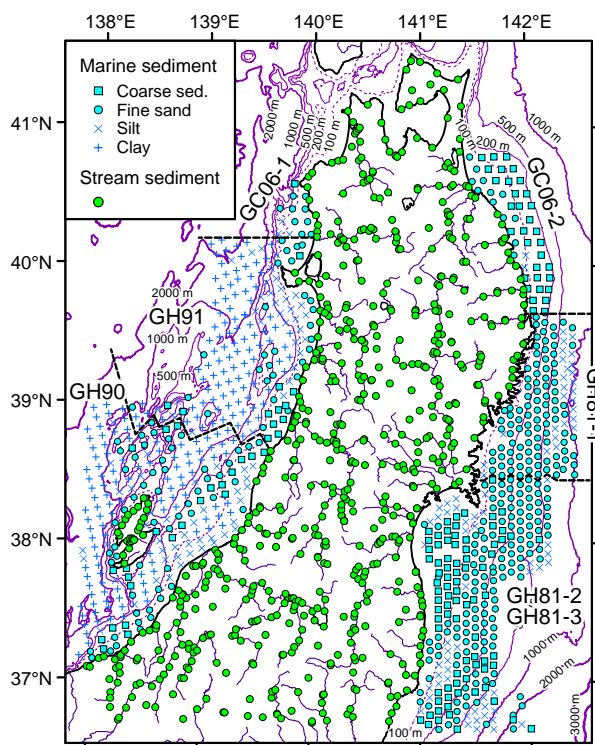
Fig. 3 Sampling locations of stream and marine sediments.

sediments from the Sea of Japan were collected from the continental shelf and submarine topographic highs.

4. Methodology

The analytical methods and quality control of the geochemical data have been described by Imai (1990), Ujiie-Mikoshiba *et al*. (2006), and Ohta *et al*. (2013). Each sample was digested for 2 h using a mixed solution of HF, HNO$_3$ and HClO$_4$ at 120°C. The degraded product was evaporated to dryness at 200°C; the residue was then dissolved in 100 mL of 0.35 M HNO$_3$ solution. The concentrations of 53 elements were determined using ICP-AES (major elements, V, Sr, and Ba) and ICP-MS (minor elements) (Imai *et al*., 2004, 2010). Analyses of the As contents of all samples and Hg content of stream sediment and marine sediment samples from the Sea of Japan were subcontracted to ALS Chemex in Vancouver, B.C. Levels of Hg in marine sediments from the Pacific Ocean were determined using an atomic absorption spectrometer. A portion of the geochemical data reported in pilot studies (e.g., the Hg data of Terashima *et al*., 1995a) was used for nationwide marine geochemical mapping. In this study, the V, Co, and Zn data of Imai *et al*. (1997) and Terashima *et al*. (1995b) were also used for the analysis. Table 2 summarizes of the analytical results obtained for marine and stream sediments. Data for Na$_2$O content in marine sediments are only advisory because marine sediments

were not desalinated. Zr and Hf data are excluded because of unsatisfactory digestion of minerals that host Zr and Hf using the HF, HNO$_3$ and HClO$_4$ solution.

The spatial distribution patterns of elements in both terrestrial and marine environments were determined using geographic information system (GIS) software (ArcGIS 10.3; Environmental Systems Research Institute, Inc.) after Ohta and Imai (2011). Class selection of elemental concentrations was conducted separately for terrestrial and marine environments because these environments differ in chemical and mineralogical compositions, particle size, and origins (Ohta and Imai, 2011). Percentiles are used for class selections for the elemental concentration intervals used in maps, i.e., the 5th, 10th, 25th, 50th, 75th, 90th, and 95th percentiles (Reimann, 2005). The spatial distribution patterns of mud (silt and clay) content by weight % in marine environments were also determined using this method. Mud contents were not recorded from GH81-2, GH81-3, GC06-01, and CG06-02; therefore, the mud contents of marine sediments off of Hachinohe and Miyako reported by Arita and Kinoshita (1978) were used to create the mud distribution map. Geochemical maps of mud content and 15 elements (Al$_2$O$_3$, K$_2$O, CaO, MnO, Fe$_2$O$_3$, Cr, Cu, As, Cd, Cs, Ba, La, Yb, Pb, and U) are shown in Fig. 4.

5. Results

5. 1 Spatial distributions of elements in terrestrial areas

Sampling locations and their geography, geology and geochemical backgrounds have previously been reported by Ohta *et al*. (2011) and Ujiie-Mikoshiba *et al*. (2006). Therefore, we simply summarize these features herein. Mafic volcanic rocks are associated with elevated MgO, Al$_2$O$_3$, P$_2$O$_5$, CaO, Sc, TiO$_2$, V, MnO, Fe$_2$O$_3$, Co, Cu, Zn, and Sr concentrations in stream sediments, but with lower Li, Be, Na$_2$O, K$_2$O, Rb, Nb, Sn, Cs, Ba, Ta, Tl, Th, and U concentrations. Pyroclastic rocks and debris exert an effect similar to that of mafic volcanic rocks. For example, K$_2$O and Ba concentrations are low in the Ou Mountains covered by mafic volcanic rocks and pyroclastic rocks, but these concentrations are rather high in the western Ou Mountains where mafic and felsic volcanic rocks and Neogene sedimentary rocks are distributed. Be, Na$_2$O, K$_2$O, Ga, Rb, Nb, Sn, rare earth elements (REEs: Y and lanthanides), Ta, Tl, Th, and U are highly enriched in stream sediments collected from areas underlain by granitic rocks; especially high concentration of these elements are found in the Asahi and Echigo Mountains. Stream sediments collected from the northern Kitakami Mountains, which are covered by accretionary complexes, are abundant in Li, Be, K$_2$O, Rb, Cs, light REEs (La, Ce, Pr, Nd, and Sm), and Th. Ultramafic rock especially elevates MgO, TiO$_2$, Cr, MnO, Co, Ni and Cu concentrations in stream sediments; however, distribution of these elements is highly restricted in the southern Kitakami Mountains.

Table 2 Summary of the geochemistry of marine and stream sediments for the Tohoku region, Japan.

Element	Unit	Marine sediment ($N=857$)					Stream sediment ($N=655$)				
		Min	Median	Mean	Max	MAD	Min	Median	Mean	Max	MAD
Na$_2$O	wt%	1.08	3.12	3.34	5.62	0.46	0.61	2.19	2.19	3.87	0.32
MgO	wt%	0.67	3.28	3.34	5.99	0.68	0.71	2.75	2.99	8.85	0.70
Al$_2$O$_3$	wt%	1.05	8.73	8.74	16.8	0.98	5.55	11.2	11.1	19.4	1.59
P$_2$O$_5$	wt%	0.036	0.115	0.126	0.447	0.023	0.027	0.118	0.137	3.46	0.031
K$_2$O	wt%	0.215	1.63	1.62	2.91	0.26	0.271	1.47	1.51	3.06	0.32
CaO	wt%	0.631	2.77	3.12	39.6	1.45	0.262	2.67	2.83	8.55	0.92
TiO$_2$	wt%	0.033	0.461	0.465	1.43	0.052	0.175	0.732	0.813	4.26	0.168
MnO	wt%	0.017	0.075	0.139	2.19	0.020	0.030	0.128	0.135	0.628	0.030
Fe$_2$O$_3$	wt%	0.85	4.66	5.08	18.4	0.78	2.11	6.29	6.51	26.1	1.38
Li	mg/kg	5.70	26.5	28.0	62.1	9.25	5.78	20.9	22.0	67.9	5.27
Be	mg/kg	0.16	1.13	1.16	3.85	0.21	0.19	1.14	1.21	5.49	0.23
Sc	mg/kg	1.80	10.8	11.2	38.0	2.54	4.23	16.0	16.9	62.1	4.74
V	mg/kg	8.0	89	87	219	14	29	125	134	383	37
Cr	mg/kg	7.4	47.9	48.0	199	11.2	6.4	46.3	60.1	605	16.4
Co	mg/kg	1.0	9.0	9.4	39	1.6	3.18	14.4	15.4	43.5	4.21
Ni	mg/kg	3.98	17.3	21.2	136	6.27	2.54	16.2	22.5	277	5.99
Cu	mg/kg	2.97	14.5	17.8	57.9	6.84	3.49	24.1	33.0	523	8.42
Zn	mg/kg	10	87	87	221	15	52.0	116	145	5382	26
Ga	mg/kg	1.87	13.0	12.8	18.4	0.97	7.92	16.0	16.1	22.4	0.99
As	mg/kg	1.0	8.2	11	141	3.9	1.0	9.0	14	234	4.0
Rb	mg/kg	4.56	46.1	46.7	120	11.7	5.29	45.0	52.0	242	15.5
Sr	mg/kg	70	168	189	2089	45	51	156	163	426	38
Y	mg/kg	5.56	13.4	13.5	22.2	1.96	6.44	18.5	19.3	48.6	3.40
Nb	mg/kg	0.73	5.13	4.88	9.32	0.96	0.92	6.20	6.77	25.0	1.41
Mo	mg/kg	0.29	0.99	1.68	38.2	0.36	0.17	1.37	1.73	24.0	0.46
Cd	mg/kg	0.015	0.079	0.105	0.79	0.027	0.026	0.16	0.31	19.7	0.064
Sn	mg/kg	0.29	1.33	1.51	3.30	0.47	0.47	1.79	2.57	168	0.48
Sb	mg/kg	0.045	0.51	0.62	2.10	0.16	0.066	0.60	1.01	123	0.20
Cs	mg/kg	0.24	2.41	2.83	7.40	1.02	0.63	2.45	2.92	12.6	0.82
Ba	mg/kg	49	311	364	12500	51	142	389	390	1337	63
La	mg/kg	3.76	12.2	12.1	42.4	2.13	2.16	14.2	15.8	135	3.65
Ce	mg/kg	6.99	20.5	22.4	104	3.41	4.48	26.2	30.0	268	6.51
Pr	mg/kg	0.88	2.95	2.98	10.7	0.47	0.62	3.48	3.84	28.4	0.79
Nd	mg/kg	3.57	12.0	12.2	41.9	1.66	3.02	14.4	15.7	103	2.92
Sm	mg/kg	0.82	2.63	2.65	8.04	0.30	0.94	3.19	3.44	17.9	0.53
Eu	mg/kg	0.27	0.68	0.71	1.73	0.08	0.31	0.85	0.87	1.78	0.11
Gd	mg/kg	0.78	2.53	2.54	6.65	0.26	1.07	3.18	3.36	13.1	0.50
Tb	mg/kg	0.16	0.45	0.45	1.00	0.05	0.25	0.57	0.60	1.82	0.09
Dy	mg/kg	0.90	2.30	2.32	4.45	0.26	1.19	3.06	3.17	8.14	0.52
Ho	mg/kg	0.19	0.45	0.45	0.77	0.06	0.21	0.61	0.63	1.60	0.11
Er	mg/kg	0.50	1.33	1.34	2.15	0.18	0.60	1.83	1.89	4.72	0.32
Tm	mg/kg	0.077	0.21	0.21	0.34	0.03	0.091	0.29	0.31	0.74	0.05
Yb	mg/kg	0.47	1.33	1.34	2.13	0.19	0.55	1.85	1.92	4.75	0.32
Lu	mg/kg	0.067	0.20	0.20	0.33	0.03	0.078	0.27	0.29	0.68	0.05
Ta	mg/kg	0.004	0.41	0.40	0.74	0.10	0.015	0.50	0.56	2.25	0.13
Hg	mg/kg	0.0005	0.045	0.071	1.19	0.023	0.001	0.030	0.086	18	0.020
Tl	mg/kg	0.056	0.36	0.36	0.75	0.10	0.09	0.43	0.48	6.54	0.14
Pb	mg/kg	4.90	21.2	26.6	83.6	9.29	4.82	20.2	37.9	7594	6.43
Bi	mg/kg	0.015	0.26	0.37	1.45	0.16	0.026	0.21	0.50	87.0	0.08
Th	mg/kg	0.67	3.74	3.68	14.8	0.87	0.64	4.25	7.10	363	1.69
U	mg/kg	0.25	0.92	0.96	2.91	0.22	0.16	1.19	1.63	86.2	0.39

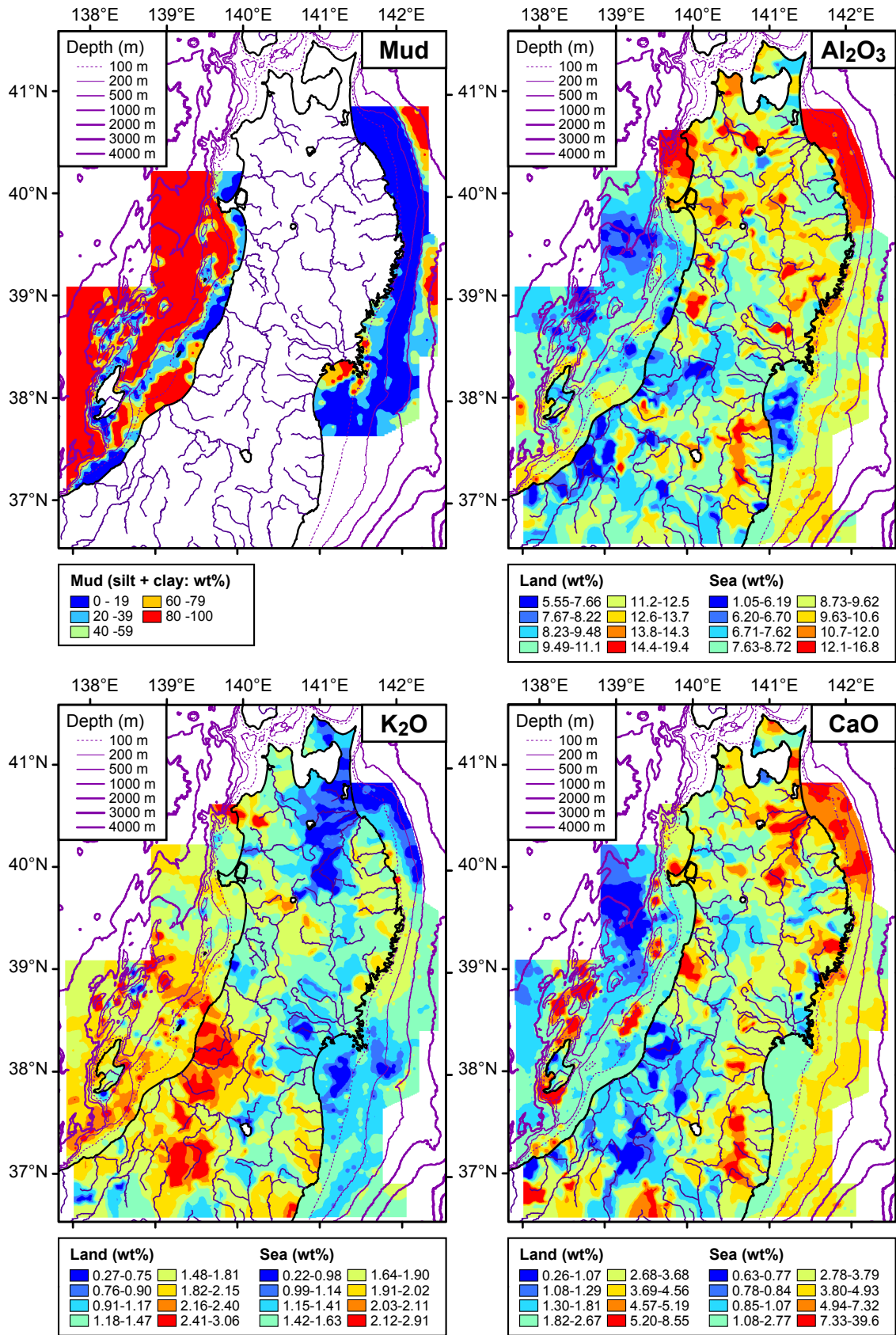Minimum (Min), maximum (Max), and median absolute deviation (MAD).

Fig. 4 Spatial distributions of mud content in marine areas and of elemental concentrations in terrestrial and marine areas for Al₂O₃, CaO, K₂O, T-Fe₂O₃, MnO, Cr, Cu, As, Cd, Cs, Ba, La, Yb, Pb, and U. Star, cross, circle, and diamond, symbols indicate major metalliferous deposits.
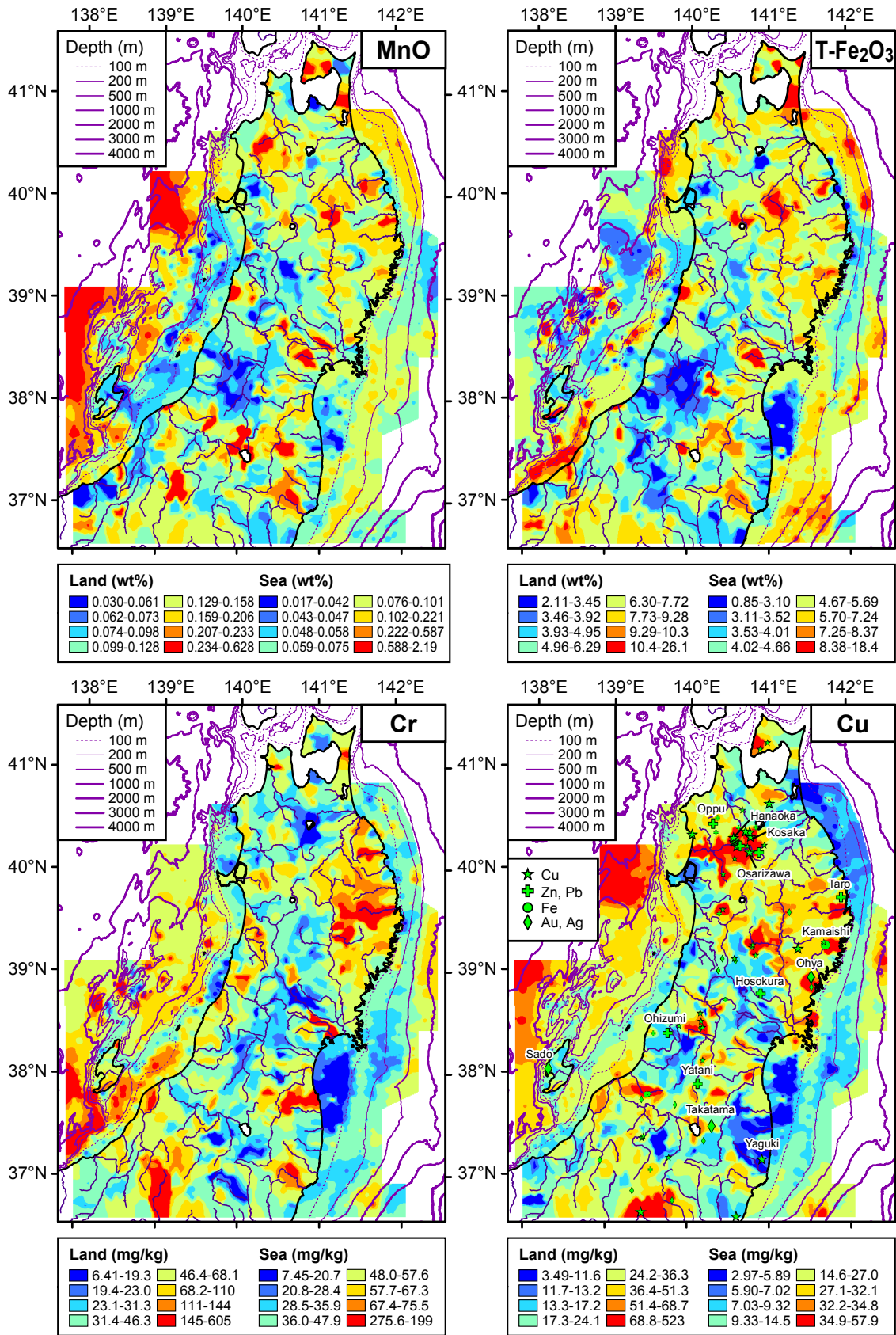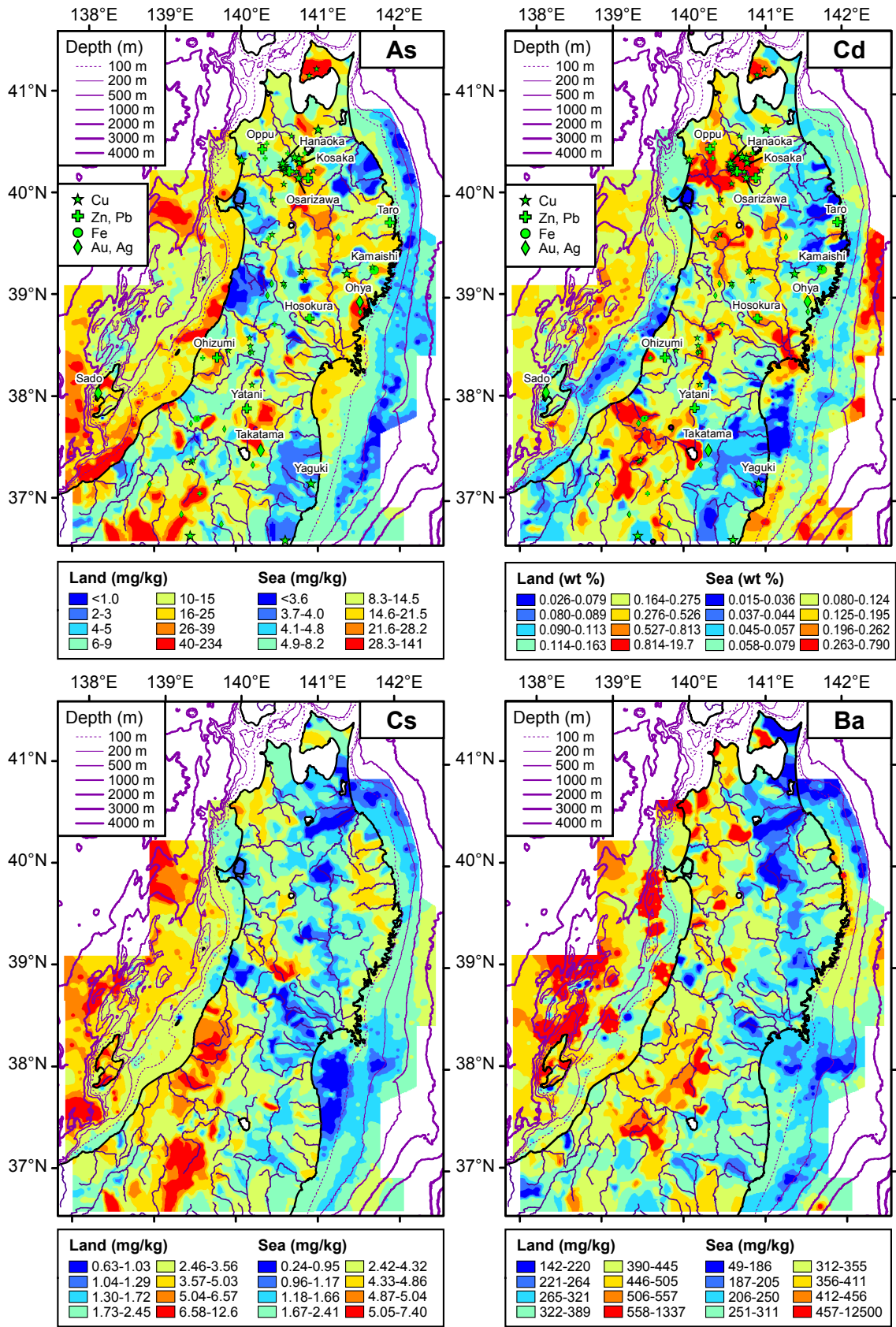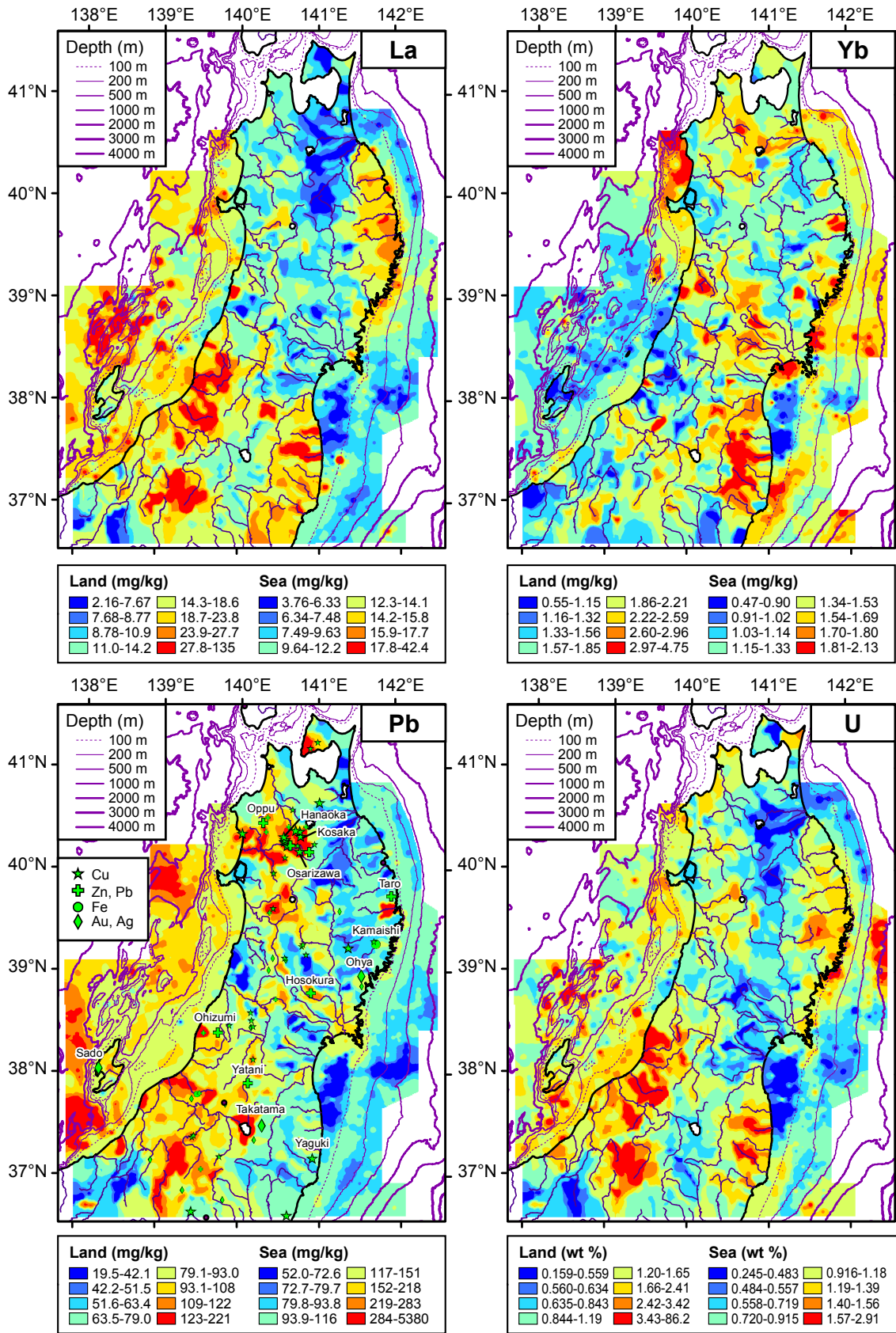
Fig. 4 Continued.

Fig. 4   Continued.

Fig. 4 Continued.

In contrast, the spatial distribution patterns of As, Cd, Sb, Hg, Pb, and Bi are strongly influenced not by geology but by mineral deposits. Certain Kuroko-type deposits, which are found at the Kosaka and Hanaoka mines within the Yoneshiro River watershed and the Taro mine in the Kitakami Mountains, greatly enhance Cu, Zn, Cd, Sb, Hg, Pb, and Bi concentrations in sediments. Skarn-type deposits, such as those of the Kamaishi and Yaoi mines, are associated with elevated Fe_2O_3 and Cu concentrations in sediments. The Au mine on Sado Island is the largest hydrothermal vein in Japan and shows elevated As concentrations in sediments. Therefore, geochemical maps in terrestrial areas are simply controlled by lithology and mineral deposits.

5. 2 Geochemical features of elemental concentrations in marine sediments

5. 2. 1 Spatial distributions of elements in marine environments

In the Pacific Ocean, MgO, Al_2O_3, CaO, Sc, TiO_2, V, MnO, Fe_2O_3, Co, Ga, and Sr are abundant in the sandy sediments on the shelf and slope off of Hachinohe. The area offshore from Kamaishi is relatively abundant in Li, Be, P_2O_5, K_2O, Cr, Ni, Rb, Y, Nb, Sb, Cs, Ba, REEs, Ta, Tl, Th, and U, although the areas of high enrichment in these elements are restricted to near the shore. Cu, Zn, As, Mo, Cd, Sn, Sb, Hg, Pb, and Bi are elevated in silt content on the shelf off of Ishinomaki. Coarse sediments on the shelf off of Shioyazaki and the southern part of Sendai Bay are depleted in all elements analyzed except for As and Ba. Silts collected from the continental slope have high concentrations of Li, V, Cr, Fe_2O_3, Ni, Cu, Zn, Nb, Mo, Cd, Sn, Sb, Cs, heavy REEs, Ta, Hg, Pb, Bi and U.

For the Sea of Japan, coarse sediments collected from the shelf and sea topographic highs are highly enriched in CaO and Sr. It is clear that these enrichments (especially in samples with CaO > 7.0 wt%) are caused by shell fragments and foraminiferal tests. Sandy sediments from the continental shelf are generally poor in almost all of the elements analyzed. However, sands on the shelf off of Noshiro are enriched in Al_2O_3, Sc, TiO_2, Fe_2O_3, Co, and heavy REEs; coarse sands on the shelf off of Mogami are abundant in As and Ba; coarse and fine sands on the edge of the shelf off of Niigata are enriched in As and Fe_2O_3; and coarse sands on the shelf off Joetsu are rich in Al_2O_3, P_2O_5, Sc, Fe_2O_3, Co, As, REEs, and Th. Silts and clays on the continental shelf off of Niigata are abundant in Li, P_2O_5, TiO_2, Cr, Ni, Cu, Nb, Cd, Sn, Cs, heavy REEs, Ta, Hg, Pb, Bi, and U. Sandy and silty sediments collected from the Sado Ridge have high concentrations of K_2O, Rb, and Cs, and especially of Be, Ba and light REEs. Clays from the Yamato Basin and the Toyama Trough are abundant in Li, MgO, P_2O_5, TiO_2, Cr, MnO, Co, Ni, Cu, As, Rb, Cs, Mo, Sn, Sb, Pb, Bi, and Tl. Thus, marine geochemical maps differ by area, and patterns are strongly associated with sediment grain sizes.

5. 2. 2 Variation of elemental concentrations in marine sediments with water depth

Figure 5 shows the mud contents and elemental concentrations of marine sediments from the Sea of Japan and the Pacific Ocean near Tohoku according to water depth. Except for the shallow water of Sendai Bay and the shelf offshore from the Niigata region, mud content in the Pacific Ocean increases gradually with water depth and steeply below 500 m, whereas mud content in the Sea of Japan increases steeply with water depth and becomes steady (90–100%) below depths of about 200–500 m. Correspondingly, changes in the elemental concentrations in sediments are similar to the systematic changes in mud content with water depth (see Cu and Cs in Fig. 5). The concentrations of many elements, such as MgO, Al_2O_3, K_2O, TiO_2, Fe_2O_3, vary greatly on the shelf (water depth (WD) = 0–200 m), but become constant below 200 m. Some elements present distinctive changes outside of this rule. Sediments collected around submarine topographic highs in the Sea of Japan (WD = 100–600 m) are abundant in Be, K_2O, Rb, Cs, Ba, and light REEs (La–Gd). The MnO, As and Mo concentrations increase steeply at depths below 500 m in the Sea of Japan (particularly the Toyama Trough and Yamato Basin). Cd, Hg and U concentrations are very high within 500–1,100 m in depth in both marine areas, but reach a constant low in deeper parts (>1,100 m) of the Sea of Japan.

6. Discussion

6. 1 Comparison of elemental abundances in stream and marine sediments between the Sea of Japan and the Pacific Ocean and with grain size

We have confirmed the geochemical features of terrestrial and marine environments of the Tohoku region using geochemical maps (Fig. 4). Figure 5 shows that the depositional or sedimentary environments systematically differ between the Sea of Japan and the Pacific Ocean. Next, we averaged the geochemical data to quantify the systematic differences in the chemical compositions of marine sediments. Figure 6 shows the median elemental concentrations of stream and marine sediments for both the Pacific Ocean and the Sea of Japan; these concentrations have been normalized to upper continental crust (UCC) values (Taylor and McLennan, 1995). The median is a robust estimation of the mean value that is less susceptible to outlier bias. Calculated median data are shown in Table 3. Stream sediments are rich in Sc, TiO_2, V, Cr, MnO, Fe_2O_3, Co, Zn, As and Sb but poor in Be, K_2O, Rb, Nb, Sn, Ta, Th, and U relative to UCC. As pointed out by Ujiie-Mikoshiba *et al.* (2006), stream sediments of the Tohoku region reflect the geochemical characteristics of igneous rocks in the orogenic arc. The UCC-normalized patterns of stream sediments on the Pacific Ocean side of Tohoku are similar to those on the Sea of Japan side. Sea of Japan sediments are somewhat abundant in K_2O, Rb, Mo, Cd, Cs, Ba, Tl, Pb, Bi, Th and U, which may be attributed to felsic
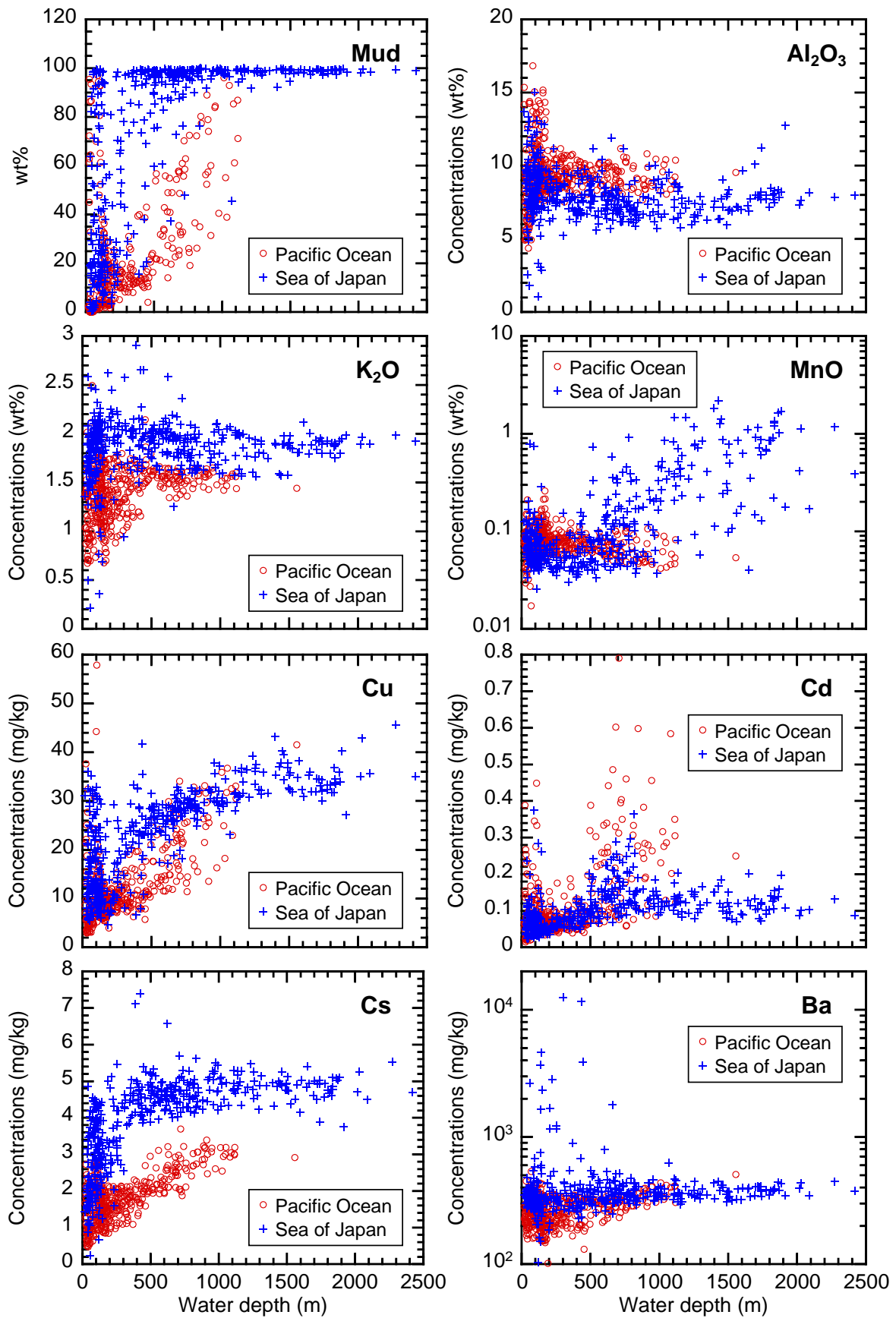
Fig. 5 Systematic change in mud contents and elemental concentrations in marine samples with changing water depth.

Table 3   Median elemental concentrations of marine and stream sediments.

| Element | Pacific Ocean | | | | | Sea of Japan | | | | | |
	Stream sed.	Marine sediment				Stream sed.	Marine sediment				
		All data	Coarse sed.	Fine sand	Silt		All data	Coarse sed.	Fine sand	Silt	Clay
	N=309	*N=439*	*N=115*	*N=249*	*N=75*	*N=346*	*N=418*	*N=36*	*N=92*	*N=79*	*N=211*
%											
Na_2O	2.21	2.95	2.67	2.96	3.50	2.17	3.65	2.54	2.84	3.30	4.38
MgO	3.00	2.78	2.80	2.74	2.86	2.50	4.07	2.97	3.62	3.87	4.24
Al_2O_3	11.5	9.23	9.32	9.31	9.04	10.4	7.84	7.18	8.83	8.31	7.60
P_2O_5	0.11	0.098	0.090	0.097	0.12	0.12	0.14	0.11	0.12	0.14	0.16
K_2O	1.32	1.44	1.19	1.48	1.56	1.67	1.90	1.64	1.92	1.93	1.90
CaO	3.12	3.57	3.83	3.66	2.80	2.24	1.06	3.12	2.33	1.16	0.88
TiO_2	0.77	0.46	0.43	0.46	0.46	0.67	0.47	0.31	0.46	0.52	0.46
MnO	0.14	0.076	0.085	0.077	0.059	0.12	0.072	0.071	0.066	0.057	0.12
Fe_2O_3	6.80	5.01	5.31	4.97	4.92	5.63	4.44	3.96	5.84	5.00	4.17
mg/kg											
Li	20	19	16	19	28	22	38	24	30	38	40
Be	1.1	0.97	0.80	1.0	1.1	1.2	1.4	1.0	1.4	1.4	1.3
Sc	19	13	14	13	12	12	8.5	6.1	9.9	9.7	8.0
V	137	81	74	81	90	108	99	56	83	96	102
Cr	47	38	32	39	50	45	55	30	46	54	58
Co	16	8.3	9.1	8.2	7.5	12	10	6.0	10	11	9.0
Ni	16	14	11	14	21	16	28	14	16	23	31
Cu	26	10	7.1	10	23	23	26	9.0	12	22	30
Zn	110	75	68	72	94	124	99	64	87	107	102
Ga	16	12	12	13	13	16	14	11	13	15	14
As	10	4.9	5.6	4.6	5.6	8.9	14	21	14	15	13
Rb	41	36	29	37	44	55	57	52	56	56	58
Sr	164	198	196	205	162	146	123	209	172	123	109
Y	19	15	13	15	16	17	12	11	15	13	12
Nb	6.1	4.2	3.1	4.3	5.5	6.2	5.7	3.4	5.1	6.1	5.8
Mo	1.3	0.81	0.76	0.72	1.3	1.5	1.3	0.76	0.89	1.1	1.9
Cd	0.13	0.072	0.065	0.066	0.22	0.20	0.093	0.041	0.054	0.079	0.12
Sn	1.7	1.0	0.80	1.0	1.4	1.9	2.1	1.2	1.4	2.2	2.3
Sb	0.59	0.42	0.37	0.43	0.71	0.60	0.70	0.45	0.50	0.53	0.96
Cs	2.2	1.8	1.2	1.8	2.6	2.8	4.3	1.9	2.8	3.8	4.8
Ba	348	260	211	276	287	423	344	317	343	328	352
La	13	9.8	7.7	10	12	14	14	12	15	14	14
Ce	26	19	16	19	21	26	23	23	31	26	20
Pr	3.4	2.5	2.0	2.6	2.9	3.5	3.3	2.7	3.7	3.5	3.2
Nd	14	11	8.6	11	12	14	13	11	15	14	13
Sm	3.3	2.4	2.1	2.5	2.7	3.1	2.8	2.3	3.2	3.1	2.7
Eu	0.88	0.72	0.70	0.74	0.68	0.82	0.64	0.59	0.81	0.68	0.60
Gd	3.3	2.4	2.1	2.4	2.6	3.0	2.6	2.1	3.0	2.8	2.6
Tb	0.60	0.44	0.39	0.44	0.49	0.55	0.45	0.36	0.51	0.49	0.43
Dy	3.2	2.4	2.1	2.4	2.6	2.9	2.2	1.8	2.6	2.5	2.2
Ho	0.64	0.48	0.42	0.48	0.52	0.57	0.42	0.34	0.50	0.47	0.40
Er	1.9	1.4	1.3	1.4	1.6	1.7	1.2	1.0	1.5	1.4	1.2
Tm	0.31	0.23	0.20	0.23	0.26	0.28	0.19	0.16	0.23	0.22	0.19
Yb	1.9	1.4	1.3	1.5	1.6	1.7	1.2	0.95	1.4	1.4	1.2
Lu	0.29	0.22	0.19	0.22	0.25	0.26	0.18	0.14	0.20	0.20	0.17
Ta	0.49	0.33	0.24	0.33	0.44	0.49	0.50	0.31	0.41	0.54	0.52
Hg	0.030	0.047	0.027	0.047	0.11	0.030	0.040	0.030	0.045	0.080	0.040
Tl	0.35	0.28	0.21	0.29	0.32	0.51	0.45	0.34	0.37	0.45	0.47
Pb	17	15	13	14	18	26	39	24	28	35	45
Bi	0.19	0.14	0.090	0.14	0.26	0.24	0.62	0.27	0.30	0.55	0.73
Th	3.7	2.8	1.9	2.9	3.6	4.6	4.3	3.8	4.6	5.0	4.1
U	1.1	0.78	0.61	0.78	1.2	1.3	1.1	0.87	1.2	1.2	0.97
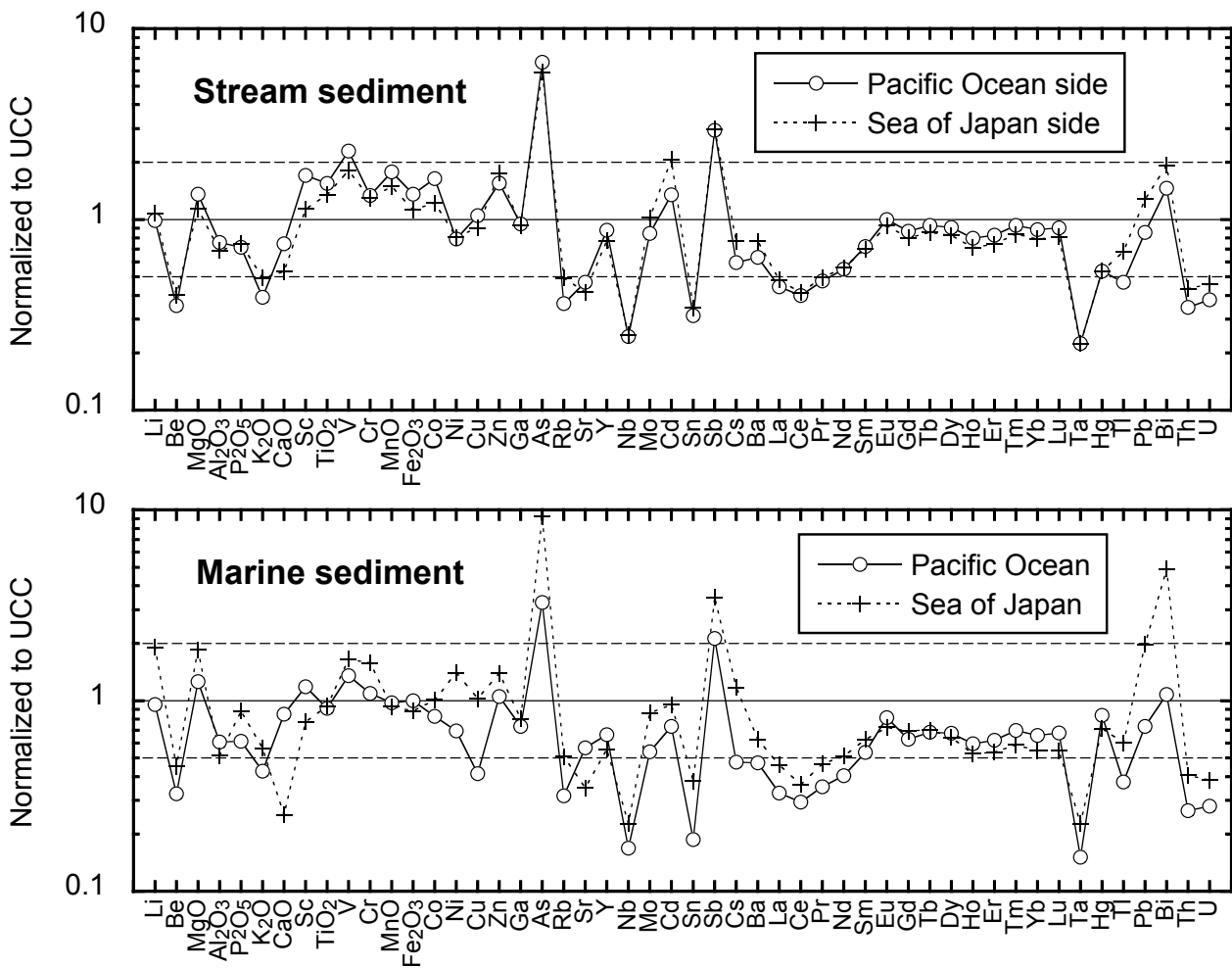
Fig. 6 Chemical compositions of stream sediments and marine sediments normalized to the upper continental crust.

igneous rocks and metalliferous deposits associated with Neogene felsic volcanic rocks. UCC-normalized values for marine sediments are systematically lower than those of stream sediments, although they have fundamentally similar geochemical features. Marine sediments of the Sea of Japan are relatively abundant in Li, MgO, P_2O_5, K_2O, Cr, Ni, Cu, Zn, As, Rb, Mo, Sn, Cs, Ba, light REEs, Tl, Pb, Bi, Th and U, but scarce in CaO, Sc, and Sr compared to those of the Pacific Ocean.

Figure 7 shows the median elemental concentrations of marine sediments according to grain size and region, normalized to those of stream sediments. The classification of grain size is the same as that used in Fig. 3. Median data for grain sizes and regions are also summarized in Table 3. In the Pacific Ocean, MgO, Al_2O_3, CaO, Sc, TiO_2, V, Fe_2O_3, Ga, and Eu concentrations are similar, whereas the concentrations of other elements, especially Li, Cu, Cd, Cs, Hg, and Bi, increase with decreasing grain size. In the Sea of Japan, many elemental concentrations increase with decreasing grain size. There are no systematic changes in K_2O, Rb, and Ba concentrations. Al_2O_3, Fe_2O_3,

Ga, REEs, Th, and U concentrations are high in fine sand and silt but low in coarse sediment and clay. Arsenic is highly abundant in coarse sediment, and MnO is highly enriched in clay. CaO and Sr concentrations decrease systematically with decreasing grain size. In summary, geochemical differences in marine sediments between the Pacific Ocean and the Sea of Japan are larger than those in stream sediments. Furthermore, chemical compositions of marine sediments change systematically with grain size.

6. 2 Two-way ANOVA applied to quantitatively assess factors controlling elemental concentrations in marine sediments

The regional geochemical differences identified in marine sediments are inferred to be caused by factors such as differing amounts of terrestrial sediment discharge to the coast, denudation of local marine basement rocks, and the occurrence of relict sediments. Geochemical variations in sediment with grain size may indicate the effects of dilution with quartz and calcareous materials, the enhancement of heavy elements through early
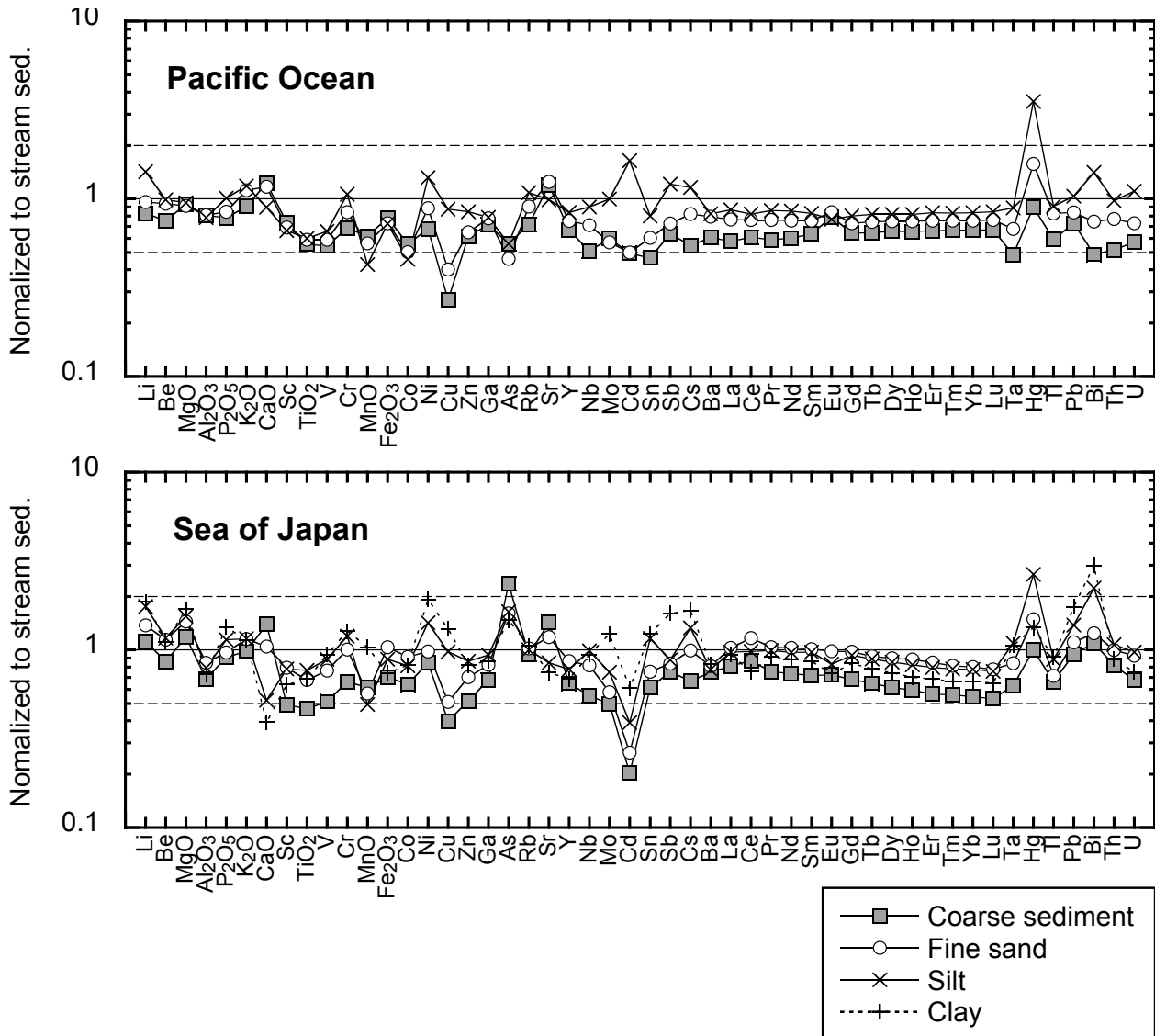
Fig. 7 Chemical variations of coarse sediments, fine sands, silts and clays in marine sediments normalized to the adjacent terrestrial sediments.

diagenetic process, increasing clay contents. Next, we have investigated which controlling factor is dominant for each element using two-way analysis of variance (ANOVA).

For this process, we closely followed the methods described by Ohta *et al*. (2007). The Ekuseru-Toukei 7.0 software (ESUMI Corp. Ltd.) was used for statistical analysis. We generally assumed that geochemical data followed either normal distribution or log-normal distribution. However, geochemical data do not strictly follow either of these distribution patterns in most cases (Ohta *et al*., 2007). Therefore, as a second approach, data with a symmetrical distribution were used for ANOVA, i.e., data sets with data skewness close to zero were used. Table 4 shows the skewness of our geochemical data and the format of these data used for ANOVA. Samples were

classified into seven sub-groups, as shown in Table 3: coarse sediments, fine sand, and silt in the Pacific Ocean; and coarse sediments, fine sand, silt, and clay in the Sea of Japan. Unfortunately, clay was not found in appreciable amounts in the Pacific Ocean; therefore, ANOVA provides only semi-quantitative results. Nonetheless, the findings obtained through ANOVA are informative.

Table 5 shows the variance ratios (F), probabilities (p), and the size effects (η^2) of regional differences (factor A), grain size (factor B), and the interaction effects (factor A $\times$ factor B), which were estimated through two-way ANOVA. When the p value is lower than 0.01, we conclude that the effect of that factor is significant. However, Table 4 demonstrates that in most cases, each factor is statistically significant ($p < 0.01$). This finding can be attributed to very small difference detected to be

Table 4 Skewness of unchanged and log-transformed data.

Element	Skewness		Data transformation for ANOVA
	Raw	Log	
MgO	−0.26	−1.52	Unchanged
Al_2O_3	0.52	−1.71	Unchanged
P_2O_5	1.79	0.24	Log-transformed
K_2O	−0.35	−1.62	Unchanged
CaO	5.85	0.29	Log-transformed
TiO_2	1.18	−1.95	Unchanged
MnO	4.57	1.91	Log-transformed
Fe_2O_3	2.04	−0.15	Log-transformed
Li	0.21	−0.34	Unchanged
Be	1.93	−0.46	Log-transformed
Sc	1.31	−0.43	Log-transformed
V	−0.09	−2.11	Unchanged
Cr	1.80	−0.82	Log-transformed
Co	1.64	−1.52	Log-transformed
Ni	2.62	0.07	Log-transformed
Cu	0.55	−0.18	Log-transformed
Zn	−0.84	−1.23	Unchanged
Ga	−1.37	−3.82	Unchanged
As	4.21	0.42	Log-transformed
Rb	0.40	−0.81	Unchanged
Sr	7.37	1.41	Log-transformed
Y	0.14	−0.49	Unchanged
Nb	−0.4	−1.61	Unchanged
Mo	6.77	1.35	Log-transformed
Cd	2.92	0.50	Log-transformed
Sn	0.47	−0.31	Log-transformed
Sb	1.21	0.07	Log-transformed
Cs	0.38	−0.41	Unchanged
Ba	15.47	2.93	Log-transformed
La	2.21	−0.18	Log-transformed
Ce	3.47	0.57	Log-transformed
Pr	2.36	−0.18	Log-transformed
Nd	2.44	−0.17	Log-transformed
Sm	2.13	−0.29	Log-transformed
Eu	2.01	0.54	Log-transformed
Gd	1.55	−0.47	Log-transformed
Tb	0.90	−0.59	Log-transformed
Dy	0.38	−0.65	Unchanged
Ho	0.17	−0.57	Unchanged
Er	0.09	−0.57	Unchanged
Tm	0.09	−0.53	Unchanged
Yb	0.08	−0.53	Unchanged
Lu	0.05	−0.56	Unchanged
Ta	−0.29	−3.4	Unchanged
Hg	5.42	−0.16	Log-transformed
Tl	−0.09	−0.93	Unchanged
Pb	0.64	−0.03	Log-transformed
Bi	0.96	−0.41	Log-transformed
Th	1.16	−0.75	Log-transformed
U	0.97	−0.3	Log-transformed

significant in the case of a large sample size ($N = 857$). In such cases, η^2 can be used for a plausible estimate of the p value irrespective of the number of samples (Richardson, 2011; Fritz *et al*., 2012). In this study, we conclude that 1) a factor with $\eta^2 \geq 0.06$ has a significant influence on changes in chemical compositions, and 2) a factor with a higher η^2 score indicates a more significant effect on chemical compositions (Fritz *et al*., 2012).

The "interaction effect" refers to the effect of one factor on another factor, i.e., the two factors affect the data synergistically. The η^2 score of the interaction effect is lower than 0.06 for the entire data set (Table 5). It is therefore concluded that these factors affect the chemical compositions of sediments independently. ANOVA also suggests that 1) the grain size effect is significant for almost all elements except for Al_2O_3, TiO_2, Sc, Co, As, Rb, and Ba in marine sediments, and 2) grain size has stronger influence on the concentrations of 33 elements than do regional differences. The regional difference effect is significant for 25 elements, but only 14 elements, such as MgO and K_2O, are more dominantly affected by regional differences than by grain size. Consequently, the ANOVA results caution that grain size obscures geochemical information of sediment origin in most cases. Therefore, we have divided the study area into regions in which marine sediments are roughly similar in terms of grain size to elucidate the processes of particle transport from land to sea and the influence of local marine geology.

6.3 Geochemical features of marine sediments in the Pacific Ocean
6.3.1 Influence of local marine geology on marine geochemical maps

Coarse sands distributed on the continental shelf off of Hachinohe are highly abundant in elements that are enriched in mafic volcanic rocks such as Al_2O_3, CaO, MnO, and Fe_2O_3, and scarce in elements enriched in felsic igneous rocks such as K_2O, Rb, Cs, Ba, REEs, and Th. In contrast, in the Sea of Japan, coarse sediments are relatively depleted in many elements, except for CaO, Sr and As (Fig. 7). Small rivers flow to the coastline of the Hachinohe area. Furthermore, most coarse sediments were collected from depths below wave base. Water movement, such as fair-weather and storm waves and coastal current, is able to move sandy sediments at water depths of less than 50–80 m (Saito, 1989). Therefore, the transport processes of modern sediments from land to sea are not the cause of the enrichment of the above-mentioned elements. Arita and Kinoshita (1978) and Nishimura and Saito (2016) reported that the sandy sediments of the Pacific Ocean contain large amounts of volcanic rock fragments and heavy minerals such as augite, hypersthene and hornblende. In fact, the marine geological map shows that Miocene volcanic rocks are exposed in the region offshore from Hachinohe (Fig. 2). Therefore, we assume that these coarse sands were produced by the denudation of Miocene volcanic rocks on the continental shelf off of

Table 5　Variance ratios (F), probabilities (p), and size effects (η^2) of two-way ANOVA applied to the unchanged and log-transformed data.

Element	F			p			η^2			Dominant factor
	A	B	A×B	A	B	A×B	A	B	A×B	
MgO	302	44	5	<0.01	<0.01	<0.01	**0.154**	**0.068**	0.008	Regional
Al$_2$O$_3$	48	11	11	<0.01	<0.01	<0.01	0.045	0.030	0.032	none
P$_2$O$_5$	105	84	2	<0.01	<0.01	0.15	**0.061**	**0.146**	0.003	Grain size
K$_2$O	372	48	2	<0.01	<0.01	0.13	**0.217**	**0.084**	0.003	Regional
CaO	75	189	19	<0.01	<0.01	<0.01	0.032	**0.243**	0.025	Grain size
TiO$_2$	<1	14	13	0.44	<0.01	<0.01	0.001	0.046	0.041	none
MnO	<1	52	0.7	0.74	<0.01	0.56	0.000	**0.147**	0.002	Grain size
Fe$_2$O$_3$	5	32	15	0.03	<0.01	<0.01	0.005	**0.096**	0.045	Grain size
Li	418	270	3	<0.01	<0.01	0.05	**0.111**	**0.216**	0.002	Grain size
Be	383	81	9	<0.01	<0.01	<0.01	**0.207**	**0.131**	0.014	Regional
Sc	200	23	19	<0.01	<0.01	<0.01	**0.142**	0.049	0.041	Regional
V	1	44	3	0.34	<0.01	0.05	0.001	**0.123**	0.007	Grain size
Cr	22	113	1	<0.01	<0.01	0.22	0.020	**0.231**	0.004	Grain size
Co	105	3	8	<0.01	0.03	<0.01	**0.098**	0.009	0.022	Regional
Ni	56	214	2	<0.01	<0.01	0.13	0.025	**0.284**	0.003	Grain size
Cu	15	443	4	<0.01	<0.01	0.01	0.005	**0.436**	0.004	Grain size
Zn	40	103	13	<0.01	<0.01	<0.01	0.028	**0.216**	0.028	Grain size
Ga	14	88	25	<0.01	<0.01	<0.01	0.010	**0.198**	0.057	Grain size
As	694	16	4	<0.01	<0.01	<0.01	**0.363**	0.025	0.007	Regional
Rb	299	19	5	<0.01	<0.01	<0.01	**0.194**	0.036	0.009	Regional
Sr	2	104	15	0.21	<0.01	<0.01	0.001	**0.218**	0.031	Grain size
Y	15	80	10	<0.01	<0.01	<0.01	0.012	**0.200**	0.024	Grain size
Nb	34	177	1	<0.01	<0.01	0.22	0.020	**0.315**	0.003	Grain size
Mo	8	81	<1	<0.01	<0.01	0.44	0.006	**0.181**	0.002	Grain size
Cd	128	189	27	<0.01	<0.01	<0.01	**0.085**	**0.378**	0.055	Grain size
Sn	249	331	<1	<0.01	<0.01	0.77	**0.086**	**0.277**	0.001	Grain size
Sb	0.03	109	11	0.87	<0.01	<0.01	0.000	**0.233**	0.023	Grain size
Cs	428	328	3	<0.01	<0.01	0.02	**0.100**	**0.230**	0.002	Grain size
Ba	129	18	3	<0.01	<0.01	0.04	**0.116**	0.048	0.007	Regional
La	342	66	7	<0.01	<0.01	<0.01	**0.210**	**0.122**	0.013	Regional
Ce	329	90	10	<0.01	<0.01	<0.01	**0.238**	**0.195**	0.022	Regional
Pr	339	82	7	<0.01	<0.01	<0.01	**0.208**	**0.151**	0.013	Regional
Nd	299	87	7	<0.01	<0.01	<0.01	**0.192**	**0.168**	0.014	Regional
Sm	207	96	7	<0.01	<0.01	<0.01	**0.144**	**0.201**	0.015	Grain size
Eu	11	91	17	<0.01	<0.01	<0.01	0.009	**0.225**	0.042	Grain size
Gd	126	92	7	<0.01	<0.01	<0.01	**0.097**	**0.213**	0.017	Grain size
Tb	45	96	8	<0.01	<0.01	<0.01	0.037	**0.238**	0.021	Grain size
Dy	12	87	10	<0.01	<0.01	<0.01	0.010	**0.230**	0.026	Grain size
Ho	<1	87	8	0.4	<0.01	<0.01	0.001	**0.225**	0.022	Grain size
Er	14	89	8	<0.01	<0.01	<0.01	0.011	**0.220**	0.020	Grain size
Tm	34	90	7	<0.01	<0.01	<0.01	0.027	**0.214**	0.017	Grain size
Yb	52	86	7	<0.01	<0.01	<0.01	0.041	**0.202**	0.016	Grain size
Lu	87	85	6	<0.01	<0.01	<0.01	**0.065**	**0.191**	0.014	Grain size
Ta	78	139	1.3	<0.01	<0.01	0.26	0.045	**0.240**	0.002	Grain size
Hg	<1	71	2.2	0.85	<0.01	0.09	0.000	**0.198**	0.006	Grain size
Tl	183	58	4	<0.01	<0.01	0.01	**0.106**	**0.100**	0.006	Regional
Pb	937	165	2	<0.01	<0.01	0.21	**0.214**	**0.113**	0.001	Regional
Bi	448	163	2	<0.01	<0.01	0.11	**0.142**	**0.156**	0.002	Grain size
Th	314	88	5	<0.01	<0.01	<0.01	**0.184**	**0.155**	0.009	Regional
U	133	84	14	<0.01	<0.01	<0.01	**0.099**	**0.187**	0.031	Grain size

The A, B and A×B indicate the regional effect, the grain size effect, and the interaction effect, respectively.

Bold phase type means that η^2 is larger than 0.06.

Hachinohe during regression and transgression.

6. 3. 2　Particle transport from land to sea and within the marine environment in the Pacific Ocean

The distribution of silts in Sendai Bay is evidence for the input of modern sediments from rivers because major rivers that drain into the Pacific Ocean flow into Sendai Bay (Table 1). The concentrations of many elements, such as Cu, As, Cd, Yb, and Pb, in silt from Sendai Bay are higher than those in near-shore sandy sediments because of the grain size effect. Silts on the deep continental slope of the Pacific Ocean also have high concentrations of Li, Cr, Ni, Cu, Nb, Mo, Cd, Sn, Sb, Cs, Ta, Hg, Bi, and U, which can be explained by the same effect. The concentrations of many elements in silt both in Sendai Bay and on the continental slope are similar. However, the Zn, As, Hg, and Pb concentrations of silts in Sendai Bay are half as high as those of silts on the continental slope. Their enrichment may be attributed to anthropogenic activity or the supply of ore minerals from the Hosokura Mine.

The coarse sediments distributing on the continental shelf off of Shioyazaki are remarkably depleted in most elements except for As and Ba. Dilution effects caused by preferential enrichment in quartz and feldspar, which may be supplied from granitic rocks of the nearby Abukuma Mountains, may be the cause. The same phenomenon is observed on the continental shelf off of the Atsumi Peninsula of the Tokai Region (Ohta *et al.*, 2007). Quartz and feldspar generally do not become small grains because of their resistance to physical weathering processes (e.g., Goldich, 1938). Consequently, these minerals are not transported by water movement to the degree that small grains of minerals such as mica, biotite, and amphibole are, and selectively accumulate on the continental shelf. This important mineralogical fractionation obscures sediment origin information.

The spatial distributions of many elements, such as K_2O, Rb, Nb, REEs, and Th, are continuous between the Kitakami Mountains and the nearby the coast off of Kamaishi (e.g., K_2O, La, and U in Fig. 4). As explained above, marine sediments in the Pacific Ocean in this region are influenced by mafic volcanic rocks (Nishimura and Saito, 2016), which are associated with lower Li, K_2O, Rb, Cs, Ba, Nb, REEs, Ta, and Th concentrations in sediments. Therefore, the influence of sediments that originated from granitic intrusions and accretionary complexes becomes apparent. However, the rivers that flow through the Kitakami Mountains to the coast near Kamaishi are small, and their sediment yields are low. In addition, most of the marine sediments sampled were collected from water depths of 50–150 m, below wave base. Accordingly, these samples are interpreted as relict sediments that originated from coastal erosion and/or denudation of granitic rocks and accretionary complexes during regression and transgression.

The wide distribution of fine sands on the continental shelf and slope off of Kamaishi is clearly explained by the deposition of relict sediments because most of these samples were deposited below the depth of wave base and away from the shore (Fig. 3). Noda and TuZino (2007) reported that sandy sediments on the edge of the continental shelf and on the continental slope are transported gradually by a gravity to a deeper area offshore from Nemuro, Hokkaido, Japan, which results in the formation of numerous gullies on the slope. However, there are few submarine canyons in the Pacific Ocean near the Tohoku region except for in the region off of Kamaishi (Yashima *et al.*, 1982; Shimamura, 2008). Therefore, sediments may be conveyed to deeper areas via massive submarine landslides or sheet flows. Otherwise, these sediments may be produced by denudation of basement rocks such as Neogene sedimentary rocks (Fig. 2). Figure 8 shows that the median concentrations of elements in fine sands are classified with water depths, which are normalized to stream sediments on the Pacific Ocean side. We followed the convention of dividing the samples into four groups: the shelf (WD = 0–100 m), the edge of the shelf (WD = 100–200 m), the upper slope (WD = 200–500 m), and the lower slope (WD = 500–1,000 m). The shelf was an erosional region during regression and subsequently shifted to a depositional environment during transgression. The edge of the shelf was under depositional conditions even during transgression. The upper slope has thin Quaternary sediments overlying Miocene sediments (Okamura and Tanahashi, 1983). The lower slope is a deep-sea terrace. Figure 8 shows that normalized patterns of fine sediments in the Pacific Ocean are fairly consistent; their mean chemical compositions are similar to those of terrestrial areas influenced by orogenic belt volcanism, as explained above. Furthermore, no significant differences are apparent among samples; marine sediments in the Pacific Ocean have very homogenous geochemical features. Enrichment in Cr, Fe_2O_3, Cu, Cd, Sb, Cs, and Hg in sandy sediments collected from sea-floor depth of over 500 m (Fig. 3) is explained by the increase in the proportion of silts. These results suggest that fine sands were deposited on the continental shelf under the influence of volcanic activity during a regression/transgression and have been transported from the continental shelf to the deep sea by gravity currents. From geochemical mapping of the Pacific Ocean, we observe two kinds of particle transport, i.e., present and past particle transportation, from land to sea.

6. 4　Geochemical features of marine sediments in the Sea of Japan
6. 4. 1　Particle transport processes from land to marine environments in the Sea of Japan

Sediments on the continental shelf off of Noshiro are expected to be influenced by Kuroko deposits because there are many geochemical anomalies found in the watershed area of the Yoneshiro River (Cu, Cd, and Pb in Fig. 4). Fine sands in the region off of Noshiro are abundant in Al_2O_3, Sc, TiO_2, Fe_2O_3, Co, and heavy REEs,
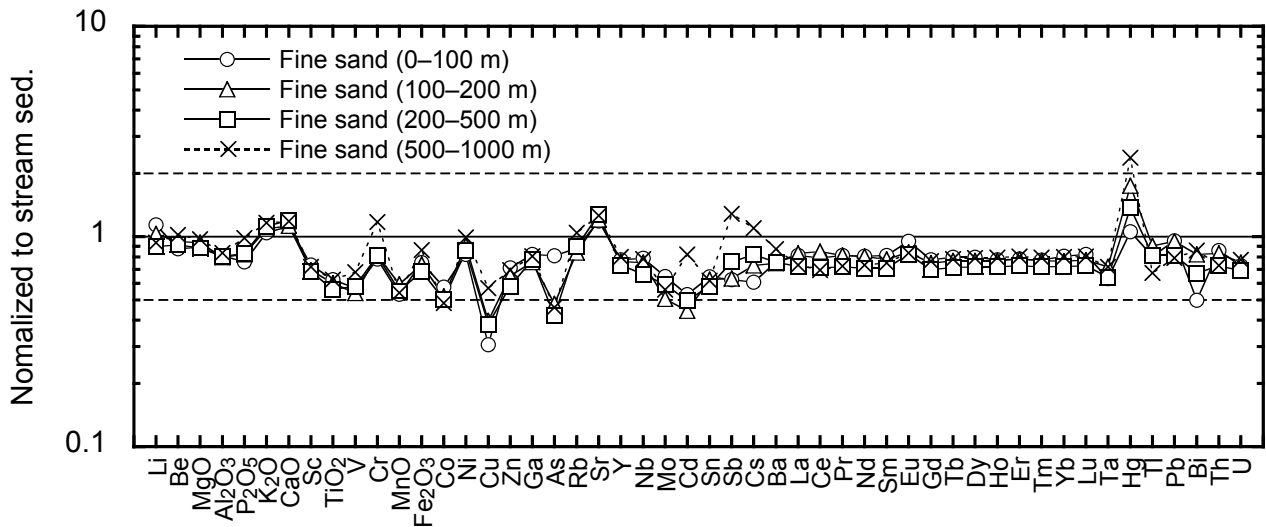
Fig. 8   Chemical variations of fine sands in the Pacific Ocean normalized to the adjacent terrestrial sediments.

but scarce in Cu, Zn, As, Cd, Sb, Pb, and Bi. Ohta *et al.* (2010) have discussed the transport processes of mining ores from the Kuroko deposits in the Yoneshiro River watershed to the coast. They concluded that sulfide ores have been oxidized and are releasing heavy metals during weathering and transportation. Based on those results, fine sands in the region offshore from Noshiro are inferred to have originated from mafic volcanic rocks in the northern Tohoku region and scarcely contain mining ores.

Silts and clays on the continental shelf off of Niigata are modern sediments supplied primarily by the Shinano and Agano Rivers because the sediment discharge yields of these rivers are the highest in the study area (Table 1). The spatial distributions of Be, K₂O, Rb, Sn, light REEs, Th, and U are continuous between the watershed of the Ara River and the coast because granitic rocks and accretionary complexes underlie the watershed area. However, these elements are less abundant in the estuarine regions of the Shinano and Agano Rivers because volcanic rocks are the dominant lithology of these river systems. Characteristically, Li, MgO, P₂O₅, V, Cr, Ni, Ga, Nb, Mo, Cs, Pb and Bi are more abundant in clay samples from far offshore and notably less abundant in silt from near the shore. These distribution patterns can be simply explained by the grain size effect. Several samples from the estuarine region of the Agano River are highly enriched in Cu, Zn, As, Cd, and Hg. This enrichments may be influenced by metalliferous deposits distributed in the watershed of the Agano River. As in the examples noted above, it must be considered that the spatial distributions of elemental concentrations are not always continuous between land and sea. Nevertheless, the influence of material input from land to sea is evident.

6. 4. 2 Relict sediments on the continental shelf
   Coarse and fine sands are distributed on the continental

shelf off of Mogami and Joetsu and on the edge of the continental shelf off of Niigata. These sandy sediments are poor in many elements, with the exceptions of Fe₂O₃ and As. Ikehara *et al.* (1994a, b) and Katayama *et al.* (1994) reported that sand particles in these regions contain quartz coated in Fe hydroxides, which are interpreted as relict sediments because fresh modern sand is not coated. The Fe hydroxide-coated quartz grains absorb As efficiently over long periods (e.g., Sullivan and Aller, 1996). Enrichment of As in sandy sediments collected from the southern part of Sendai Bay is also explained by this mechanism, because Nishimura and Saito (2016) found quartz coated with Fe hydroxides (stained quartz) in the sandy sediments of this region. Arsenic is supplied to coastal seas mainly in the dissolved phase through rivers and is precipitated in coastal sediments (Ohta *et al.*, 2015). There are more As-enriched sandy sediments in the Sea of Japan because many major rivers flow into this sea (Table 1).

6. 4. 3 Hemipelagic conditions in deep sea basins
   Half of sediments in the Sea of Japan consist of clay, which is mainly deposited in deep-sea basins such as the Yamato Basin and Toyama Trough. These clays are rich in elements such as MnO, Cr, Ni, Cu, As, Mo, Sb, and Pb. Terashima *et al.* (1995b) and Imai *et al.* (1997) have pointed out that enrichments of these elements are caused by early diagenetic processes. These elements were released into pore water at greater depths in sediments under reducing conditions, diffused upward, and finally precipitated with Mn oxide under oxic condition (e.g., Shaw *et al.*, 1990). These deep-sea basins would be oxidative enough to cause Mn oxide precipitation because MnO concentrations are very high in sediments, and an oxygen-rich water mass (the Japan Sea Proper Water) covers the deep parts of the Sea of Japan (Gamo *et al.*, 1986).

6. 4. 4 Influence of local marine geology on marine geochemical maps: particularly extreme enrichment of Ba caused by barite deposition

Figures 5 and 6 show that marine sediments in the Sea of Japan are rather enriched in Li, Be, K_2O, Rb, Nb, Cs, Ba, light REEs, Ta, Th, and U compared to those in the Pacific Ocean in this region and sediments of the adjacent terrestrial areas. These elemental concentrations are particularly high in sediments around the Sado Ridge, Awashima Island, the Torimi-Guri Bank, and the Shin-Guri Bank (Ba and La in Fig. 4). The characteristics of these sediments would be controlled by local marine geology because these places are distant from terrestrial areas and the sediments are of various grain sizes. To highlight the signatures of these sediments, in Fig. 9, we illustrate the distributions of outliers in Be, Ba and La associated with marine geological maps at 1:200,000 scale (Okamura *et al.*, 1994, 1995a, 1996a, b). The threshold value for each element was determined by employing the Smirnov–Grubbs test for the original data at the 95% confidence level to identify outliers (Grubbs, 1969). Most of these outliers plot near marine faults associated with basement rocks. The upper surfaces of submarine topographic highs consist mainly of Middle Miocene–Pliocene siltstone called the Hirase Group (Okamura *et al.*, 1995a, b). These strata have been uplifted from the seafloor by reverse faults that underwent inversion during the Late Pliocene to Quaternary (Okamura, 2010). Nakajima et al. (1995) suggest that sediments around these topographic highs formed through denudation of basement rocks. The Hirase Group corresponds to Miocene–Pliocene siltstone with dacitic tuff distributed in the adjacent terrestrial area. Therefore, these marine sediments would mainly reflect the geochemistry of the Hirase Group.

However, the spatial distribution of the outliers in Ba concentration do not correspond to those of Be and La concentrations. In particular, extremely high Ba concentrations of 2,000–15,000 mg/kg cannot be explained by regional geology. Barite nodules are known from the submarine topographic highs of the Sado Ridge and the Shin-Guri, Torimi-Guri, and Oki-Kami Guri Banks (Sakai, 1971; Astakhova and Mel'nichenko, 2002); these locations correspond precisely to the locations where samples with high Ba concentrations were collected. Sakai (1971) proposed that barite nodules were formed by hydrothermal activity during the Quaternary glaciation based on oxygen and sulfur isotopic data, although the barite nodules are found in Miocene–Pliocene siltstone (Hirase Group). Astakhova and Mel'nichenko (2002) proposed that barite precipitated during the interactions of Ba-bearing solutions with sulfates of mud water. These workers pointed out that barite nodule occurrences are spatially inhomogeneous within the Hirase Group. Therefore, the distribution of Ba concentration outliers differs from those of Be and La concentration.

7. Summary

We elucidated the controls of marine sedimentary environments on the spatial distribution of elements using comprehensive geochemical maps of both the land and sea of the Tohoku region, Japan and its surroundings. Particle transportation through large rivers was identified as the dominant factor affecting the distribution of silt and clay on the continental shelf off of Niigata and around Sendai Bay. These areas are particularly abundant in Li, Cu, Zn, As, Mo, Cd, Sn, Sb, Hg, Pb, and Bi. These geochemical features are simply controlled by the grain size effect and do not reflect the geochemistry of the adjacent terrestrial area.

Coarse sands on the continental shelf are relict sediments. These sands contain large amounts of quartz coated with Fe hydroxides, which absorb As dissolved in water effectively. Distributions of Li, Be, P_2O_5, K_2O, Cr, Ni, Rb, Y, Nb, Sb, Cs, Ba, REEs, Ta, Tl, Th, and U are continuous between the Kitakami Mountains and nearshore regions such as offshore from Kamaishi. These relict sediments are inferred to have originated from coastal erosion and/or denudation of basement rocks during past regression and transgression because they are deposited at water depths of 50–150 m where they are unaffected by water action. The sandy sediments that occur widely on the shelf and slope of the Pacific Ocean in this region are homogenous across water depths, which suggests that these sandy sediments on the shelf have been transported by gravity-driven processes to the deep sea and have been influenced little by the denudation of basement rocks.

High concentrations of MgO, Al_2O_3, CaO, Sc, TiO_2, V, MnO, Fe_2O_3, Co, Ga, and Sr in sandy sediments on the continental shelf off of Hachinohe are explained as the result of denudation of Miocene volcanic materials. Sediments enriched in Li, Be, K_2O, Rb, Nb, Cs, Ba, REEs, Ta, Th, and U in submarine topographic highs in the Sea of Japan are attributed to the denudation of Miocene sedimentary rocks associated with acidic tuff and barite nodules.

The marine environment of the Sea of Japan is dominantly hemipelagic and pelagic. Early diagenetic processes enhance the concentrations of MgO, P_2O_5, TiO_2, Cr, MnO, Co, Ni, Cu, As, Mo, Cd, Sn, Sb, Hg, Pb, and Bi in clays deposited in the deep-sea basins under oxic condition associated with the Japan Sea Proper Water. The deep continental slope on the Pacific Ocean side also exists under hemipelagic sedimentary conditions with sediments enriched in Li, Cr, Ni, Cu, Zn, Mo, Cd, Sb, Cs, Hg, Bi, and U.

Therefore, the spatial distribution patterns of elements in these marine sediments are strongly controlled by their depositional environments. However, except for grain size effect and input of local geological materials, the elemental abundance patterns of these marine sediments are comparable between the Pacific Ocean and the Sea of Japan.
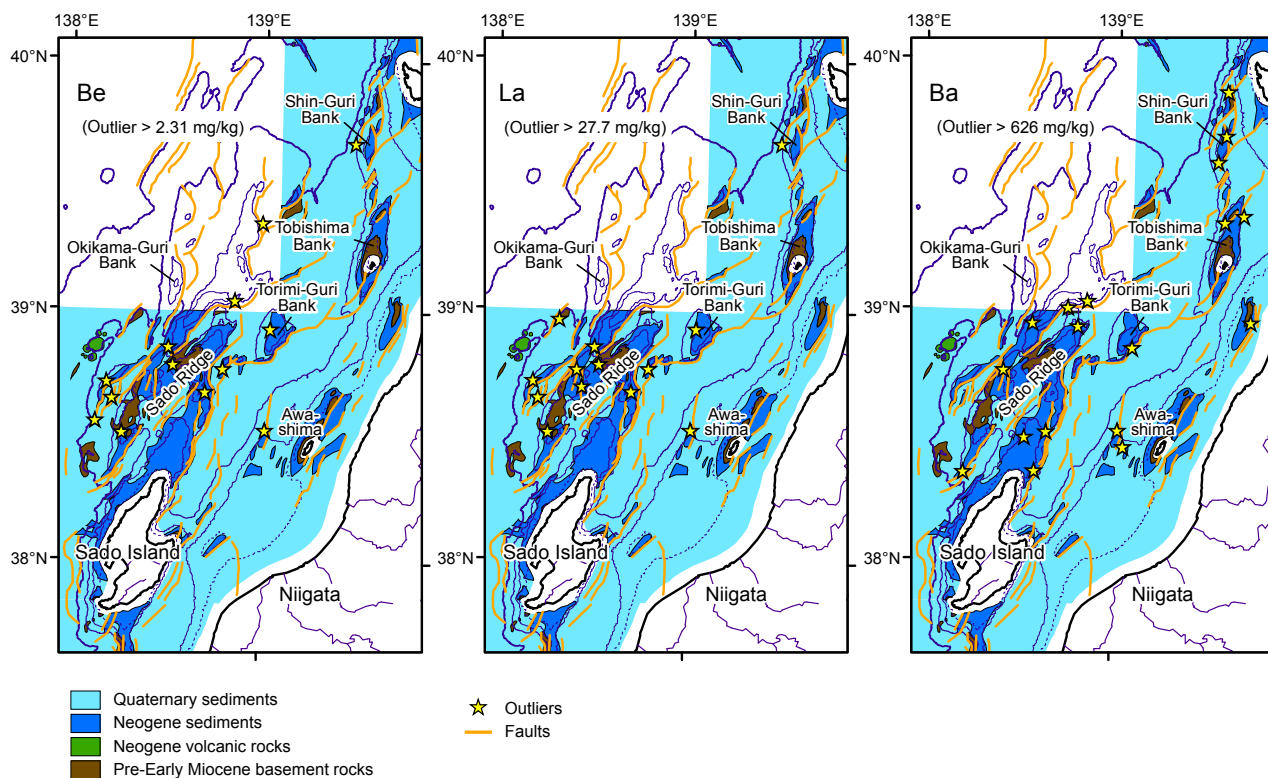
Fig. 9   Distributions of outliers in Be, La and Ba concentrations in marine sediments and marine geological maps at a scale of 1:200,000 (Okamura *et al.*, 1994, 1995a, 1996a, b).

References

Akimoto, T., Kawagoe, S. and Kazama, S. (2009) Estimation of sediment yield in Japan by using climate projection model. *Proceedings of Hydraulic Engineering*, **53**, 655–660 (in Japanese, with English abstract).

Arita, M. and Kinoshita, Y. (1978) *Sedimentological Map of Offing of Hachinohe*. 1:200,000 Marine Geology Map Series 9, Geological Survey of Japan.

Arita, M. and Kinoshita, Y. (1984) *Sedimentological Map of off Kamaishi*. 1:200,000 Marine Geology Map Series 25, Geological Survey of Japan (in Japanese, with English abstract).

Astakhova, N. and Mel'nichenko, Y. I. (2002) Barite nodules in the Japan Sea. *Lithology and Mineral Resources*, **37**, 39–46.

Fritz, C. O., Morris, P. E. and Richler, J. J. (2012) Effect size estimates: current use, calculations, and interpretation. *J. Exp. Psychol. Gen.*, **141**, 2–18.

Gamo, T., Nozaki, Y., Sakai, H., Nakai, T. and Tsubota, H. (1986) Spatial and temporal variations of water characteristics in the Japan Sea bottom layer. *J. Mar. Res.*, **44**, 781–793.

Geological Survey of Japan, AIST (ed.). (1992) *Geological Map of Japan, 1:1,000,000 (3rd, ed.)*. Geological Survey of Japan.

Goldich, S. S. (1938) A study in rock-weathering. *J. Geol.*, **46**, 17–58.

Grubbs, F. E. (1969) Procedures for Detecting Outlying Observations in Samples. *Technometrics*, **11**, 1–21.

Honza, E., Tamaki, E. and Murakami, F. (1978) Geological Map of the Japan and Kuril Trenches and the adjacent areas. *1:1,000,000 Marine Geology Map Series 11*.

Howarth, R. J. and Thornton, I. (1983) Regional Geochemical Mapping and its Application to Environmental Studies. *In* Thornton, I., ed., *Applied Environmental Geochemistry*, Academic Press, London, 41–73.

Iijima, A. and Kagami, H. (1961) Cainozoic tectonic developement of the continental slope, northeast of Japan. *J. Geol. Soc. Japan*, **67**, 561–577 (in Japanese, with English abstract).

Ikehara, K., Katayama, H. and Nakajima, T. (1994a) *Sedimentological Map of the Vicinity of Awashima*. 1:200,000 Marine Geology Map Series 42, Geological

Survey of Japan (in Japanese, with English abstract).

Ikehara, K., Nakajima, T. and Katayama, H. (1994b) *Sedimentological Map West of Akita*. 1:200,000 Marine Geology Map Series 41, Geological Survey of Japan (in Japanese, with English abstract).

Imai, N. (1987) Multielement analysis of stream sediment by ICP-AES. *Bunseki Kagaku*, **36**, T41–T45 (in Japanese, with English abstract).

Imai, N. (1990) Multielement analysis of rocks with the use of geological certified reference material by inductively coupled plasma mass spectrometry. *Anal. Sci.*, **6**, 389–395.

Imai, N., Terashima, S., Katayama, H., Nakajima, T., Ikehara, K. and Taniguchi, M. (1997) Geochemical behavior of heavy metals in coastal marine sediments from the eastern margin of the Japan Sea. *Bull. Geol. Surv. Japan*, **48**, 511–530 (in Japanese, with English abstract).

Imai, N., Terashima, S., Ohta, A., Mikoshiba, M., Okai, T., Tachibana, Y., Togashi, S., Matsuhisa, Y., Kanai, Y., Kamioka, H. and Taniguchi, M. (2004) *Geochemical map of Japan*. Geological Survey of Japan, AIST, 209p (in Japanese, with English abstract).

Imai, N., Terashima, S., Ohta, A., Mikoshiba, M., Okai, T., Tachibana, Y., Togashi, S., Matsuhisa, Y., Kanai, Y. and Kamioka, H. (2010) *Geochemical Map of Sea and Land of Japan*. Geological Survey of Japan, AIST, Tsukuba, 207p (in Japanese, with English abstract). Database available from https://gbank.gsj.jp/geochemmap/ (accessed 2016-07-12).

Katayama, H., Nakajima, T. and Ikehara, K. (1994) *Sedimentological Map South of Sado Island*. 1:200,000 Marine Geology Map Series 44, Geological Survey of Japan (in Japanese, with English abstract).

Nakajima, T. (1973) Submarine topography off the southern part of Sanriku district. *J. Geogr. (Chigaku Zasshi)*, **82**, 136–147 (in Japanese, with English abstract).

Nakajima, T., Katayama, H. and Ikehara, K. (1995) *Sedimentological Map North of Sado Island*. 1:200,000 Marine Geology Map Series 45, Geological Survey of Japan (in Japanese, with English abstract).

Nishimura, A. and Saito, Y. (2016) *Sedimentological Map off Kinkasan*. 1:200,000 Marine Geology Map Series, no. 87 (CD), Geological Survey of Japan, AIST (in Japanese, with English abstract).

Noda, A. and TuZino, T. (2007) Characteristics of sediments and their dispersal systems along the shelf and slope of an active forearc margin, eastern Hokkaido, northern Japan. *Sediment. Geol.*, **201**, 341–364.

Ohta, A. and Imai, N. (2011) Comprehensive Survey of Multi-Elements in Coastal Sea and Stream Sediments in the Island Arc Region of Japan: Mass Transfer from Terrestrial to Marine Environments. *In* El-Amin, M., ed., *Advanced Topics in Mass Transfer*, InTech, Croatia, 373–398.

Ohta, A., Imai, N., Terashima, S., Tachibana, Y., Ikehara, K., Okai, T., Ujiie-Mikoshiba, M. and Kubota, R. (2007) Elemental distribution of coastal sea and stream sediments in the island-arc region of Japan and mass transfer processes from terrestrial to marine environments. *Appl. Geochem.*, **22**, 2872–2891.

Ohta, A., Imai, N., Terashima, S., Tachibana, Y., Ikehara, K., Katayama, H. and Noda, A. (2010) Factors controlling regional spatial distribution of 53 elements in coastal sea sediments in northern Japan: Comparison of geochemical data derived from stream and marine sediments. *Appl. Geochem.*, **25**, 357–376.

Ohta, A., Imai, N., Terashima, S. and Tachibana, Y. (2011) Regional geochemical mapping in eastern Japan including the nation's capital, Tokyo. *Geochem.-Explor. Environ. Anal.*, **11**, 211–223.

Ohta, A., Imai, N., Terashima, S., Tachibana, Y. and Ikehara, K. (2013) Regional spatial distribution of multiple elements in the surface sediments of the eastern Tsushima Strait (southwestern Sea of Japan). *Appl. Geochem.*, **37**, 43–56.

Ohta, A., Imai, N., Terashima, S., Tachibana, Y., Ikehara, K. and Katayama, H. (2015) Elemental distribution of surface sediments around Oki Trough including adjacent terrestrial area: Strong impact of Japan Sea Proper Water on silty and clayey sediments. *Bull. Geol. Surv. Japan*, **66**, 81–101.

Okamura, Y. (2010) Relationships between geological structure and earthquake source faults along the eastern margin of the Japan Sea. *J. Geol. Soc. Japan*, **116**, 582–591 (in Japanese, with English abstract).

Okamura, Y. (2013) Active Faults in Japan Sea revealed by topography and geology. *Reports of seismic crusutal and activities in Japan discussed in the 198th, 199th meetings are recorded.*, **90**, p. 530–536. The coordinating Commitee for Earthquake Prediction, Japan (in Japanese).

Okamura, Y. and Tanahashi, M. (1983) *Geological Map off Kamaishi*. 1:200,000 Marine Geology Map Series 22, Geological Survey of Japan (in Japanese, with English abstract).

Okamura, Y., Takeuchi, K., Joshima, M. and Satoh, M. (1994) *Geological Map South of Sado Island*. 1:200,000 Marine Geology Map Series 43, Geological Survey of Japan (in Japanese, with English abstract).

Okamura, Y., Takeuchi, K., Joshima, M. and Satoh, M. (1995a) *Geological Map North of Sado Island*. 1:200,000 Marine Geology Map Series 46, Geological Survey of Japan (in Japanese, with English abstract).

Okamura, Y., Watanabe, M., Morijiri, R. and Satoh, M. (1995b) Rifting and basin inversion in the eastern margin of the Japan Sea. *Isl. Arc.*, **4**, 166–181.

Okamura, Y., Morijiri, R. and Satoh, M. (1996a) *Geological Map West of Akita*. 1:200,000 Marine Geology Map Series 48, Geological Survey of Japan (in Japanese, with English abstract).

Okamura, Y., Morijiri, R., Tsuchiya, N. and Satoh, M.

(1996b) *Geological Map of the Vicinity of Awashima.* 1:200,000 Marine Geology Map Series 47, Geological Survey of Japan (in Japanese, with English abstract).

Reimann, C. (2005) Geochemical mapping: technique or art? *Geochem.: Explor. Environ. Anal.*, **5**, 359–370.

Reimann, C., Siewers, U., Tarvainen, T., Bityukova, L., Eriksson, J., Gilucis, A., Gregorauskiene, V., Lukashev, V., Matinian, N. and Pasieczna, A. (2003) *Agricultural Soils in Northern Europe: A Geochemical Atlas.* E. Schweizerbart'sche Verlagsbuchhandlung, Stuttgart, Germany, 279p.

Richardson, J. T. (2011) Eta squared and partial eta squared as measures of effect size in educational research. *Educational Research Review*, **6**, 135–147.

Saito, Y. (1989) Classification of shelf sediments and their sedimentary facies in the storm-dominated shelf: A review. *J. Geogr. (Chigaku Zasshi)*, **98**, 350–365.

Sakai, H. (1971) Sulfur and oxygen isotopic study of barite concretions from banks in the Japan Sea off the Northeast Honshu, Japan. *Geochem. J.*, **5**, 79–93.

Salminen, R., Batista, M. J., Bidovec, M., Demetriades, A., B., D. V., De Vos, W., Duris, M., Gilucis, A., Gregorauskiene, V., Halamic, J., Heitzmann, P., Lima, A., Jordan, G., Klaver, G., Klein, P., Lis, J., Locutura, J., Marsina, K., Mazreku, A., O'Connor, P. J., Olsson, S. Å., Ottesen, R.-T., Petersell, V., Plant, J. A., Reeder, S., Salpeteur, I., Sandström, H., Siewers, U., Steenfelt, A. and Tarvainen, T. (2005) *Geochemical atlas of Europe. Part 1 —Background Information, Methodology and Maps.* Geological Survey of Finland, Espoo, Finland, 526p.

Shaw, T. J., Gieskes, J. M. and Jahnke, R. A. (1990) Early diagenesis in differing depositional environments: The response of transition metals in pore water. *Geochim. Cosmochim. Acta*, **54**, 1233–1246.

Shimamura, K. (2008) Revised chart of the submarine canyon and valley systems around the Japanese Islands —on their topographic features and their unsettled questions. *J. Geol. Soc. Japan*, **114**, 560–576 (in Japanese, with English abstract).

Sullivan, K. A. and Aller, R. C. (1996) Diagenetic cycling of arsenic in Amazon shelf sediments. *Geochim. Cosmochim. Acta*, **60**, 1465–1477.

Tamaki, K. (1978) *Geological Map off Hachinohe.* 1:200,000 Marine Geology Map Series 10, Geological Survey of Japan.

Tamaki, K., Honza, E., Yuasa, M., Nishimura, K. and Murakami, F. (1981) Geological Map of the Central Japan Sea. *1:1,000,000 Marine Geology Map Series 15.*

Taylor, S. R. and McLennan, S. M. (1995) The geochemical evolution of the continental crust. *Rev. Geophys.*, **33**, 241–265.

Terashima, S. and Katayama, H. (1993) Geochemical behavior of twelve elements in marine sediments from of Niigata, Japan. *Bull. Geol. Surv. Japan*, **44**, 55–74 (in Japanese, with English abstract).

Terashima, S., Katayama, H., Nakajima, T. and Ikehara, K. (1995a) Geochemical behavior of mercury in coastal marine sediments off Niigata, southeastern margin of the Japan Sea. *Chikyukagaku (Geochemistry)*, **29**, 25–36 (in Japanese, with English abstract).

Terashima, S., Nakajima, T., Katayama, H., Ikehara, K., Imai, N. and Taniguchi, M. (1995b) Geochemical behavior of heavy metals in marine sediments from the off Akita-Yamagata, Japan Sea. *Bull. Geol. Surv. Japan*, **46**, 153–176 (in Japanese, with English abstract).

Ujiie-Mikoshiba, M., Imai, N., Terashima, S., Tachibana, Y. and Okai, T. (2006) Geochemical mapping in northern Honshu, Japan. *Appl. Geochem.*, **21**, 492–514.

Weaver, T. A., Broxton, D. E., Bolivar, S. L. and Freeman, S. H. (1983) *The Geochemical Atlas of Alaska: Compiled by the Geochemistry Group, Earth Sciences Division, Los Alamos National Laboratory.* GJBX-32(83), Los Alamos, 141p.

Webb, J. S., Thornton, I., Thompson, M., Howarth, R. J. and Lowenstein, P. L. (1978) *The Wolfson Geochemical Atlas of England and Wales.* Clarendon Press, Oxford, 69p.

Yashima, K., Imai, K. and Nishizawa, K. (1982) 1:1,000,000 Bathymetric Charts "Hokkaido", "North-east Nippon" and Submarine Topography. *Report of Hydrographic and Oceanographic Researches*, **17**, 93–162 (in Japanese, with English abstract).

東北地方の多元素海域地球化学図に対し太平洋側と日本海側で堆積環境の違いが与える影響

太田充恒・今井　登・立花好子・池原　研・片山　肇・中嶋　健

要　旨

　著者らは東北地方の陸海域包括地球化学図を作成し，海域の堆積環境が広域元素濃度分布にどのような影響を与えるかについて調べた．日本海の堆積物はカリウム，バリウム，希土類元素など珪長質火成岩に多く含まれる元素に富み，特に海底地形の高まりで採取された堆積物に著しく濃集する傾向が認められた．この堆積物は，デイサイト質火山灰やバライト団塊などを伴う新第三紀堆積岩の削剥生成物と考えられる．深海盆に分布するシルトや粘土は，マンガン，カドミウム，鉛などに富んでおり，初期続成作用がこれらの元素の濃集の原因と考えられる．大陸棚のシルト質堆積物は大規模河川から供給されたにもかかわらず，その化学組成は隣接する陸域物質の影響よりは，粒径効果の影響が強く現れていた．太平洋側に広く分布する砂質堆積物は主に，波浪限界深度よりも深い海域で採取された．これらの化学組成は均質であり，苦鉄質火山岩の影響を受けた河川堆積物の化学組成と類似していた．この結果から，これらの堆積物は第四紀の苦鉄質火山活動の影響下で形成された残存堆積物であり，陸棚から深海へ重力流によって移動していったと考えられる．陸域の土砂生産量の内，81%は日本海側へ供給されるが，必ずしも陸と海との間で元素濃度の空間分布に連続性が認められる訳ではない．同様の結果は太平洋側にも認められる．例外的に，釜石沖の粗粒砂は，隣接する陸域に露出する付加帯堆積岩や花崗岩に多く含まれる元素に富む特徴を示す．この地域の河川は皆小規模であることから土砂生産量は少ないことを考慮すると，これらの粗粒砂は海進・海退期に母岩の海岸浸食・削剥などによって形成されたと考えられる．

Article

Sulfur isotopic ratios and mode of occurrence of stibnite at the Hishikari epithermal Au-Ag deposit, Japan

Toru Shimizu[1,*]

Abstract: Mode of occurrence and sulfur isotopic ratios (δ^{34}S) of stibnite were investigated to understand the characteristics of stibnite mineralization, and the source of stibnite sulfur at the Hishikari epithermal Au-Ag deposit. Stibnite occurs as prismatic or acicular crystals forming radiating aggregates in quartz druses, indicating that stibnite precipitated during the last stage of sequential mineralization.

Stibnite samples were collected from several veins at 40 and 10 ML (mine meter level) within the bonanza (high-grade Au) zone, located between 150 and -50 ML. Sulfur isotopic values (δ^{34}S) of stibnite samples yielded a narrow range: -0.2 to +0.7‰ (n = 7), and are similar to previous δ^{34}S data from ginguro (an Au-Ag-rich black sulfide band) in earlier mineralization (+0.4 to +0.6‰), and to δ^{34}S data from pyrite in veins and hydrothermally-altered host rocks (Shimanto Supergroup sedimentary rocks)(-1.1 to +1.8‰).

The presence of stibnite within the bonanza zone indicates that stibnite mineralization overprinted Au-Ag mineralization at the same depth. Considering that stibnite commonly forms in the peripheral portions of the epithermal environment, e.g., stibnite deposition on the top of an Au-Ag orebody near the surface, the overprinting of stibnite mineralization on Au-Ag mineralization at depth in the Hishikari deposit may reflect mineralogically exceptional circumstances.

The narrow isotopic range of stibnite sulfur could be due to a spatially homogeneous source of stibnite sulfur. The isotopic similarity between stibnite and ginguro sulfur suggests that the source of sulfide sulfur may have been the same throughout both early and late vein formation. The similarity between sulfur isotopic values in stibnite and other sulfides (ginguro and pyrite) also suggests that the source of stibnite sulfur is likely to be dominantly magmatic, as with the source of other sulfide sulfur discussed in previous studies of this deposit.

Keywords: stibnite, sulfur isotopes, mode of occurrence, Hishikari deposit

1. Introduction

Stibnite (Sb_2S_3), a principal source of mined antimony (Sb), is a common vein mineral in hydrothermal systems (Schwarz-Schampera, 2014). Although stibnite is one of the common accessory minerals at the Hishikari epithermal Au-Ag deposit (Sekine *et al*., 2002), studies of its genetics are scarce.

Sulfur isotope data for stibnite are a powerful tool for understanding the genesis of stibnite mineralization, in conjunction with other geological, mineralogical, and geochemical data (e.g., Robinson and Farrand, 1982; Gokçe and Spiro, 1991; Ishihara *et al*., 2000; Imai *et al*., 2006). However, sulfur isotopic values for stibnite at the Hishikari deposit have not been previously documented, except for one value of -0.2‰ reported by Imai *et al*. (2006); this was not fully discussed in terms of the source

of stibnite sulfur.

This study presents the morphological modes of occurrence for stibnite crystals, and their sulfur isotopic values from several veins. It discusses the spatial characteristics of stibnite occurrence, and the potential source of stibnite sulfur in comparison to previous isotopic data from other sulfides at the Hishikari deposit.

2. Geologic background and mineralization

The Hishikari deposit is located in southern Kyushu, Japan (Fig. 1a). Other Au-Ag deposits near Hishikari include Okuchi, Yamagano, Kushikino, Akeshi and Kasuga. The Hishikari deposit formed in the Pleistocene (0.61–1.25 Ma) (Izawa *et al*., 1993; Sanematsu *et al*., 2005; Tohma *et al*., 2010), within basement sedimentary rocks of the Cretaceous Shimanto Supergroup and

[1] AIST, Geological Survey of Japan, Research Institute of Earthquake and Volcano Geology

* Corresponding author: T. Shimizu,Central 7,1-1-1 Higashi, Tsukuba, Ibaraki 305-8567, Japan. Email: t.shimizu@aist.go.jp
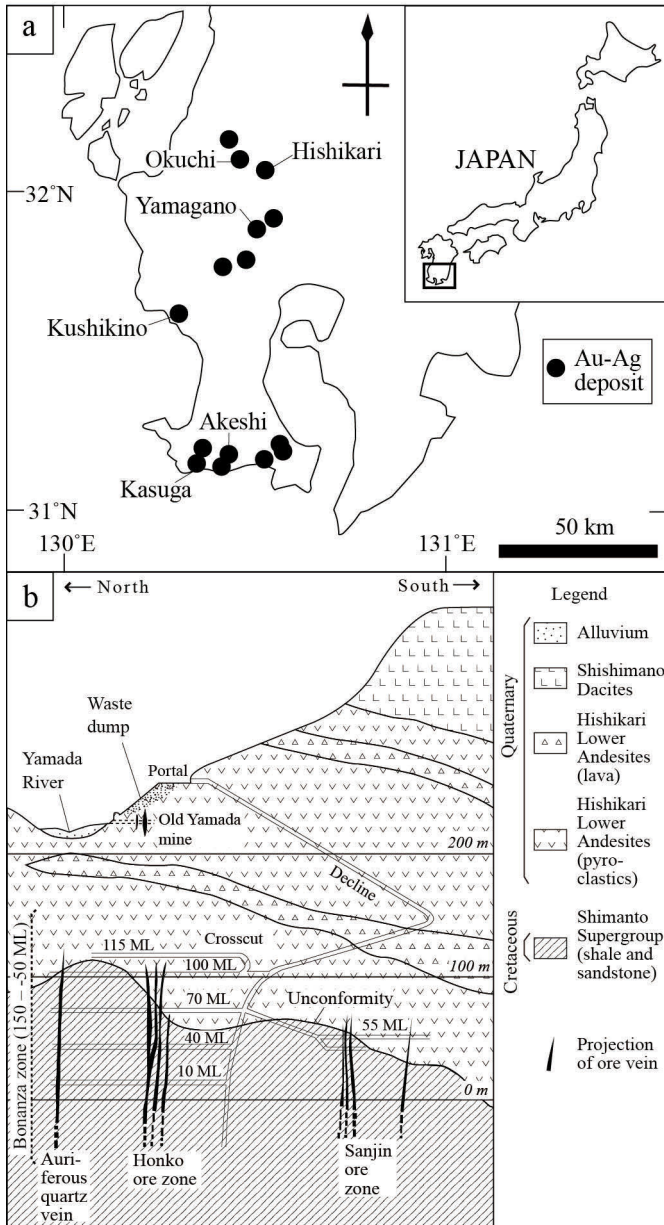
Fig. 1 Location (a) and schematic geological cross section around the Honko and Sanjin ore zones at the Hishikari deposit (b) (Partly modified after Sekine *et al*., 2002). 'ML' denotes the mine meter level. Meter (m) in italics indicates elevation above sea level. Some ore veins, not shown in the figure, continue up to 150 ML (Ibaraki and Suzuki, 1993).

Quaternary volcanic rocks in ascending order (Fig. 1b). The deposit consists of three ore zones: Honko (Main), Sanjin, and Yamada (Fig. 2); the Honko and Sanjin zones are relatively enriched in Au, especially in the upper half of the ore zones (Ibaraki, 1990; Ibaraki and Suzuki, 1993). In these ore zones, quartz veins generally strike N50°E and dip 70–90°NW (Izawa *et al*., 1990). Drill core surveys show that the high-grade Au "bonanza" zone is located between 150 and -50 ML (mine meter level, which is equal to above sea level, Fig. 1), although low-grade Au veins continue at depth (Ibaraki and Suzuki, 1993). Ore veins are classified as early and late veins based on observed vein crosscutting relationships (Sekine *et al*., 2002).

The assemblages of ore and gangue minerals are the same for early and late veins (Sekine *et al*., 2002). Ore minerals mainly consist of electrum, chalcopyrite, pyrite,

and marcasite, with minor constituents of naumannite, sphalerite, galena and stibnite. The gangue minerals are mainly quartz, adularia, smectite with small amounts of sericite, chlorite, and kaolinite. Ginguro (an Au-Ag-rich black sulfide band, "silver black") tends to be present along the outer side of early veins in higher levels of the deposits (Izawa *et al*., 1990; Sekine *et al*., 2002). Izawa *et al*. (1990) reported that antimony was first deposited as pyrargyrite (Ag_3SbS_3) and miagyrite ($Ag_2Sb_2S_4$) in the ginguro, then as stibnite and pyrargyrite with fine-grained pyrite in cracks, druses and fractures in the veins. Fine-grained anhedral quartz is commonly associated with adularia, forming porcellanous white bands, as shown in the Ryosen vein swarm in the Honko zone; these were subsequently overprinted by euhedral quartz, forming druses (Matsuhisa and Aoki, 1994; Shimizu, 2015).
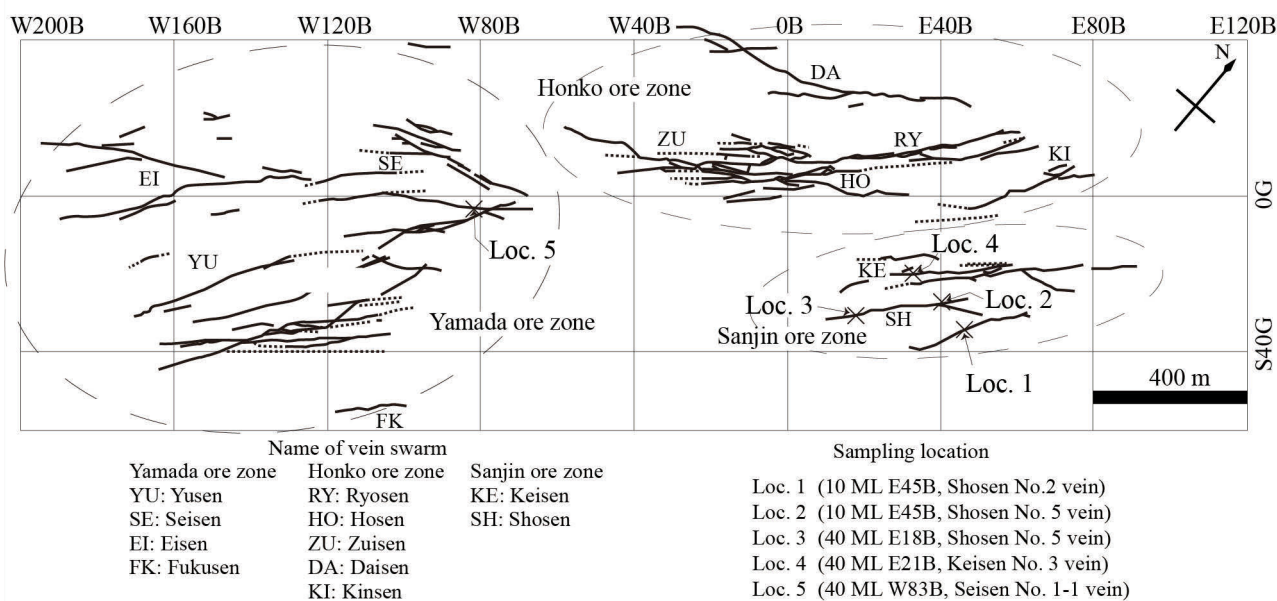
Fig. 2 Sampling location plotted on the vein map of the Hishikari deposit (Sumitomo metal Mining Co., Ltd., 2012). The vein distribution is projected to 40 ML (40 m mine level = 40 m above sea level).

3. Methods

Sample collection and observation

Samples were collected from five locations among different veins, at different mine levels: Loc. 1 (10 ML, Shosen No. 2 vein), Loc. 2 (10 ML, Shosen No. 5 vein), Loc. 3 (40 ML, Shosen No. 5 vein), and Loc. 4 (40 ML, Keisen No. 3 vein) in the Sanjin ore zone, and Loc. 5 (40 ML, Seisen No. 1-1 vein) in the Yamada ore zone (Fig. 2). The samples at Loc. 1 were collected from three different quartz druses filled with stibnite crystals in a crustiform-banded vein (Fig. 3). The morphological characteristics of the samples were examined both in hand specimen and in binocular microscope.

Sulfur isotope analysis

Analyzed stibnite crystals were separated by handpicking from seven samples, which are listed in Table 1, and were carefully checked for contamination via binocular microscope examination. A single or a few crystals were crushed and ground to powder for each analytical run.

All stibnite sulfur isotope measurements were conducted at the Geological Survey of Japan, using a conventional method: the stibnite was evolved to H_2S using tin (II)-strong phosphoric acid (Kiba reagent) at 280°C (Sasaki *et al.*, 1979), and precipitated as Ag_2S that was combusted to SO_2 gas using Cu_2O in a vacuum at 900°C (Robinson and Kusakabe, 1975). The gas was purified with a closed n-pentane trap (Kusakabe, 2005) to separate SO_2 from CO_2 due to contamination during sample preparation. The purified gas was analyzed on a Finnigan MAT 252 mass spectrometer, and the data are presented as $\delta^{34}S$

Fig. 3 A working face of the Shosen No. 2 vein at 10 ML, E45B looking towards the northeast (Loc. 1 in Fig. 2). Dotted circles on the vein indicate the area of druses where stibnite samples for sulfur isotopic measurements were collected. Loc. 1-1, Loc. 1-2 and Loc. 1-5 indicate the sample names that correspond to those in Table 1.

(‰) relative to the Canyon Diablo Troilite (CDT). The overall experimental reproducibility in this study was ±0.2‰ (1σ).

4. Results

Mode of occurrence of stibnite

Morphological characteristics of stibnite at hand

Table 1   Mode of occurrence and sulfur isotopic values for stibnite at the Hishikari deposit

Sampling locations	Mode of occurrence of stibnite	Host rock	δ^{34}S (‰)	Remarks
Loc. 1 (10 ML E45B, Shosen No. 2 vein)	Random growths of prismatic or acicular stibnite on euhedral quartz crystals forming a druse at Loc. 1-1 in Fig. 3. Some stibnite crystals are bent. Stibnite crystals are 10 to 23 mm in size.	Sedimentary rocks (Shimanto Supergroup)	+0.6	Sample name: 20120919 Loc.1-1
Loc. 1 (10 ML E45B, Shosen No. 2 vein)	Prismatic stibnite randomly growing inwards from euhedral quartz cavity walls at Loc.1-2 in Fig. 3 (Fig. 4a). Stibnite crystals are 1 to 15 mm in size.	Sedimentary rocks (Shimanto Supergroup)	+0.7	Sample name: 20120919 Loc.1-2
Loc. 1 (10 ML E45B, Shosen No. 2 vein)	Aggregates of prismatic stibnite crystals, randomly or radially growing on euhedral quartz crystals, forming a druse at Loc. 1-5 in Fig. 3. Stibnite crystals are 1 to 12 mm in size.	Sedimentary rocks (Shimanto Supergroup)	+0.1	Sample name: 20120919 Loc.1-5
Loc. 2 (10 ML E45B, Shosen No. 5 vein)	Aggregates of radial prismatic stibnite crystals at Loc. 2 in Fig. 2 (Fig. 4b). Stibnite crystals are 4 to 30 mm in size.	Sedimentary rocks (Shimanto Supergroup)	+0.4	A sample provided by Hishikari mine
Loc. 3 (40 ML E18B, Shosen No. 5 vein)	Bundles of subparallel-orientation prismatic stibnite crystals overgrown on euhedral quartz crystals. Stibnite crystals are 1 to 6 mm in size.	Hishikari Lower Andesites	-0.2	Sample name: 199407 3-3
Loc. 4 (40 ML E21W, Keisen No.3 vein)	Aggregates of radial prismatic or acicular stibnite crystals. Stibnite crystals are 1 to 10 mm in size.	Hishikari Lower Andesites	-0.1	A sample provided by Hishikari mine
Loc. 5 (40 ML W83B, Seisen No.1-1)	Acicular or prismatic stibnite crystals. The crystals are 3 to 11 mm in size.	Hishikari Lower Andesites	+0.3	A sample provided by Hishikari mine

Note: Sampling locations correspond to those in Fig. 2.

specimen scale are summarized in Table 1. Stibnite commonly occurs as lead-gray prismatic or acicular crystals protruding randomly into a druse of quartz (Fig. 4a), and/or as radiating aggregates (Fig. 4b). The crystals are elongated, up to 30 mm maximum (Table 1). There are no other ore minerals associated with stibnite at Loc. 1-1, 1-2 and 1-5, and Loc. 3 (Figs. 2 and 3). Whether other ore minerals coexist with stibnite is unknown for the samples from Locs. 2, 4 and 5 (Fig. 2).

Sulfur isotopic data
  Seven δ^{34}S values for stibnite samples from Loc. 1 to 5 are listed in Table 1. The values range between -0.2 and +0.7‰ and are plotted in Fig. 5, together with other sulfide data from previous studies. The δ^{34}S values of stibnite are consistent with one value of stibnite, -0.2‰ reported by Imai *et al.* (2006).

5. Discussion

  Formation of prismatic, acicular or radial stibnite crystals in quartz druses and fractures is a common mineralogical feature in many antimony-bearing hydrothermal deposits, indicating that stibnite precipitated during the last stage of sequential mineralization (e.g., Ikeda, 1969; Izawa *et al.*, 1990; Bailly *et al.*, 2000; Wagner and Cook, 2000; Wang *et al.*, 2012). Although Izawa (1990) described stibnite as tending to form at higher elevations at the Hishikari deposit, the present study documents stibnite at 40 and 10 ML at the Sanjin and Yamada ore zones, and indicates that stibnite mineralization overprinted the preceding Au-Ag mineralization responsible for forming the bonanza zone (150 to -50 ML, Fig. 1) (Ibaraki and Suzuki, 1993). The overprinting of stibnite mineralization on Au-Ag mineralization has also been seen irrespective of depth at the Okuchi epithermal Au-Ag deposit near the Hishikari deposit (Fig. 1a; Ikeda, 1969). Stibnite, however, typically
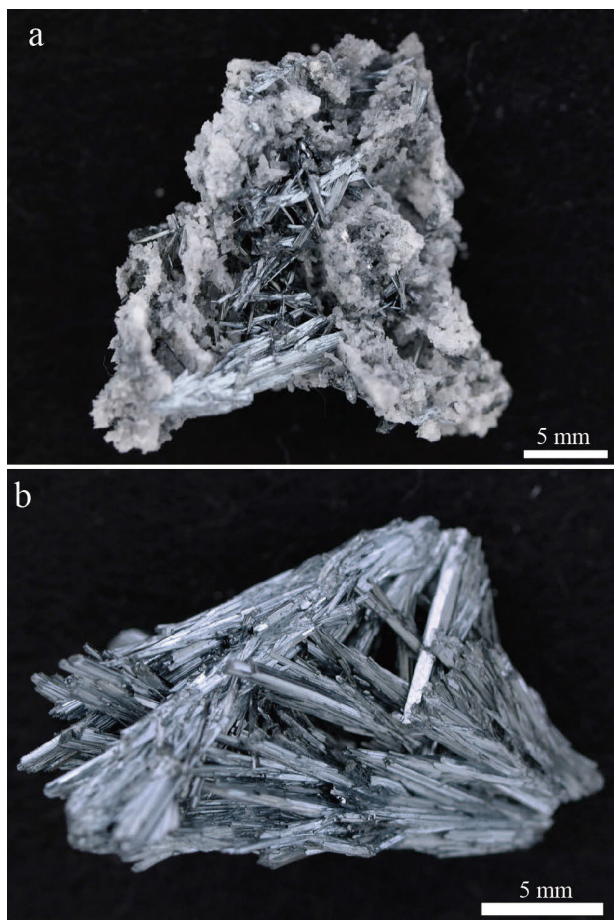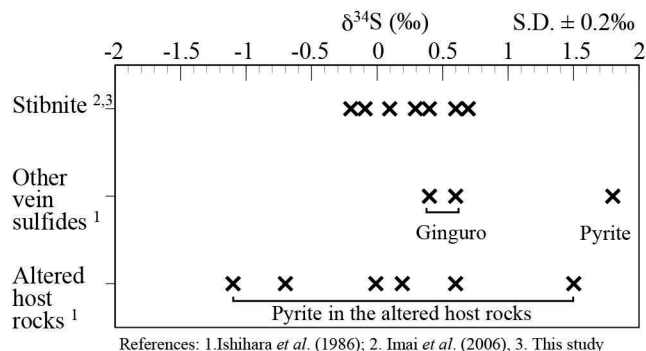
Fig. 4 Modes of occurrence of stibnite from the Shosen 5 vein, Sanjin ore zone. (a) Stibnite protruding into a druse of euhedral quartz (Loc. 1 in Fig. 2). (b) Aggregates of radially-distributed stibnite (Loc. 2 in Fig. 2).

Fig. 5 Plot of sulfur isotopic values ($\delta^{34}S$) for stibnite, other vein sulfides, and altered host rocks (Shimanto Supergroup sedimentary rocks) at the Hishikari deposit.

preferentially precipitates in the peripheral portions of epithermal systems (Morteani *et al.*, 2011; Schwarz-Schampera, 2014), e.g., stibnite deposition on the top of an Au-Ag orebody near the surface (Kinoshita, 1973). This suggests that the overprinting of stibnite mineralization on Au-Ag mineralization at depth at the Hishikari and the Okuchi deposits may have required mineralogically unusual circumstances.

As shown in Fig. 5, the $\delta^{34}S$ values of stibnite form a narrow-range, -0.2 to +0.7‰, representing different veins between 40 and 10 ML (Shosen No. 2 and No. 5 veins, and Keisen No. 3 vein in the Sanjin ore zone; and Seisen vein No. 1-1 vein in the Yamada ore zone) (Fig. 2). This suggests that the source of stibnite sulfur could be spatially homogeneous for these mine levels.

The $\delta^{34}S$ values of stibnite are also similar to previous study values for ginguro (+0.4 and +0.6‰ in Fig. 5) and pyrite in veins and altered host rocks (-1.1 to +1.8‰ in Fig. 5), although all $\delta^{34}S$ values from vein sulfides and altered rocks (Fig. 5) are higher than those of unaltered host rocks

(Shimanto Supergroup sedimentary rocks), which range between -1.4 and -21.5‰ and average -12.0‰ (Ishihara *et al.*, 1986). The similarity of $\delta^{34}S$ values between later stibnite mineralization and earlier ginguro mineralization suggests that the source of sulfide sulfur may have been the same throughout ore mineralization. The similarity of $\delta^{34}S$ values between stibnite and all other sulfides (ginguro and pyrite) indicates that the source of stibnite sulfur is the same as for the other sulfides; this sulfur source has been discussed in previous geological and isotopic studies, detailed as follows.

Ishihara *et al.* (1986) first proposed that sulfide sulfur at the Hishikari deposit was derived from magmatic fluid generated from a felsic subvolcanic intrusive body, ruling out the possibilities of other sources of sulfur based on interpretation of $\delta^{34}S$ data for sulfide sulfur in veins, altered host rocks, and unaltered host rocks (Shimanto Supergroup sedimentary rocks, Fig. 1). This study was followed by two more isotopic studies: Morishita (1993) discussed the low $\delta^{13}C$ values ($\approx$ -11‰) of epithermal ore fluids in southern Kyushu, positing they may have been a result of contribution of organic carbon from the Shimanto Supergroup sedimentary rocks. Imai *et al.* (1998) proposed that the low δD values of ore fluids (-60‰ to <-100‰) were a result of leaching of hydrogen from the Shimanto Supergroup sedimentary rocks. These two studies suggest that the Shimanto Supergroup sedimentary rocks are genetically related to ore fluids. With the interpretation of the $\delta^{13}C$ and δD values referenced above, Shikazono (1999) reinterpreted the earlier $\delta^{34}S$ values of sulfides (Ishihara *et al.*, 1986). Considering the Hishikari deposit was situated in the non-green tuff region where the Shimanto Supergroup sedimentary rocks underlay subaerial volcanic rocks (Fig. 1), Shikazono (1999) determined that the $\delta^{34}S$ values of sulfides at the Hishikari deposit (-1.1 to +1.8‰ in Fig. 5) were likely a result of a dominant contribution of magmatic sulfur, with a minor contribution of sedimentary sulfur from the Shimanto Supergroup sedimentary rocks.

6. Conclusions

1. The overprinting of stibnite mineralization on Au-Ag mineralization at the Hishikari deposit at depth may have been due to mineralogically unusual conditions.

2. The $\delta^{34}S$ values of stibnite, morphologically determined to be from the latest stage of sequential mineralization, are narrow-ranged (-0.2 to +0.7‰) among different veins, suggesting that the source of stibnite sulfur could be spatially homogeneous at the Hishikari deposit.

3. The similarity of $\delta^{34}S$ values between stibnite, and ginguro from earlier mineralization suggests that the source of sulfide sulfur may have been the same throughout ore mineralization.

4. The similarity of $\delta^{34}S$ values among the stibnite, ginguro, and pyrite in veins and altered host rocks suggests a likely dominantly magmatic origin of stibnite sulfur, the same as for the other sulfides.

References

Bailly, L., Bouchot, V., Beny, C. and Milesi, J. (2000) Fluid inclusion study of stibnite using infrared microscopy: An example from the Brouzils antimony deposit (Vendee, Armoriscan Massif, France). *Economic Geology*, **95**, 221–226.

Gokçe A. and Spiro, B. (1991) Sulfur isotope study of source and deposits of stibnite in the Turhal Area, Turkey. *Mineralium Deposita*, **26**, 30–33.

Ibaraki, K. (1990) General description of Yamada deposit, Hishikari mine. *In Prof. Y. Urashima commemoration volume on the occasion of his retirement*, 197–200.

Ibaraki, K. and Suzuki, R. (1993) Gold-silver quartz-adularia veins of the Main, Yamada and Sanjin deposits, Hishikari gold mine; a comparative study of their geology and ore deposits. *Resource Geology Special Issue*, **14**, 1–11.

Ikeda, T. (1969) On the ore deposits and prospecting at the Okuchi mine, Kagoshima prefecture. *Mining Geology*, **19**, 132–146 (in Japanese with English abstract).

Imai, A., Shimazaki, H. and Nishizawa, T. (1998) Hydrogen isotope study of fluid inclusions in vein quartz, Hishikari gold deposits, Japan. *Resource Geology*, **48**, 159–170.

Imai, A., Shikazono, N., Shimizu, M. and Shimazaki, H. (2006) Sulfur isotopic study on Hg and Sb deposits in Japan. *Resource Geology*, **56**, 37–48.

Ishihara, S., Sakamaki, Y., Sasaki, A., Teraoka, Y. and Terashima, S. (1986) Role of the basement in the genesis of the Hishikari gold-quartz vein deposit, southern Kyushu, Japan. *Mining Geology*, **36**, 495–509.

Ishihara, S., Sasaki, A., Minagawa, T., Bunno, M., Shishido, A. and Tanaka, R. (2000) Paired sulfur isotopic belts: Late Cenozoic ore deposits of Southwest Japan. *Bulletin of Geological Survey of Japan*, **51**, 283–297.

Izawa, E., Kurihara, M. and Itaya, T. (1993) K-Ar ages and initial Ar isotopic ratio of adularia-quartz veins from the Hishikari gold deposit, Japan. *Resource Geology Special Issue*, **14**, 63–69.

Izawa, E., Urashima, Y., Ibaraki, K., Suzuki, R., Yokoyama, T., Kawasaki, K., Koga, A. and Taguchi, S. (1990) The Hishikari gold deposit: High grade epithermal veins in Quaternary volcanics of southern Kyushu, Japan. *Journal of Geochemical exploration*, **36**, 1–56.

Kinoshita, K. (1973) Antimony ore, in Kinoshita, K., ed., *Japanese Regional Ore Deposits Record*: Japan, Asakura Publishing Co., Ltd., 210–220 (in Japanese).

Kusakabe, M. (2005) A closed pentane trap for separation of SO_2 from CO_2 for precise $\delta^{18}O$ and $\delta^{34}S$ measurements. *Geochemical Journal*, **39**, 285–287.

Matsuhisa, Y. and Aoki, M. (1994) Temperature and oxygen isotope variations during formation of the Hishikari epithermal gold-silver veins, southern Kyushu, Japan. *Economic Geology*, **89**, 1608–1613.

Morishita, Y. (1993) Carbon and oxygen isotopic characteristics of epithermal veins in the Hokusatsu gold district, southern Kyushu, Japan. *Resource Geology Special Issue*, **14**, 103–114.

Morteani, G., Ruggieri, G., Möller, P. and Preinfalk, C. (2011) Geothermal mineralized scale in the pipe system of the geothermal Piancastagnaio power plant (Mt. Amiata geothermal area): a key to understand the stibnite, cinnabarite and gold mineralization of Tuscany (central Italy). *Mineralium Deposita*, **46**, 197–210.

Robinson, W. B. and Kusakabe, M. (1975) Quantitative preparation of sulfur dioxide $^{34}S/^{32}S$ analyses from sulfides by combustion with cuprous oxide. *Analytical Chemistry*, **47**, 1179–1181.

Robinson, W. B. and Farrand, M. G. (1982) Sulfur isotopes and the origin of stibnite mineralization in New England, Australia. *Mineralium Deposita*, **17**, 161–174.

Sanematsu, K., Duncan, R., Imai, A. and Watanabe, K. (2005) Geochronological constraints using $^{40}Ar/^{39}Ar$ dating on the mineralization of the Hishikari epithermal gold deposit, Japan. *Resource Geology*, **55**, 249–266.

Sasaki, A., Arikawa, Y. and Folinsbee, E. R. (1979) Kiba reagent method of sulfur extraction applied to isotopic work. *Bulletin of Geological Survey of Japan*, **30**, 241–245.

Schwarz-Schampera, U. (2014) Antimony. In Gunn, G., ed., *Critical Metals Handbook*, UK, John Wiley & Sons, Ltd., 70–98.

Sekine, R., Izawa, E. and Watanabe, K. (2002) Timing of fracture formation and duration of mineralization at the Hishikari deposit, southern Kyushu, Japan. *Resource Geology*, **52**, 395–404.

Shikazono, N. (1999) Sulfur isotopic composition and origin of sulfide sulfur in epithermal Au-Ag vein-type deposits in Japan. *Resource Geology Special Issue*, **20**, 39–45.

Shimizu, T. (2015) Elemental analysis of bonanza ores of the Ryosen veins, Hishikari epithermal Au-Ag deposit, Japan, using micro X-ray fluorescence (µ-XRF). *Bulletin of the Geological Survey of Japan*, **66**, 1–14.

Sumitomo Metal Mining Co., Ltd. (2012) Hishikari mine. 10p. (in Japanese).

Tohma, Y., Imai, A., Sanematsu, K., Yonezu, K., Takahashi, R., Koyama, M., Sekine, R., Duncan, R. and Watanabe, K. (2010) Characteristics and mineralization age of the Fukusen No. 1 vein, Hishikari epithermal gold deposits, southern Kyushu, Japan. *Resource Geology*, **60**, 348–358.

Wagner, T. and Cook, N. J. (2000) Late-Variscan antimony mineralization in the Rheinisches Schiefergebirge, NW Germany: evidence for stibnite precipitation by drastic cooling of high-temperature fluid systems. *Mineralium Deposita*, **35**, 206–222.

Wang, J., Wen, H., Fan, H. and Zhu, J. (2012) Sm-Nd geochronology, REE geochemistry and C and O isotope characteristics of calcites and stibnites from the Banian antimony deposit, Guishou Province, China. *Geochemical Journal*, **46**, 393–407.

菱刈浅熱水性金銀鉱床産輝安鉱の硫黄同位体比と産状

清水　徹

要　旨

　菱刈浅熱水性金銀鉱床の輝安鉱産状の特徴と硫黄の起源を理解するため, 輝安鉱の産状と硫黄同位体比 (δ34S) を精査した. 輝安鉱は角柱状または針状結晶を示して石英晶洞中に放射状の塊をなしており, 輝安鉱が一連の鉱化作用最末期に形成したことを意味する.

　輝安鉱試料は, ボナンザ (金に富む) ゾーン内の複数鉱脈の40若しくは10 ML (坑内深度レベル) にて採取した. 輝安鉱の硫黄同位体比は, 狭い範囲：-0.2から +0.7‰ (測定数： 7) を示し, 輝安鉱の硫黄同位体比は過去のδ34S値：+0.4 から +0.6‰ (銀黒), 及び-1.1 から +1.8‰ (脈内の黄鉄鉱, 及び四万十層群からなる熱水変質母岩) に類似している.

　輝安鉱の鉱化作用がボナンザゾーン内に見られることは, 同一深度で輝安鉱の鉱化作用が金銀鉱化作用に重複していたことを意味する. 輝安鉱が一般的に浅熱水環境の縁辺部, 例えば金銀鉱脈鉱床の地表に近い上部に形成することを考慮すると, 菱刈鉱床では深部 (40及び10 ML) で輝安鉱と金銀鉱物が重複形成したことは, 鉱化作用としては特異な環境であったかもしれない.

　狭い範囲を示す輝安鉱のδ34S値から, 輝安鉱硫黄の起源は空間的に均質であったと考えられる. 輝安鉱と銀黒の間のδ34S値の類似性は, 鉱脈形成時, 硫化物硫黄の起源は時間的にも均質であったことを意味するかもしれない. また, 輝安鉱と他の全ての硫化鉱物のδ34S値の類似性から, 輝安鉱硫黄の起源は, 従来研究における他の硫化鉱物の起源に関する考察と同様に, マグマが主体であったと思われる.

Report

LA-ICP-MS U–Pb and fission-track ages of felsic tuff beds of the Takikubo Formation, Izumi Group in the Kan-onji district, eastern Shikoku, southwestern Japan

Atsushi Noda[1,*], Tohru Danhara[2], Hideki Iwano[2], and Takafumi Hirata[3]

Abstract: LA-ICP-MS U–Pb and fission-track (FT) dating were performed for detrital zircons in two felsic tuff samples (KT01 and KT02) in order to estimate the depositional age of the Takikubo Formation (Izumi Group) in the Kan-onji district, eastern Shikoku, southwestern Japan. Total 30 grains analyzed for each sample indicated that the U–Pb ages composed of multiple populations chiefly of younger (75–85 Ma) and older (85–95 Ma) clusters. The concordia ages calculated by grains in the younger clusters were 78.3±0.5 Ma (2σ) for KT01 (number of accepted grains $n = 23$) and 80.8±0.7 Ma (2σ) for KT02 ($n = 9$). The U–Pb ages of KT01 are comparable with 79±7 Ma (2σ) of the FT age from the same sample. The U–Pb ages of KT01 could constrain the maximum depositional age near the basal part of the Takikubo Formation, which was middle of the Middle Campanian (polarity chron C33n in the magnetostratigraphy).

1. Introduction

The Izumi Group is forearc basin deposits of the Late Cretaceous, which is narrowly distributed from western Shikoku to the Kii Peninsula along the northern side of the Median Tectonic Line. Macro-fossils (ammonoids and inoceramids) and micro-fossils (radiolarian assemblages) show that the depositional age of the Izumi Group are Campanian to Maastrichtian, Late Cretaceous (Suyari, 1973; Bando and Hashimoto, 1984; Yamasaki, 1987; Hashimoto *et al*., 2015). Those paleontological studies indicate that the depositional ages are younging toward the east. On the other hand, the paleocurrent directions in the main facies suggest the sediment derivation was mainly from east-northeast to west-southwest (Suyari, 1973; Miyata, 2004), as opposed to the younging direction of the depositional ages. These facts imply that the sedimentary basin of the Izumi Group had been developed in association with strike-slip fault activities (Ichikawa *et al*., 1981; Miyata, 1989; Noda and Toshimitsu, 2009). Progressive fault displacements along the pull-apart basins could migrate the basin depocenters (e.g., Noda, 2013).

Recently, details of the Late Cretaceous volcanic activities in the Sanyo Belt, which is situated at the north of the Izumi Group, were revealed by using U–Pb ages of igneous zircon grains in the felsic volcanic rocks and welded tuff beds (Sato, 2016; Sato *et al*., 2016a, b) (Fig. 1A). Therefore, radioisotope geochronological data in the Izumi Group may be useful to compare with the volcanic activities in magmatic fronts and to discuss temporal and spatial evolution of the sedimentary basin during the Late Cretaceous time. Although there are a few fission-track ages reported from the Izumi Group of Shikoku Island and the Kii Peninsula (Fig. 1A), no FT and U–Pb age data have been reported from eastern Shikoku to date.

This paper reports LA-ICP-MS U–Pb and FT ages of zircons in two felsic tuff beds of the Takikubo Formation (Yamasaki, 1986; Matsuura *et al*., 2002), which is the lower most formation of the main facies in the Izumi Group, eastern Shikoku. It is unclear whether or not the Takikubo Formation is an equivalent to the strata distributed in the Niihama district, central Shikoku (Fig. 1A). The depositional age of the Takikubo Formation was estimated to be of the lower Upper Campanian based on the radiolarian assemblages (Hashimoto *et al*., 2015; Noda and Kurihara, 2016).

---

[1] AIST, Geological Survey of Japan, Research Institute of Geology and Geoinformation

[2] Kyoto Fission-Track Co., Ltd.

[3] Division of Earth and Planetary Sciences, Kyoto University, Sakyo-ku, Kyoto 606-8502, Japan

Present address: Geochemical Research Center, Graduate School of Science, The University of Tokyo

[*] Corresponding author: A. Noda, Central 7,1-1-1 Higashi, Tsukuba, Ibaraki 305-8567, Japan. Email: a.noda@aist.go.jp
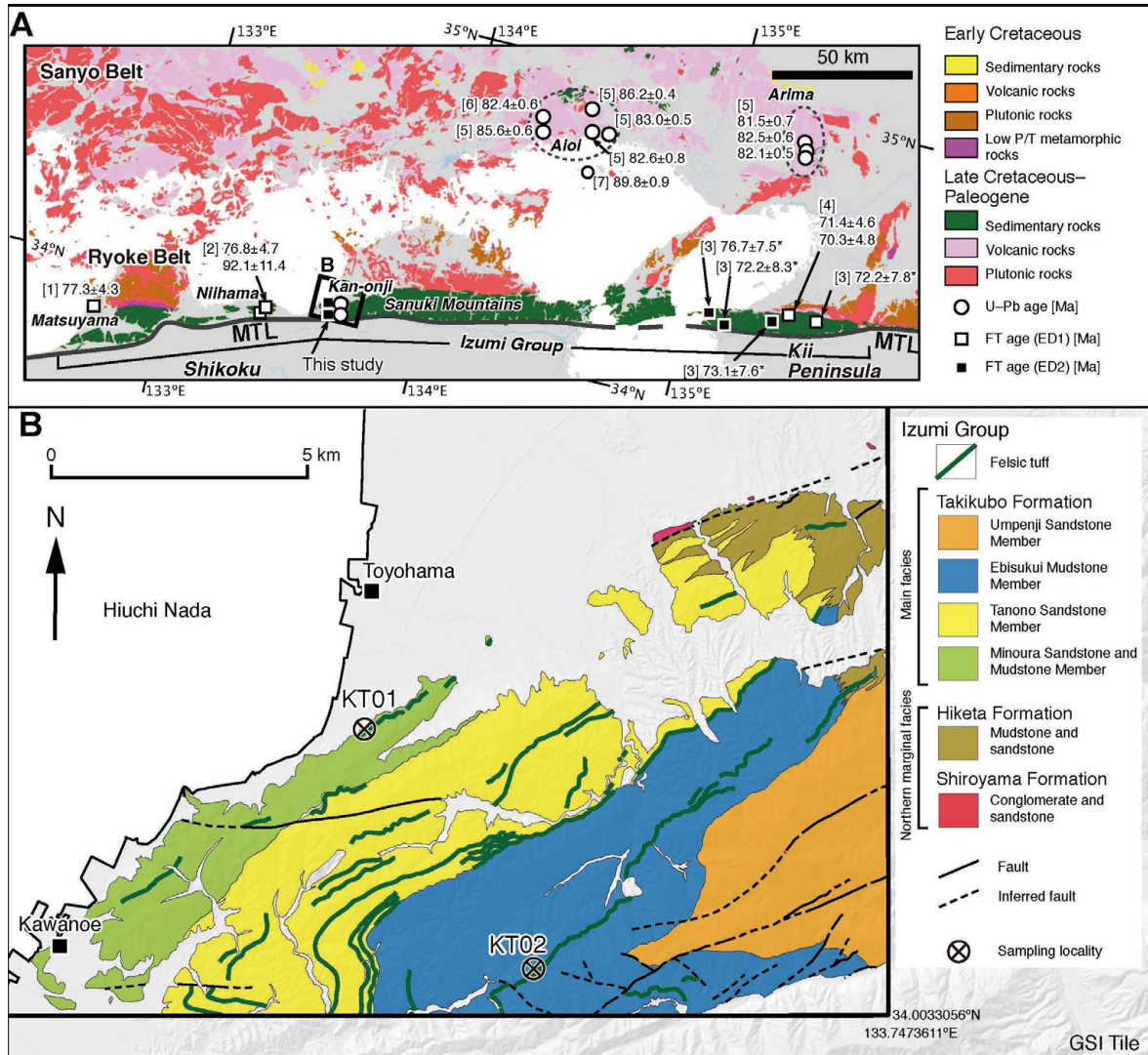
Fig. 1 A: Index map with U–Pb and fission-track (FT) ages (2σ) previously reported. FT ages include data obtained from the external detector method using internal surfaces (ED1) and external surfaces (ED2). The geological map is reproduced from the Seamless Digital Geological Map of Japan (Geological Survey of Japan, AIST, 2015). MTL means the Median Tectonic Line. References: [1] Sato *et al*. (2009), [2] Noda *et al*. (2010), [3] Miyata (2004), [4] Seike *et al*. (2013), [5] Sato *et al*. (2016a), [6] Sato *et al*. (2016b), and [7] Sato (2016). Asterisks (∗) denote fission-track ages recalculated from the original data using the decay constant of $\lambda_D = 1.55125 \times 10^{-10}$ yr^{-1} instead of 1.480×10^{-10} yr^{-1}. B: Localities of felsic tuff samples (KT01 and KT02) for U–Pb and FT age analyses. Geological map of the Izumi Group is based on Noda *et al*. (in press). Shaded topography is from the GSI Maps (http://maps.gsi.go.jp/). Thick lines indicate the area of extent of the Kan-onji district.

2. Materials and methods

Two samples (KT01 and KT02) were obtained from felsic tuff beds in the Takikubo Formation of the Izumi Group, the western margin of the Sanuki Mountains (Fig. 1 and Table 1). The tuff bed of KT01 was intercalated within a mudstone-dominated sequence in the Minoura Sandstone and Mudstone Member which is the lowest member of the Takikubo Formation (Noda *et al*., in press). KT01 was collected from a very thick (more than 15 m in thick) felsic tuff bed composed of thin- to thick-bedded tuffaceous mudstones and siltstones with normal grading

or parallel laminations (Fig. 2A). It was classified to vitric or crystal tuff showing light gray in color and silt- to fine sand-grained in size (Fig. 2B).

The sample KT02 was collected from a tuff bed in the Ebisukui Mudstone Member which is the third member of the Takikubo Formation. KT02 was obtained from a 7 m thick tuff bed which was composed of thin- to medium-bedded vitric tuff including fine- to coarse silt grains (Fig. 2C and D). The tuff bed included very fine sand-sized carbonaceous fragments parallel to the laminae. Although both samples of KT01 and KT02 were fine-grained, they contained euhedral to semi-euhedral zircon grains.

Table 1 List of samples analyzed. Longitude and latitude are based on WGS84 coordinate system.

Sample no.	ID	Longitude	Latitude	Date	Loc no.	Lithology	GSJ reg. no.
KT01	3499	133.63601	34.05375	2011-03-11	12	Felsic tuff	R108418
KT02	3287	133.67383	34.01164	2011-03-06	11	Felsic tuff	R108419
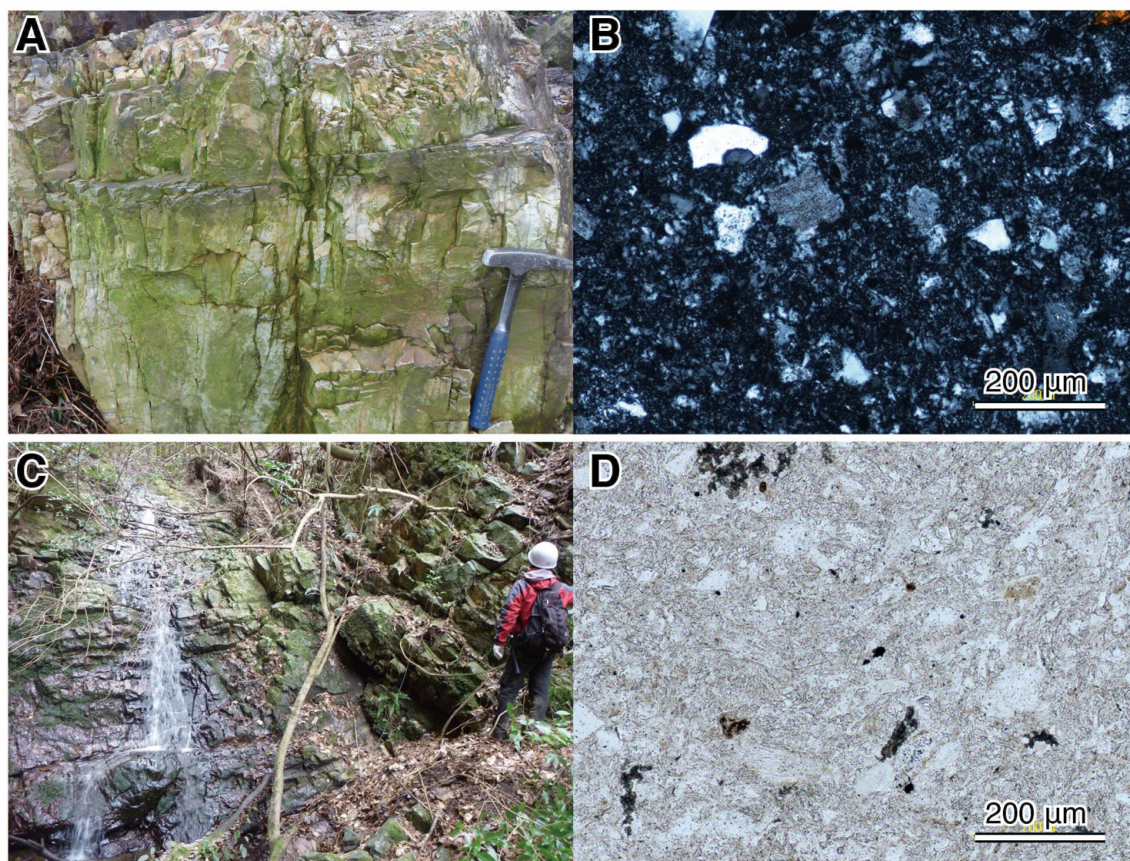
Fig. 2 A: Photograph of outcrop of the felsic tuff bed continued from the sampling locality of KT01. Wada, Toyohama-cho, Kan-onji, Kagawa. Length of the hammer is 33 cm. B: Photomicrograph of KT01 (crossed polar). C: Outcrop of KT02. Nakashita, Shimokawa-cho, Shikoku-Chuo, Ehime. D: Photomicrograph of KT02 (open polar).

The zircon grains were extracted from the samples; about 400 grains from 700 g for KT01 and 3,000 grains from 300 g for KT02. They were mounted on a PFA Teflon sheet with external natural surfaces exposed and etched by KOH–NaOH eutectic melts (KOH:NaOH = 1:1) at 225℃ during 19 hours. Because the zircon grains were very fine-grained, the measurements had to been conducted on the external surfaces of them instead of the internal ones. Spontaneous track density measurement was performed for 30 grains which were randomly selected using a high-resolution touch-monitor screen through a digital camera and an optical microscope (Danhara and Iwano, 2009).

U–Pb dating was performed on the same zircon grains with the track density counted ones by using LA- ICP-MS

system installed in the Division of Earth and Planetary Science of Kyoto University, Japan (Table 2). The LA-ICP-MS system was a Nu Instruments (Wrexham, UK) AttoM high-resolution magnetic sector field ICP-MS (e.g., Yokoyama *et al.*, 2011). The forward power of the ICP-MS was 1300 W (Iwano *et al.*, 2013). Helium gas was used as the carrier gas inside the ablation cell and was mixed with argon gas before entering the ICP-MS. Signal intensities for ^{202}Hg, ^{204}(Pb+Hg), ^{206}Pb, ^{207}Pb, ^{232}Th, and ^{238}U were obtained from 30 zircon crystals on each sample. The laser ablation system was a New Wave Research NWR-193 ArF laser-ablation system (Fremont, CA 94538, USA; e.g., Sakata *et al.*, 2014). The experimental conditions about the laser ablation include the wavelength (193 nm), the

Table 2 ICP-MS and laser operating conditions and data acquisition parameters.

Parameters	Value/Description
Laser ablation	
Model	New Wave Research NWR193
Laser type (Wave length)	Excimer ArF (193 nm)
Energy density	2.2 J/cm^2
Crater size	15 μm
Repetition rate	10 Hz
Carrier gas	He
ICP-MS	
Model	Nu Instruments AttoM
ICP-MS type	Magnetic sector field
Forward power	1300 W
Carrier gas	Ar
Ar gas flow rate	0.90 L min^{-1}
He gas flow rate	0.68 L min^{-1}
Scanning mode	Deflector jump
Data acquisition protocol	Batch
Integration time	8 s
Monitor isotopes	^{202}Hg, ^{204}Pb, ^{206}Pb, ^{207}Pb, ^{232}Th, ^{238}U
Primary standard	91500[*1] (U-Pb), Fish Canyon Tuff[*2] (FT)
Secondary standard	OD-3[*3]

[*1] Wiedenbeck *et al.* (1995); [*2] Danhara and Iwano (2013); [*3] Iwano *et al.* (2013)

ablation pit size (15 μm), and the repetition rate (10 Hz).

The possible contribution of common Pb was monitored from ^{204}Pb signal with (or plus) ^{204}Hg as an isobaric interference. The abundance of ^{204}Hg was calculated from blank-corrected ^{202}Hg on the basis of the natural ^{202}Hg/^{204}Hg ratio, which in turn was subtracted from 204 total to yield ^{204}Pb. We applied one-shot cleaning on the sample surfaces before the analysis in order to reduce the risk of contamination of common Pb. Instrumental bias for the unknown ^{206}Pb*/^{238}U ratio (asterisk denotes radiogenic) was corrected using a 91500 zircon standard (Wiedenbeck *et al.*, 1995).

The resultant U–Pb isotopic ratios and errors were used to calculate and plot concordia diagrams and histograms by Noda (2017). Details of the calculation for U–Pb ages and their errors are shown in Noda (2017). We excluded data whose error ellipses (2σ) do not overlap the concordia curves in the concordia diagrams as discordant data.

We also approximated FT ages for each grain by means of the ^{238}U signal data without internal standard correction based on Si or Zr. Age calibration was based on the zeta approach (Hurford, 1990a, b; Hasebe *et al.*, 2013) using the age standard Fish Canyon Tuff with the absolute FT age being 28.4±0.2 Ma (Danhara and Iwano, 2013) and ζ = 44.0±6.0 for 91500 zircon as a uranium standard.

3. Results

3. 1 U–Pb ages
The ^{206}Pb*/^{238}U, ^{207}Pb*/^{235}U, and ^{207}Pb*/^{206}Pb* ages of

zircons were calculated from analyzed isotopic ratios and decay constants.

KT01 The results of KT01 sample show a bimodal distribution whose ranges were roughly 75–85 Ma and 85–95 Ma; the younger population has a more conspicuous peak in the histogram (Fig. 3D; Table 3). We accepted grains whose error (3σ) of ^{206}Pb*/^{238}U ages includes the range of error (3σ) of the weighted mean of those in the younger cluster (Fig. 3C). By using the grains in the younger cluster (*n* = 23), the calculated ages are nearly consistent among the conventional concordia (^{207}Pb*/^{235}U–^{206}Pb*/^{238}U), Terra–Wasserburg concordia (^{238}U/^{206}Pb*–^{207}Pb*/^{206}Pb*), and the weighted mean of ^{206}Pb*/^{238}U ages, which are 78.3±0.5 Ma (2σ) of the concordia ages and 78.2±0.5 Ma (2σ) of the weighted mean of ^{206}Pb*/^{238}U ages (Fig. 3).

KT02 Most of the single grain ages in KT02 sample are concentrated in the older population of 85–95 Ma, but a small amount of grains are recognized within the younger one of 75–85 Ma (Fig. 4; Table 4). Because it is difficult to divide the clusters clearly by the dates, we chose grains in the same way as KT01 based on the error (3σ) of the weighted mean of ^{206}Pb*/^{238}U ages (Fig. 4C). The grains in this cluster (*n* = 9) yield 80.8±0.7 Ma (2σ) of the concordia ages (Fig. 4A and B) and 81.0±0.8 Ma (2σ) of the weighted mean of ^{206}Pb*/^{238}U ages (Fig. 4C). Because of the smaller numbers of accepted grains, these ages of KT02 show larger errors and MSWDs than those of KT01.

3. 2 FT ages
KT01 Individual FT ages were much more variable with larger errors than the U–Pb ages (Table 5). The weighted mean of the FT ages of 79±7 Ma (2σ), which was consistent with that of ^{206}Pb*/^{238}U age (78.2±0.5 Ma) of the same sample, was calculated with basically the same grains (*n* = 22) in the younger population of the U–Pb dating, except for one grain whose FT age was more than doubled the U–Pb age (Grain# 3 in Table 5).

KT02 The FT ages of zircon grains in the sample KT02 were also dispersed similar with KT01 (Table 6). The weighted mean of the FT ages was calculated by the selected grains (*n* = 8) in the younger population of the U–Pb age, except for one grain whose FT age was more than doubled the U–Pb age (Grain# 29 in Table 6). It was 69±10 Ma (2σ), which was younger than that of ^{206}Pb*/^{238}U ages (81.0±0.8 Ma) of the same sample.

4. Discussion

Because of the larger number of accepted grains and smaller errors and MSWDs, the U–Pb ages of KT01 are appropriate to constrain the maximum depositional age for the Minoura Sandstone and Mudstone Member in the Takikubo Formation. The lithology and sedimentary
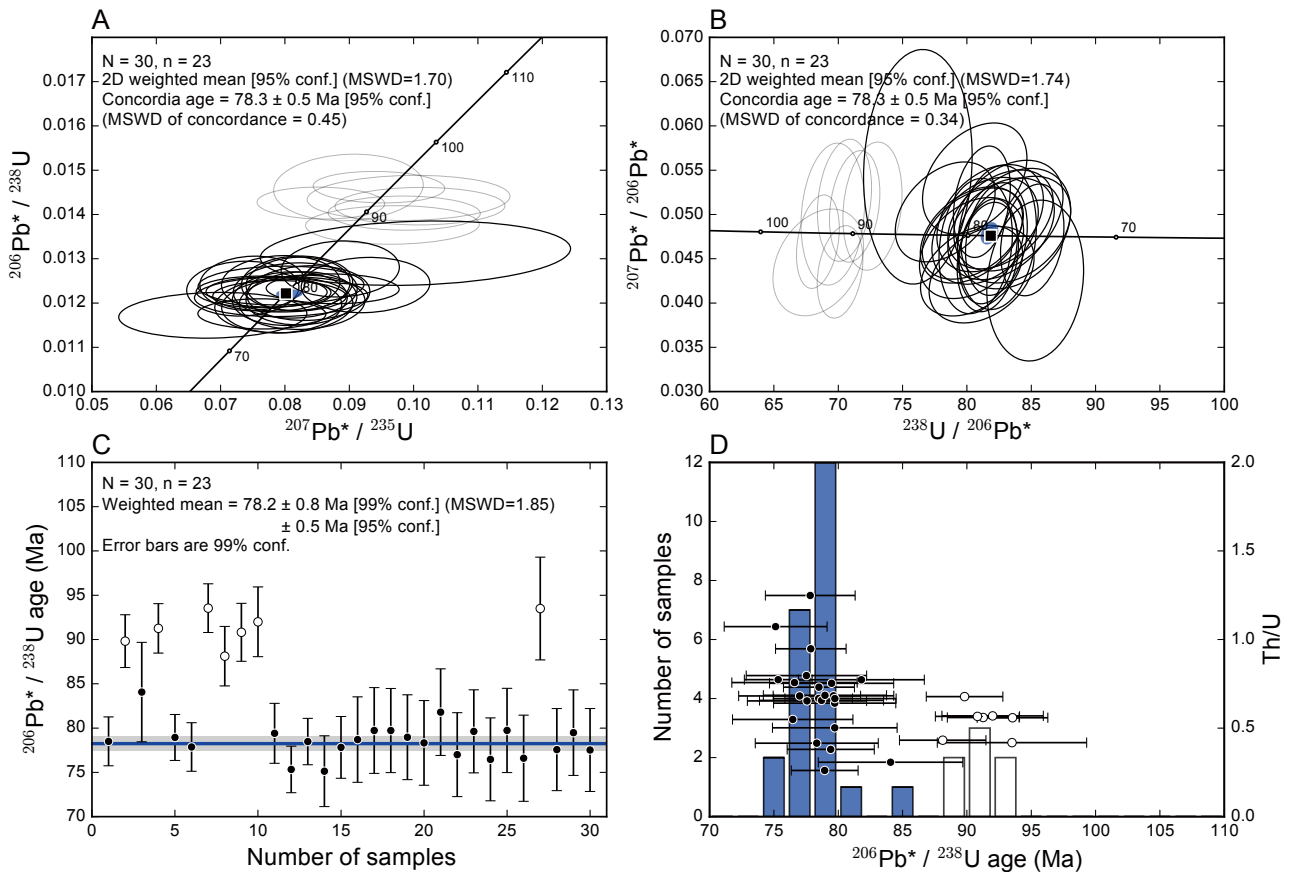
Fig. 3 Results of U–Pb dating of KT01. A: $^{207}Pb^*/^{235}U$–$^{206}Pb^*/^{238}U$ concordia diagram (Wetherill, 1956). Black solid and gray solid ellipses represent 2σ errors of accepted and excluded data points, respectively. Blue ellipse is a 95% confidence region of the two-dimensional weighted mean. Solid square shows the concordia age. N and n are numbers of total and accepted grains, respectively. B: Tera–Wasserburg concordia diagram (Tera and Wasserburg, 1972). Legends are same with A. C: one-dimensional weighted mean of $^{206}Pb^*/^{238}U$ ages (blue line) and its error of 3σ (gray band). Black and white circles with error bars (3σ) are accepted and excluded grains from the calculation, respectively. D: plots of Th/U ratios (right-hand vertical axis) with accepted (black circles) and excluded (white circles) data, and stacked histograms of $^{206}Pb^*/^{238}U$ ages (left-hand vertical axis) with accepted (blue bars) and excluded (white bars) data, respectively.

structures of the tuff beds, such as grading and parallel laminations, suggest the deposits were derived from volcaniclastic subaqueous gravity currents that transported pre-existing non-welded pyroclastic detritus from the land or shallow sea area (cf., Trofimovs et al., 2013). It means that the dates obtained from the zircon grains in the tuff beds do not indicate the depositional age directly. However, based on the very thick sediments in the Takikubo Formation (Noda et al., in press) and high productivity of pyroclastic detritus in the Sanyo Belt during this time (Sato et al., 2016a), it is probable that the zircon grains were transported from the source and deposited in the basin without a large time lag after the crystallization. Therefore, we approximate the depositional age of the Minoura Sandstone and Mudstone Member to 78.3±0.5 Ma (2σ) of the concordia ages or 78.2±0.5 Ma (2σ) of the weighted mean of $^{206}Pb^*/^{238}U$ ages for the younger cluster in KT01, which corresponds to middle Middle Campanian

and the polarity chron C33n in the magnetostratigraphy (Gradstein et al., 2012).

On the other hand, the U–Pb ages of KT02 from the Ebisukui Mudstone Member are older than those from KT01, although the tuff bed of KT02 is stratigraphically higher than that of KT01. Because tuff beds are considered to be not primary (pyroclastic) but secondary (volcaniclastic) deposits, the sample KT02 contained more recycled (older) grains. However, the depositional age of the Ebisukui Mudstone Member is at least younger than 80.8±0.7 Ma (2σ) based on the concordia ages of KT02.

FT ages of zircon grains are ideally equal to or younger than the U–Pb ages of them, if those crystals are supplied from volcanic eruptions. However, some FT ages in KT01 and KT02 show older ages than the U–Pb ages of the same grains. This discrepancy may be explained by two possibilities. The first is concentration of uranium measured in small spots (15 µm) by the LA-ICP-MS was

Table 3   Results of U–Pb age analysis of KT01. Asterisks (*) following the grain numbers mean excluded grains from calculation of concordia and weighted mean ages.

Sample KT01			Isotopic ratio						Discordance	Age [Ma]					
Grain#		Th/U	$^{207}Pb^*/^{206}Pb^*$	2σ	$^{206}Pb^*/^{238}U$	2σ	$^{207}Pb^*/^{235}U$	2σ	[%]	$^{206}Pb^*/^{238}U$	2σ	$^{207}Pb^*/^{235}U$	2σ	U [ppm]	Th [ppm]
1		0.73	0.0452	0.0050	0.01225	0.00029	0.0764	0.0082	concordant	78.5	1.9	74.7	8.3	269	197
2	*	0.68	0.0509	0.0051	0.01403	0.00031	0.0985	0.0095	concordant	89.8	2.0	95.4	9.6	276	187
3		0.31	0.0554	0.0107	0.01313	0.00058	0.1003	0.0194	concordant	84.1	3.8	97.0	19.5	56	17
4	*	0.56	0.0435	0.0042	0.01426	0.00029	0.0856	0.0080	concordant	91.3	1.9	83.4	8.1	345	193
5		0.26	0.0514	0.0051	0.01232	0.00027	0.0874	0.0083	concordant	78.9	1.7	85.1	8.4	321	84
6		0.95	0.0472	0.0051	0.01215	0.00029	0.0792	0.0084	concordant	77.9	1.8	77.4	8.4	270	256
7	*	0.56	0.0469	0.0042	0.01462	0.00029	0.0946	0.0082	concordant	93.5	1.8	91.8	8.3	379	212
8	*	0.43	0.0509	0.0058	0.01376	0.00035	0.0967	0.0109	concordant	88.1	2.3	93.7	11.0	193	83
9	*	0.57	0.0516	0.0055	0.01419	0.00034	0.1010	0.0106	concordant	90.8	2.2	97.7	10.7	218	123
10	*	0.57	0.0500	0.0065	0.01437	0.00041	0.0992	0.0127	concordant	92.0	2.6	96.0	12.8	139	79
11		0.38	0.0464	0.0061	0.01239	0.00035	0.0794	0.0104	concordant	79.4	2.3	77.6	10.5	163	62
12		0.77	0.0471	0.0051	0.01175	0.00027	0.0764	0.0080	concordant	75.3	1.8	74.8	8.1	285	220
13		0.67	0.0458	0.0048	0.01225	0.00027	0.0774	0.0078	concordant	78.5	1.8	75.7	7.9	309	206
14		1.07	0.0425	0.0073	0.01172	0.00042	0.0688	0.0118	concordant	75.1	2.7	67.5	11.9	103	110
15		1.25	0.0474	0.0065	0.01215	0.00036	0.0794	0.0108	concordant	77.8	2.3	77.6	10.9	148	184
16		0.66	0.0482	0.0049	0.01228	0.00050	0.0816	0.0077	concordant	78.7	3.2	79.6	7.8	272	179
17		0.50	0.0462	0.0046	0.01244	0.00050	0.0793	0.0074	concordant	79.7	3.2	77.5	7.5	289	145
18		0.64	0.0437	0.0041	0.01244	0.00049	0.0749	0.0066	concordant	79.7	3.2	73.4	6.7	347	222
19		0.69	0.0432	0.0044	0.01232	0.00050	0.0734	0.0070	concordant	79.0	3.2	72.0	7.1	296	203
20		0.41	0.0496	0.0049	0.01222	0.00050	0.0836	0.0077	concordant	78.3	3.2	81.5	7.8	283	117
21		0.77	0.0503	0.0045	0.01277	0.00051	0.0886	0.0074	concordant	81.8	3.3	86.2	7.5	329	255
22		0.68	0.0499	0.0050	0.01202	0.00049	0.0827	0.0078	concordant	77.0	3.2	80.6	7.9	268	183
23		0.68	0.0478	0.0041	0.01243	0.00049	0.0820	0.0065	concordant	79.6	3.1	80.1	6.6	395	269
24		0.55	0.0483	0.0048	0.01193	0.00049	0.0795	0.0075	concordant	76.5	3.1	77.7	7.6	282	155
25		0.67	0.0477	0.0044	0.01245	0.00050	0.0819	0.0070	concordant	79.7	3.2	79.9	7.0	342	228
26		0.76	0.0484	0.0055	0.01195	0.00051	0.0798	0.0086	concordant	76.6	3.3	78.0	8.7	212	161
27	*	0.42	0.0446	0.0048	0.01461	0.00060	0.0899	0.0094	concordant	93.5	3.9	87.4	9.5	206	86
28		0.65	0.0494	0.0045	0.01211	0.00048	0.0826	0.0069	concordant	77.6	3.1	80.5	7.0	348	227
29		0.75	0.0541	0.0050	0.01241	0.00050	0.0925	0.0080	concordant	79.5	3.2	89.9	8.1	291	219
30		0.80	0.0484	0.0046	0.01210	0.00049	0.0807	0.0072	concordant	77.5	3.1	78.8	7.3	314	250

Discordance is from $(1 - {^{206}Pb^*/^{238}U \text{ age}}/{^{207}Pb^*/^{235}U \text{ age}}) \times 100$.
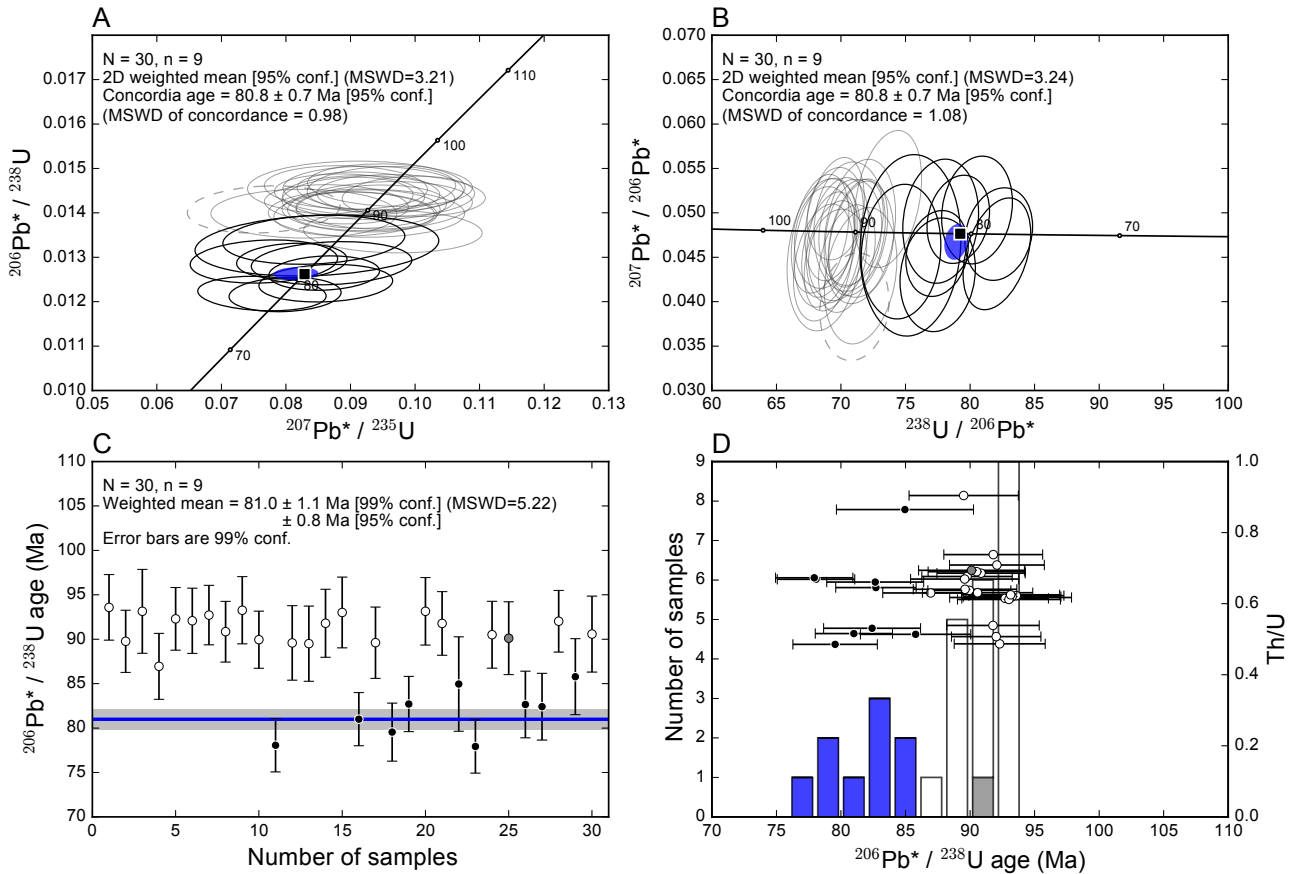
Fig. 4 Results of U–Pb dating of KT02. The discordant grain is represented by gray dashed ellipses (A and B), gray circle (C and D), and gray bar (D). Other legends are same with Fig. 3.

assumed to be the average concentrations of uranium in the grains. Because density of fission tracks in a grain depends on the average concentration of uranium in addition to duration of cooling, we might overestimate or underestimate the U concentrations for some grains. In the case of underestimation, apparent ages become older than the true ages, and vice versa.

The second is external effects of uranium outside or near the external surfaces of zircon grains, which mean contamination of fission-tracks originated from adjacent grains outside or enrichment of uranium along the external surfaces of the grains (Suzuki, 1988; Danhara *et al.*, 1991). Because we used the external surfaces for the FT analysis, such effects might lead to older FT ages than the true ages.

5. Conclusions

The analyzed samples of KT01 (Minoura Sandstone and Mudstone Member) and KT02 (Ebisukui Mudstone Member) from tuff beds of the Takikubo Formation, Izumi Group, in the Kan-onji district contain multiple populations composed chiefly of younger (75–85 Ma) and older (85–95 Ma) ages. By using grains in the younger

populations, the U–Pb ages of KT01 ($n = 23$) were 78.3±0.5 Ma (2σ) for the concordia ages and 78.2±0.5 Ma (2σ) for the weighted mean of $^{206}Pb^*/^{238}U$ ages. Those of KT02 ($n = 9$) were 80.8±0.7 Ma (2σ) and 81.0±0.8 Ma (2σ), respectively. The FT ages were 79±7 Ma (2σ) for KT01 ($n = 22$) and 69±10 Ma (2σ) for KT02 ($n = 8$). Given intensive magmatisms during the Late Cretaceous in the Sanyo Belt, the depositional ages of the basal part of the Takikubo Formation could be constrained by the U–Pb ages of KT01, which is middle Middle Campanian, corresponding to the polarity chron C33n in the magnetostratigraphy.

Table 4 Results of U-Pb age analysis of KT02.

Sample KT02

Grain#	Th/U	Isotopic ratio						Discordance [%]	Age [Ma]				U [ppm]	Th [ppm]
		$^{207}Pb^*/^{206}Pb$	2σ	$^{206}Pb^*/^{238}U$	2σ	$^{207}Pb^*/^{235}U$	2σ		$^{206}Pb^*/^{238}U$	2σ	$^{207}Pb^*/^{235}U$	2σ		
1 *	0.62	0.0476	0.0054	0.01462	0.00038	0.0961	0.0103	concordant	93.6	2.5	93.2	10.4	226	141
2 *	0.68	0.0472	0.0053	0.01402	0.00036	0.0914	0.0097	concordant	89.8	2.3	88.8	9.8	245	166
3 *	0.62	0.0453	0.0069	0.01455	0.00049	0.0909	0.0136	concordant	93.1	3.2	88.3	13.7	103	63
4 *	0.63	0.0516	0.0062	0.01358	0.00039	0.0966	0.0111	concordant	87.0	2.5	93.6	11.2	184	116
5 *	0.49	0.0452	0.0050	0.01442	0.00037	0.0898	0.0094	concordant	92.3	2.4	87.4	9.5	258	126
6 *	0.71	0.0493	0.0056	0.01439	0.00038	0.0978	0.0105	concordant	92.1	2.5	94.8	10.6	220	156
7 *	0.62	0.0464	0.0048	0.01449	0.00035	0.0928	0.0089	concordant	92.7	2.3	90.1	9.0	322	198
8 *	0.69	0.0449	0.0049	0.01419	0.00036	0.0878	0.0090	concordant	90.9	2.3	85.5	9.1	280	192
9 *	0.62	0.0444	0.0053	0.01457	0.00039	0.0893	0.0102	concordant	93.3	2.5	86.8	10.3	204	127
10 *	0.64	0.0476	0.0048	0.01405	0.00033	0.0923	0.0086	concordant	90.0	2.2	89.6	8.7	350	223
11	0.67	0.0454	0.0051	0.01218	0.00031	0.0763	0.0080	concordant	78.1	2.0	74.6	8.1	296	198
12 *	0.67	0.0479	0.0065	0.01399	0.00044	0.0925	0.0122	concordant	89.6	2.8	89.8	12.4	134	90
13 *	0.90	0.0429	0.0062	0.01398	0.00044	0.0828	0.0116	concordant	89.5	2.8	80.7	11.7	130	118
14 *	0.74	0.0469	0.0057	0.01434	0.00040	0.0928	0.0107	concordant	91.8	2.6	90.1	10.9	188	139
15 *	0.61	0.0466	0.0058	0.01453	0.00042	0.0935	0.0112	concordant	93.0	2.7	90.8	11.3	170	104
16	0.52	0.0493	0.0040	0.01264	0.00031	0.0859	0.0069	concordant	81.0	2.0	83.7	7.0	651	336
17 *	0.64	0.0471	0.0053	0.01400	0.00042	0.0910	0.0104	concordant	89.6	2.7	88.4	10.5	207	132
18	0.49	0.0503	0.0049	0.01242	0.00034	0.0862	0.0083	concordant	79.5	2.2	83.9	8.4	344	167
19	0.65	0.0454	0.0039	0.01291	0.00032	0.0809	0.0069	concordant	82.7	2.1	79.0	7.0	556	359
20 *	0.63	0.0472	0.0046	0.01455	0.00040	0.0948	0.0093	concordant	93.1	2.5	92.0	9.4	307	192
21 *	0.54	0.0453	0.0041	0.01434	0.00037	0.0895	0.0082	concordant	91.8	2.4	87.1	8.3	398	214
22	0.86	0.0463	0.0082	0.01327	0.00055	0.0848	0.0152	concordant	85.0	3.6	82.6	15.3	75	65
23	0.67	0.0476	0.0042	0.01216	0.00031	0.0799	0.0070	concordant	77.9	2.0	78.0	7.1	511	344
24 *	0.69	0.0478	0.0048	0.01414	0.00039	0.0932	0.0094	concordant	90.5	2.5	90.5	9.5	285	197
25 *	0.69	0.0394	0.0049	0.01408	0.00043	0.0765	0.0095	−20.3	90.1	2.8	74.9	9.6	194	134
26	0.66	0.0430	0.0051	0.01290	0.00039	0.0766	0.0092	concordant	82.7	2.5	74.9	9.3	212	140
27	0.53	0.0491	0.0056	0.01287	0.00039	0.0871	0.0100	concordant	82.4	2.5	84.8	10.1	210	112
28 *	0.51	0.0499	0.0042	0.01438	0.00036	0.0990	0.0083	concordant	92.0	2.3	95.8	8.4	494	251
29	0.51	0.0456	0.0061	0.01340	0.00045	0.0843	0.0113	concordant	85.8	2.9	82.2	11.5	146	75
30 *	0.63	0.0485	0.0059	0.01415	0.00045	0.0946	0.0115	concordant	90.6	2.9	91.7	11.6	168	106

Discordance is from $(1 - {}^{206}Pb^*/^{238}U\ age/^{207}Pb^*/^{235}U\ age) \times 100$.

Table 5   Preliminary results of fission-track dating of zircon samples in KT01 based on uranium data from LA-ICP-MS U–Pb dating.

Sample KT01	Fission Track Data			LA-ICP-MS-FT Age			
	N_s	A	ρ_s	U	Age (Ma)		
Grain#		(10^{-6}cm^2)	$(10^6\ \text{cm}^{-2})$	(ppm)	t_{FT}	$\pm 2\sigma$	
1	130	16.6	7.85	269	94 ±	30	
2	51	5.5	9.24	276	108 ±	42	*
3	87	14.7	5.91	56	336 ±	117	**
4	53	5.5	9.60	345	90 ±	35	*
5	45	7.4	6.11	322	62 ±	25	
6	37	5.5	6.70	271	80 ±	34	
7	111	8.3	13.41	380	114 ±	38	*
8	49	7.4	6.66	194	111 ±	44	*
9	59	5.5	10.69	218	158 ±	60	*
10	22	5.5	3.99	140	92 ±	47	*
11	94	16.6	5.68	163	112 ±	38	
12	37	5.5	6.70	285	76 ±	33	
13	79	9.2	8.59	309	90 ±	32	
14	41	9.2	4.46	103	139 ±	58	
15	42	11.0	3.80	148	83 ±	34	
16	35	3.7	9.51	277	111 ±	48	
17	43	5.5	7.79	295	86 ±	35	
18	106	9.2	11.52	353	105 ±	35	
19	44	6.4	6.83	302	73 ±	30	
20	45	7.4	6.11	288	69 ±	28	
21	49	7.4	6.66	336	64 ±	25	
22	47	4.6	10.22	273	121 ±	48	
23	54	7.4	7.34	402	59 ±	23	
24	23	3.7	6.25	287	71 ±	35	
25	44	5.5	7.97	348	74 ±	30	
26	12	1.8	6.52	216	98 ±	63	
27	47	8.3	5.68	209	88 ±	35	*
28	33	3.7	8.97	354	82 ±	36	
29	28	3.7	7.61	296	83 ±	39	
30	31	4.6	6.74	319	68 ±	31	
				Weighted mean (n = 22):	**79 ±**	**7**	

N_s Number of spontaneous fission tracks counted

A Counting area

ρ_s Spontaneous track density $(= N_s/A)$

U Uranium concentration in ppm

FT age $t_{FT} = (1/\lambda_D)\ln(1+\lambda_D\zeta_{MS}g\rho_s/m_i)$ (see Hasebe *et al.*, 2013)

λ_D: Total decay constant of ^{238}U $(= 1.55125 \times 10^{-10}\ \text{y}^{-1})$

ζ_{MS}: Zeta calibration factor determined by LA-ICP-MS

$\zeta_{MS} \pm 1\sigma = 44.0 \pm 6.0$

g: Geometry factor (=1)

$m_i = (^{238}\text{U}/^{29}\text{Si})_{sample}/(^{238}\text{U}/^{29}\text{Si})_{standard}$ for zircon grain i

$^{29}\text{Si}_{sample} = ^{29}\text{Si}_{91500\ standard}$ was supposed.

The count-area-corrected ^{238}U signal intensity was used.

Age standard   Fish Canyon Tuff (28.4±0.2 Ma: Danhara and Iwano, 2013)

Uranium standard   Nancy 91500, 74 ppm U

* Rejected data by U–Pb dating

** Manually excluded datum as an outlier

Table 6   Preliminary results of fission-track dating of zircon samples in KT02 based on uranium data from LA-ICP-MS U–Pb dating.

Sample KT02	Fission Track Data			LA-ICP-MS-FT Age			
	N_s	A	ρ_s	U	Age (Ma)		
Grain#		$(10^{-6} cm^2)$	$(10^6 cm^{-2})$	(ppm)	t_{FT}	$\pm 2\sigma$	
1	88	9.2	9.57	231	134 ±	46	*
2	131	16.6	7.91	250	102 ±	33	*
3	41	7.4	5.57	105	171 ±	71	*
4	30	5.5	5.43	188	94 ±	43	*
5	24	3.7	6.52	263	80 ±	39	*
6	41	5.5	7.43	224	107 ±	44	*
7	244	27.6	8.84	329	87 ±	26	*
8	103	8.3	12.44	285	141 ±	47	*
9	83	8.3	10.02	208	155 ±	54	*
10	97	7.4	13.18	357	119 ±	41	*
11	47	5.5	8.51	302	91 ±	37	
12	20	3.7	5.43	137	128 ±	67	*
13	33	3.7	8.97	133	217 ±	97	*
14	40	5.5	7.25	192	122 ±	51	*
15	28	5.5	5.07	173	95 ±	44	*
16	74	5.5	13.41	645	67 ±	24	
17	41	7.4	5.57	205	88 ±	37	*
18	44	5.5	7.97	341	76 ±	31	
19	74	7.4	10.05	551	59 ±	21	
20	28	2.8	10.14	303	108 ±	51	*
21	109	9.2	11.85	394	97 ±	32	*
22	16	5.5	2.90	74	126 ±	72	
23	127	13.8	9.20	506	59 ±	19	
24	73	11.0	6.61	282	76 ±	27	*
25	51	5.5	9.24	192	155 ±	61	*
26	39	7.4	5.30	210	82 ±	34	
27	38	7.4	5.16	208	80 ±	34	
28	36	3.7	9.78	489	65 ±	28	*
29	74	8.3	8.94	144	199 ±	71	**
30	61	8.3	7.37	166	143 ±	54	*
				Weighted mean (n = 8):	**69 ±**	**10**	

N_s Number of spontaneous fission tracks counted

A Counting area

ρ_s Spontaneous track density (= N_s/A)

U Uranium concentration in ppm

FT age $t_{FT} = (1/\lambda_D)\ln(1+\lambda_D\zeta_{MS}g\rho_s/m_i)$ (see Hasebe *et al.*, 2013)

λ_D: Total decay constant of ^{238}U (= 1.55125×10^{-10} y^{-1})

ζ_{MS}: Zeta calibration factor determined by LA-ICP-MS

$\zeta_{MS} \pm 1\sigma = 44.0 \pm 6.0$

g: Geometry factor (=1)

$m_i = (^{238}U/^{29}Si)_{sample}/(^{238}U/^{29}Si)_{standard}$ for zircon grain *i*

$^{29}Si_{sample} = {}^{29}Si_{91500\ standard}$ was supposed.

The count-area-corrected ^{238}U signal intensity was used.

Age standard   Fish Canyon Tuff (28.4±0.2 Ma: Danhara and Iwano, 2013)

Uranium standard   Nancy 91500, 74 ppm U

* Rejected data by U–Pb dating

** Manually excluded datum as an outlier

References

Bando, Y. and Hashimoto, H. (1984) Biostratigraphy and ammonite fauna of the Izumi Group (Late Cretaceous) in the Asan Mountains. *Mem. Fac. Educ., Kagawa Univ., Part II*, **34**, 1–16, (in Japanese with English abstract).

Danhara, T. and Iwano, H. (2009) Determination of zeta values for fission-track age calibration using thermal neutron irradiation at the JRR-3 reactor of JAEA, Japan. *Jour. Geol. Soc. Japan*, **115**, 141–145.

Danhara, T. and Iwano, H. (2013) A review of the present state of the absolute calibration for zircon fission track geochronometry using the external detector method. *Island Arc*, **22**, 264–279.

Danhara, T., Kasuya, M., Iwano, H. and Yamashita, T. (1991) Fission-track age calibration using internal and external surfaces of zircon. *Jour. Geol. Soc. Japan*, **97**, 977–985.

Geological Survey of Japan, AIST ed. (2015) *Seamless digital geological map of Japan 1:200,000, May 29, 2015 version*, Geol. Surv. Japan, AIST, (accessed 2016-05-29).

Gradstein, F. M., Ogg, J. G., Schmitz, M. D. and Ogg, G. M. eds. (2012) *The Geologic Time Scale*, Elsevier, Amsterdam, Netherland, 1144p.

Hasebe, N., Tamura, A. and Arai, S. (2013) Zeta equivalent fission-track dating using LA-ICP-MS and examples with simultaneous U–Pb dating. *Island Arc*, **22**, 280–291.

Hashimoto, H., Ishida, K., Yamasaki, T., Tsujino, Y. and Kozai, T. (2015) Revised radiolarian zonation of the Upper Cretaceous Izumi inter-arc basin (SW Japan). *Rev. Micropaléontol.*, **58**, 29–50.

Hurford, A. J. (1990a) International union of geological sciences subcommission on geochronology recommendation for the standardization of fission track dating calibration and data reporting. I*nt. Jour. Radiat. Appl. Instrum. Part D.*, **17**, 233–236.

Hurford, A. J. (1990b) Standardization of fission track dating calibration; recommendation by the Fission Track Working Group of the I.U.G.S. Subcommission on Geochronology. *Chem. Geol.*, **80**, 171–178.

Ichikawa, K., Miyata, T. and Shinohara, M. (1981) Eastward stepwise shift of the Izumi sedimentary basin with reference to the movement picture of the Median Tectonic Line. *In Proceedings of the Kansai Branch*, 11–12, Geol. Soc. Japan, (in Japanese).

Iwano, H., Orihashi, Y., Hirata, T., Ogasawara, M., Danhara, T., Horie, K., Hasebe, N., Sueoka, S., Tamura, A., Hayasaka, Y., Katsube, A., Ito, H., Tani, K., Kimura, J.-I., Chang, Q., Kouchi, Y., Haruta, Y. and Yamamoto, K. (2013) An inter-laboratory evaluation of OD-3 zircon for use as a secondary U–Pb dating standard. *Island Arc*, **22** 382–394.

Matsuura, H., Kurimoto, C., Yoshida, F., Saito, Y., Makimoto, H., Toshimitsu, S., Iwaya, T., Komazawa,

M. and Hiroshima, T. (2002) *Okayama and Marugame*, Geological Map of Japan 1:200,000, Geol. Surv. Japan, AIST, Tsukuba, Japan.

Miyata, T. (1989) Cretaceous Izumi sedimentary basin: Pullaparts with duplex structure along Median Tectonic Line, southwest Japan. *In Abstracts*, the 28th International Geological Congress, Washington, DC, United States, p. 447.

Miyata, T. (2004) The Upper Cretaceous Izumi Group. *In Geology of the Kokawa district*, Quadrangle Series, 1:50,000, Geol. Surv. Japan, AIST, 28–40, (in Japanese).

Noda, A. (2013) Strike-slip basin: Its configuration and sedimentary facies. *In* Itoh, Y. ed. *Mechanism of Sedimentary Basin Formation: Multidisciplinary Approach on Active Plate Margins*, InTech, Rijeka, Croatia, 28–57, doi: 10.5772/56593.

Noda, A. (2017) A new tool for calculation and visualization of U–Pb age data: UPbplot.py. *Bull. Geol. Surv. Japan.*, **68**, 131–140.

Noda, A. and Kurihara, T. (2016) Late Cretaceous radiolarian assemblages obtained from the Izumi Group in the Kan-onji district, eastern Shikoku, Japan. *Bull. Geol. Surv. Japan*, **67**, 119–131 (in Japanese with English abstract).

Noda, A. and Toshimitsu, S. (2009) Backward stacking of submarine channel-fan successions controlled by strike-slip faulting: The Izumi Group (Cretaceous), southwest Japan. *Lithosphere*, **1**, 41–59.

Noda, A., Toshimitsu, S., Kurihara, T., and Iwano, H. (2010) Stratigraphy and depositional age of the Izumi Group, Niihama area, central Shikoku, Japan. *Jour. Geol. Soc. Japan*, **116**, 99–113, (in Japanese with English abstract).

Noda, A., Ueki, T., Kawabata, H., Matsuura, H. and Aoya, M. (in press) *Geology of Kan-onji district*, Quadrangle Series, 1:50,000, Geol. Surv. Japan, AIST, (in Japanese with English abstract).

Sakata, S., Hattori, K., Iwano, H., Yokoyama, T. D., Danhara, T. and Hirata, T. (2014) Determination of U–Pb ages for young zircons using Laser Ablation-ICP-Mass Spectrometry coupled with an ion detection attenuator device. *Geostand. Geoanal. Res.*, **38**, 409–420.

Sato, D. (2016) Zircon U–Pb and fission-track ages of Late Cretaceous volcanic rocks of the Ieshima Islands, southwest Japan. *Japan. Mag. Mineral. Petrol. Sci.*, **45**, 53–61, (in Japanese with English abstract).

Sato, D., Matsuura, H. and Yamamoto, T. (2016a) Timing of the Late Cretaceous ignimbrite flare-up at the eastern margin of the Eurasian Plate: New zircon U–Pb ages from the Aioi–Arima–Koto region of SW Japan. *Jour. Volcanol. Geotherm. Res.*, **310**, 89–97.

Sato, D., Yamamoto, T. and Takagi, T. (2016b) *Geology of the Banshu-Ako district*, Quadrangle Series, 1:50,000, Geol. Surv. Japan, AIST, 68p. (in Japanese with English abstract, 3p).

Sato, T., Kitagawa, Y., Koizumi, N., Natori, J., NIshimura, Y., Haga, M., Hirooka, S. and Tanikawa, S. (2009) *Geological data of the GSJ boring core at the Matsuyama Observation Station*, Open-File Report, no. 504, Geol. Surv. Japan, AIST, (in Japanese).

Seike, K., Iwano, H., Danhara, T. and Hirano, H. (2013) Tectonics of the Ryoke–Izumi belt of the Izumi Mountains, Southwest Japan from thermochronological data. *Jour. Geol. Soc. Japan*, **119**, 759–775, (in Japanese with English abstract).

Suyari, K. (1973) On the lithofacies and the correlation of the Izumi Group of the Asan Mountain Range, Shikoku. *Sci. Rep. Tohoku Univ., 2nd ser. (Geol.), Special Volume*, **6**, 489–495, (in Japanese with English abstract).

Suzuki, K. (1988) Heterogeneous distribution of Uranium within zircon grains: Implication for fission-track dating. *Jour. Geol. Soc. Japan*, **94**, 1–10.

Tera, F. and Wasserburg, G. J. (1972) U-Th-Pb systematics in three Apollo 14 basalts and the problem of initial Pb in lunar rocks. *Earth Planet. Sci. Lett.*, **14**, 281–304.

Trofimovs, J., Talling, P. J., Fisher, J. K., Sparks, R. S. J., Watt, S. F. L., Hart, M. B., Smart, C. W., Le Friant, A., Cassidy, M., Moreton, S. G. and Leng, M. J. (2013) Timing, origin and emplacement dynamics of mass flows offshore of SE Montserrat in the last 110 ka: Implications for landslide and tsunami hazards, eruption history, and volcanic island evolution. *Geochem. Geophys. Geosyst.*, **14**, 385–406.

Wetherill, G. W. (1956) Discordant uranium-lead ages, I. *Eos, Trans. Amer. Geophys. Union*, **37**, 320–326.

Wiedenbeck, M., Allé, P., Corfu, F., Griffin, W. L., Meier, M., Oberli, F., Quadt, A. V., Roddick, J. C. and Spiegel, W. (1995) Three natural zircon standards for U-Th-Pb, Lu-Hf, trace element and REE analyses. *Geostand. Newsl.*, **19**, 1–23.

Yamasaki, T. (1986) Sedimentological study of the Izumi Group in the northern part of Shikoku, Japan. *Sci. Rep. Tohoku Univ., 2nd ser. (Geol.)*, **56**, 43–70.

Yamasaki, T. (1987) Radiolarian assemblages of the Izumi Group in Shikoku and western Awaji Island, Southwest Japan. *Jour. Geol. Soc. Japan*, **93**, 403–417, (in Japanese with English abstract).

Yokoyama, T. D., Suzuki, T., Kon, Y. and Hirata, T. (2011) Determinations of rare earth element abundance and U-Pb age of zircons using multispot Laser Ablation-Inductively Coupled Plasma Mass Spectrometry. *Anal. Chem.*, **83**, 8892–8899.

四国東部の観音寺地域に分布する和泉層群滝久保層の珪長質凝灰岩の
LA-ICP-MS による U–Pb 年代とフィッション・トラック年代

野田　篤・檀原　徹・岩野英樹・平田岳史

要　旨

四国東部の観音寺地域に分布する和泉層群滝久保層の堆積年代を推定するために，挟在する珪長質凝灰岩の2試料（KT01とKT02）について，LA-ICP-MSによる砕屑性ジルコン粒子のU-Pb年代とフィッション・トラック（FT）年代を測定した．各試料について，それぞれ30粒子を測定した結果，その年代分布は主に若い年代集団（75–85 Ma）と古い年代集団（85–95 Ma）から構成されることが分かった．若い年代集団に基づくコンコーディア年代は，KT01（採用粒子数 n＝23）では78.3±0.5 Ma（2σ），KT02（n＝9）では 80.8±0.7 Ma（2σ）であった．また，KT01のU-Pb年代は，同じ粒子による79±7 Ma（2σ）のFT年代とほぼ一致する．これらの結果から推定される滝久保層の堆積年代は，後期白亜紀の中期カンパニアン期の中頃（古地磁気極性 C33n）である．

Notes and Comments

A new tool for calculation and visualization of U–Pb age data: UPbplot.py

Atsushi Noda[1,*]

Abstract: This paper presents usages, examples, and mathematical backgrounds of a Python script, UPbplot.py, which was newly developed for calculation and visualization of U–Pb age data. The script is a collection of various functions to deal with the one- and two-dimensional weighted means, concordia ages, and concordia-intercept ages on the conventional (Wetherill) and Tera–Wasserburg concordia diagrams for U–Pb age data. This script can calculate those ages and output images including concordia diagrams, bar plots, and histograms.

1. Introduction

For visualization of geochronological data, such as uranium–lead (U–Pb) ages, Isoplot (Ludwig, 2012) has been successfully used for a long time. Unfortunately, because it was written in Microsoft® Visual Basic®, there are some dependent problems for specific versions of Excel® or operating systems. Although a new open-source project (e.g., Topsoil; Bowring and PI CIRDLES. org Open Source Development Team, 2016) is now developing to replace Isoplot, it can only deal with the conventional diagrams at present. In order to overcome such problems, a new script, UPbplot.py (Noda, 2016), was written in Python which is a commonly used language in the scientific community. It enables us to

- plot scattered data with error ellipses on conventional ($^{207}Pb^*/^{235}U$–$^{206}Pb^*/^{238}U$; Wetherill, 1956) and Tera–Wasserburg ($^{207}Pb^*/^{206}Pb^*$–$^{238}U/^{206}Pb^*$; Tera and Wasserburg, 1972) concordia diagrams,
- calculate the one- or two-dimensional weighted mean, concordia, and concordia-intercept ages with errors on both concordia diagrams, and
- work on any operating systems which can run Python scripts.

The purposes of this short article are to introduce the usage of this script, show examples of output images, and explain details of the calculations used in the script.

2. Usage

2.1 Preparations

The script was written in Python version 2.7 series. If the script is run by Python version 3 series, some modifications are required by reference to the comments in the script.

Mandatory libraries of matplotlib (Hunter, 2007), pandas (McKinney, 2010), and SciPy (Jones *et al*., 2001–) should be installed (Table 1). When the script is executed in the GUI mode, further libraries of PySide, wxPython, and quickgui will be required (Table 1).

Table 1　List of libraries used in the script of UPbplot.py.

Library	Version	License	URL
matplotlib[1]	2.0.0	PSF BSD[2]	http://matplotlib.org
Numpy[1]	1.12.0	BSD3[3]	http://www.numpy.org
pandas[1]	0.19.2	BSD3	http://pandas.pydata.org
SciPy[1]	0.18.1	BSD3	https://www.scipy.org
PySide	1.2.2	LGPLv2.1[4]	https://wiki.qt.io/PySide
quickgui	1.5.6	MIT[5]	https://pypi.python.org/pypi/quickgui
wxPython	3.0.2.0	wxWindows-3.1[6]	http://www.wxpython.org

[1] Mandatory libraries
[2] http://matplotlib.org/users/license.html
[3] https://opensource.org/licenses/BSD-3-Clause
[4] https://opensource.org/licenses/LGPL-2.1
[5] https://opensource.org/licenses/mit-license.php
[6] https://www.wxwidgets.org/about/licence/

[1] AIST, Geological Survey of Japan, Research Institute of Geology and Geoinformation

[*] Corresponding author: A. Noda,Central 7,1-1-1 Higashi, Tsukuba, Ibaraki 305-8567, Japan. Email: a.noda@aist.go.jp

2.2 Data and configuration files

Data files (extension of file name must be .csv) are comma- or tab-separated data sheets that must have at least six columns for isotopic ratios of $^{207}Pb^*/^{235}U$, $^{206}Pb^*/^{238}U$, $^{207}Pb^*/^{206}Pb^*$, and their errors (1σ or 2σ). Optional columns of Th/U ratios and their errors are also acceptable.

Configuration files (.cfg as extension) are needed to run the script, which define many variables used in the script. At first, it is recommended to copy and modify example files in Noda (2016).

2.3 Command-line mode

2.3.1 Options

The script accepts some options as arguments.

```
Options:
 -h, --help              Show this help message and exit
 -i FILE, --in=FILE      Name of input data file(*.csv)
 -c FILE, --cfg=FILE     Name of configuration file
                         (*.cfg)
 -o FILE, --out=FILE     Name of output file (*.pdf,
                         when DRIVER is pdf)
 -g, --gui               Use GUI for file selection
 -n, --no-gui            Do not use GUI (default)
 -d DRIVER,              Choose driver [pdf (default),
    --driver=DRIVER      qt4agg]
 -f, --force-overwrite   Force overwrite the pre-
                         existing pdf
```

2.3.2 Running the script

If the script (UPbplot.py), data (data1.csv), and configuration (data1.cfg) files are stored in the current working directory, type like below in a terminal window.

```
python UPbplot.py -i data1.csv
```

Name of the configuration file is assumed to be the same with that of the data file as default, but a different name can be set by using -c option. The following command line means that the script do not use GUI mode (-n), input data file name is data1.csv (-i), configuration file name is all.cfg (-c), pdf is the driver, and the pre-existing pdf file will be overwritten without any notice (-f).

```
python UPbplot.py -n -i data1.csv -c all.cfg -d pdf -f
```

2.3.3 Output

After the script successfully works in the command-line mode, two types of output (standard output and a pdf file) will be given by this script. The standard output includes the file names, first few lines of the input data, and results of calculation related to generate diagrams (Figure 1). A pdf file has four diagrams (A, B, C and D) in one file. The diagrams A and B are designated for plots of the measured isotopic ratios with error ellipses on the conventional (A) and Tera–Wasserburg (B) concordia diagrams, respectively. Decay constants used

in this script are listed in Appendix A.1. Error ellipses for confidence regions of the measurements are illustrated by using covariances between the coordinates in each diagram (Appendix A.2). The script optionally plots two-dimensional (2D) weighted means (Appendix A.5), concordia ages (Appendix A.6), and regression lines (Appendix A.7), and concordia-intercept ages (Appendix A.7) with the confidence regions. Configuration files can set ranges of axes, styles of symbols and lines, labels, and confidence levels (e.g., 68%, 95%, or 99%) for error ellipses, weighted means, concordia ages, and concordia-intercept ages. Several examples in Noda (2016) may be helpful to customize diagrams.

The diagram C shows bar plots of a selected age from among $^{206}Pb^*/^{238}U$, $^{207}Pb^*/^{235}U$, and $^{207}Pb^*/^{206}Pb^*$ ages with the one-dimensional weighted mean (Appendix A.3). The mean square of the weighted deviation (MSWD) can also be calculated (Appendix A.4).

The diagram D is a histogram of the age used in the diagram C with or without kernel density estimations (KDE), which is a way to estimate the probability density function (PDF) of a random variable in a non-parametric way. In this script, the function of stats.gaussian_kde in SciPy is used to obtain the KDE (SciPy.org, 2016). If the input data file has Th/U ratios, they can be plotted in this diagram.

Figure 2 is an example of plots for the Cretaceous granitoids in the Abukuma Highland (Ishihara and Orihashi, 2015). In the diagrams A and B, solid red, dashed blue, and dotted black ellipses represent 95% confidence regions of accepted, discordant (>10%), and manually excluded measurements, respectively. Calculation of the discordance is explained in Appendix A.8. Concordia ages are indicated by solid circles on the concordia curves, which are calculated from the accepted data (red ellipses in this case). Numbers of all (N) and accepted (n) data points, calculated ages, errors, and MSWD are listed in the upper left sides of the diagrams.

Figure 2C shows the weighted mean (blue line) of $^{206}Pb^*/^{238}U$ ages with the 95% confidence region (shaded band). Red square, gray and open circles with error bars are accepted, discordant, and excluded data, respectively. Figure 2D contains a histogram (left side vertical axis) for the same age with the diagram C, which is stacked by blue (accepted), gray (discordant), and open (excluded) boxes. The Th/U ratios (right side vertical axis) are plotted by the same symbols with those in the diagram C. In addition, kernel-density estimations of all (dashed red) and accepted (solid red) data are also shown in the diagram D.

Figure 3 is another example of the output image for the Cretaceous granitic rocks in the Setouchi area (Iida *et al*., 2015). In addition to Figure 2, the diagrams A and B include confidence regions of 2D weighted means (green ellipses) of the accepted measurements and the regression lines with the errors (thick blue lines with purple zones). Solid black and dashed gray ellipses represent confidence regions of accepted and discordant data, respectively.

```
Terminal — -zsh — 80×44
[% UPbplot.py -i Ishihara2015ia_TableS1_68A-64.csv -f
Output file Ishihara2015ia_TableS1_68A-64.pdf already exists.
-----------------------------------------------------------
Data filename is Ishihara2015ia_TableS1_68A-64.csv
Configuration filename is Ishihara2015ia_TableS1_68A-64.cfg
Output filename is Ishihara2015ia_TableS1_68A-64.pdf
# Input data (first 5 lines)
-----------------------------------------------------------
207Pb/235U  2s        206Pb/238U  2s        207Pb/206Pb  2s
column[9]   column[11] column[6]  column[8] column[3]   column[5]
-----------------------------------------------------------
207Pb/235U  1s        206Pb/238U  1s        207Pb/206Pb  1s
-----------------------------------------------------------
0.11190     0.00280   0.01664     0.00034   0.04880     0.00070
0.11770     0.00295   0.01725     0.00035   0.04950     0.00070
0.11380     0.00265   0.01681     0.00034   0.04910     0.00060
0.11740     0.00395   0.01753     0.00034   0.04860     0.00135
0.18110     0.00410   0.01871     0.00036   0.07020     0.00085
-----------------------------------------------------------
Discordant data (> 10.00%) are excluded from analysis.
Discordance is calculated by 100*(1-([206Pb/238U age]/[207Pb/235U age]))
Discordant data points are
4 29.29%
6 54.01%
12 11.12%
20 54.07%
22 26.21%
Manually excluded data points are [13, 19]
Accepted data points are [ 0  1  2  3  5  7  8  9 10 11 14 15 16 17 18 21 23]
-----------------------------------------------------------
Plotting A: Conventional concordia diagram
Error ellipses are 95% for data points
Concordia age = 109.70 ± 1.04 Ma [95% conf.]
    (MSWD of concordance=17.78, p(chi^2)=0.00)
Plotting B: Tera-Wasserburg concordia diagram
Concordia age = 109.70 ± 1.04 Ma [95% conf.]
    (MSWD of concordance=17.23, p(chi^2)=0.00)
Plotting C: One-dimensional bar plot
1D weighted mean age = 109.72 ± 1.05 Ma [95% conf.] (MSDW=2.34)
Plotting D: Histogram
All done.
Saving Ishihara2015ia_TableS1_68A-64.pdf
%
```

Figure 1   An example of standard output in a terminal window. This output includes file names to be processed, a part of the input data, and results of calculation. In this case, the script was applied to the data of sample 68A-64 in Ishihara and Orihashi (2015).

Other symbols and lines are the same with those in Figure 2.

2.4   GUI mode

To run the script as the GUI mode, add -g option in the command line. A new window will be opened to select an input data file. Please notice that the GUI mode cannot accept any command-line options related with file names (-i, -c, and -o) at the present version of the script. After the selection of input data and/or configuration files, a message window will pop up to show the calculation process.

If PySide is installed and the user's matplotlib has a backend of qt4agg, the script accepts an option of "-d qt4agg" as the driver.

```
python UPbplot.py -g -d qt4agg
```

This driver enables us to modify ranges of axes, labels, and styles of lines, interactively. To output images in the GUI mode, press "Save" bottom in the toolbar. Several image formats, such as png, jpg, and tiff, can be chosen in the save dialog, in addition to pdf. Figure 4 shows main, preference, and message windows of the GUI mode for the same data of Figure 2.

3.   Summary

In this paper, I introduced usages and examples of the script, UPbplot.py, which had developed in order to offer a new tool for calculation and visualization of U–Pb age data. It is an operating system-independent software and can deal with the conventional and Tera–Wasserburg diagrams with error ellipses of arbitrary confidence levels. It can calculate and plot the one- and two-dimensional weighted means, MSWDs, concordia ages, and concordia-intercept ages. This script provides an alternative tool to a well-known Visual Basic® add-in program for Microsoft® Excel® "Isoplot".
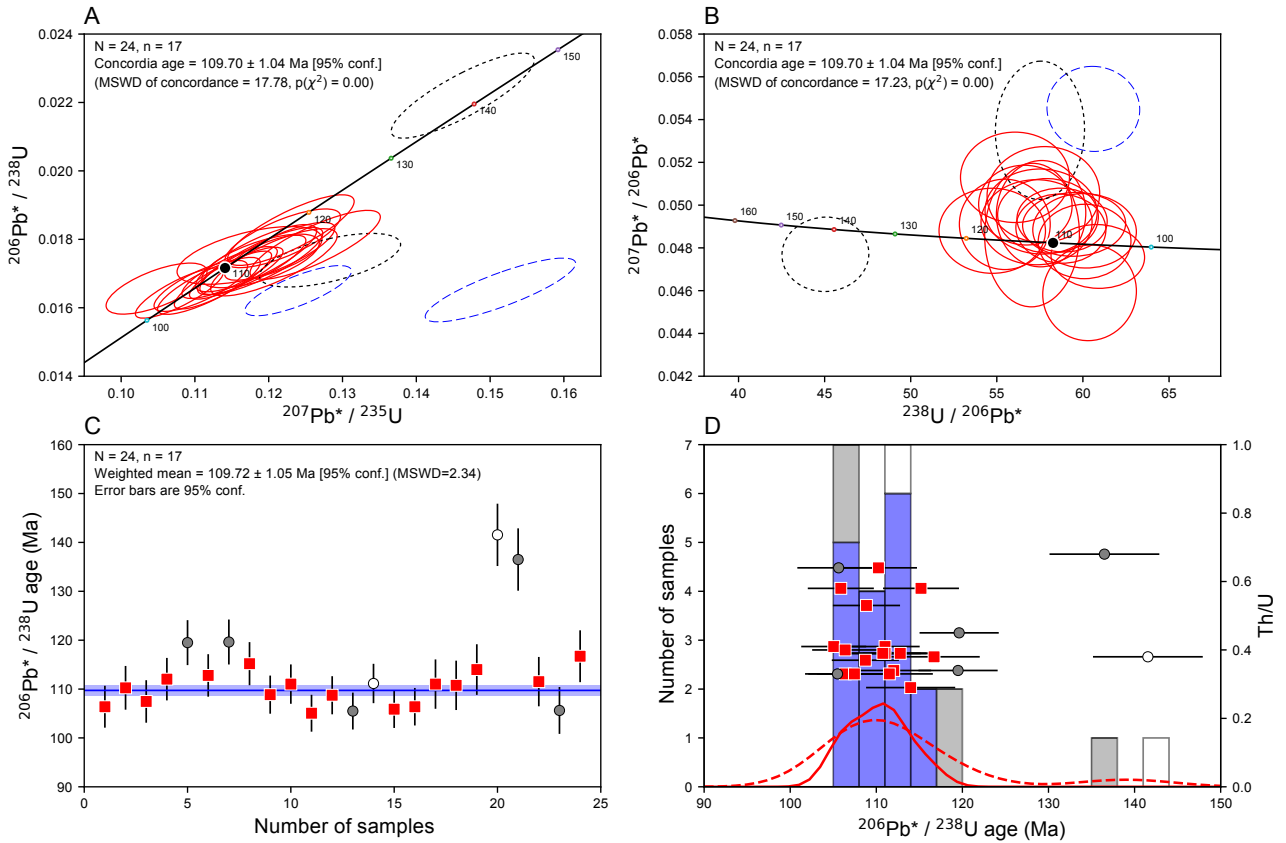
Figure 2   An example of output image derived from the same data with those of Figure 1. A: Conventional concordia diagram with error ellipses for 95% confidence regions of the measurements. Solid red, dashed blue, and dotted black ellipses are accepted, discordant, and manually excluded measurements from the calculation, respectively. A solid black circle on the concordia curve indicates the concordia age. *N* and *n* indicate numbers of total and accepted measurements, respectively. B: Tera–Wasserburg concordia diagram for the same legend with A. C: Bar plots of $^{206}Pb^*/^{238}U$ ages and their weighted mean (blue line) with its 95% confidence region (shaded band). Red squares, gray circles, and open circles with error bars are accepted, discordant, and excluded measurements, respectively. D: Histogram of $^{206}Pb^*/^{238}U$ age (left side of the vertical axis). Blue, gray, and, open boxes are accepted, discordant, and excluded measurements, respectively. Kernel density estimates of all (dashed red line) and accepted (solid red line) measurements are also illustrated. Th/U ratios (right side of the vertical axis) are indicated by the same symbol with C.

Appendix

A. 1   Decay constants

The following decay constants are used in the script, based on Jaffey *et al.* (1971), Steiger and Jäger (1977) and Hiess *et al.* (2012) (see Schoene, 2014).

$$\lambda_{238U} = 1.55125 \times 10^{-10} \quad [\text{year}^{-1}] \qquad \pm 0.107\% \quad (2\sigma)$$

$$\lambda_{235U} = 9.8485 \times 10^{-10} \quad [\text{year}^{-1}] \qquad \pm 0.137\% \quad (2\sigma)$$

$$\lambda_{232Th} = 4.9475 \times 10^{-11} \quad [\text{year}^{-1}] \qquad \pm \sim 1\% \quad (2\sigma)$$

$$\frac{^{238}U}{^{235}U} = 137.818 \qquad\qquad\qquad \pm 0.045 \quad (2\sigma)$$

A. 2   Concordia diagrams

Coordinates of *X* and *Y* for the conventional concordia diagram (Wetherill, 1956) are written as functions of time *t*,

$$X = \frac{^{207}Pb^*}{^{235}U} = \exp(\lambda_{235U}t) - 1 \qquad (A1)$$

$$Y = \frac{^{206}Pb^*}{^{238}U} = \exp(\lambda_{238U}t) - 1 \qquad (A2)$$

where asterisks denote radiogenic components. Coordinates of *x* and *y* for the Tera–Wasserburg concordia diagram (Tera and Wasserburg, 1972) can be expressed by using eqs. (A1)–(A2) and the constants in Appendix A.1.
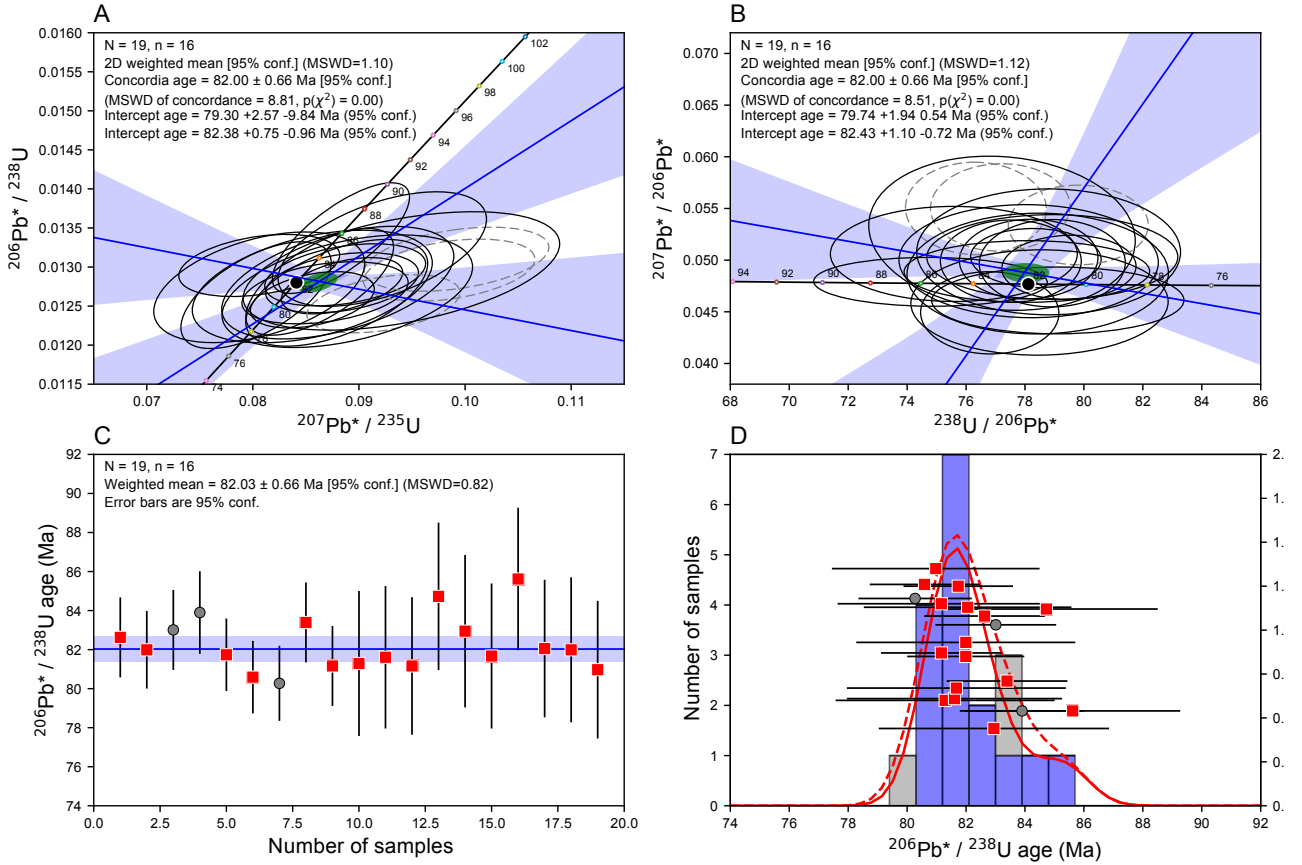
Figure 3 Another example of output image. A: Conventional concordia diagram with 95% confidence regions of the measurements. Solid and gray dashed ellipses are accepted and discordant data, respectively. Two-dimensional weighted mean (solid green ellipse), concordia age (solid black circle), two regression lines (thick blue lines) with the errors (shaded areas) are also plotted. B: Tera–Wasserburg concordia diagram for the same legend with A. C: Bar plots of $^{206}Pb^*/^{238}U$ ages. Symbols are same with Figure 2C. D: Histogram of $^{206}Pb^*/^{238}U$ age and Th/U ratios. Symbols are same with Figure 2D. The data come from sample 080122I01 in Iida *et al.* (2015).

$$x = \frac{^{238}U}{^{206}Pb^*} = \frac{1}{\exp(\lambda_{238_U}t) - 1} = \frac{1}{Y} \tag{A3}$$

$$y = \frac{^{207}Pb^*}{^{206}Pb^*} = \frac{^{235}U}{^{238}U}\frac{\exp(\lambda_{235_U}t) - 1}{\exp(\lambda_{238_U}t) - 1} = \frac{1}{137.818}\frac{X}{Y}. \tag{A4}$$

Because both coordinates of X and Y (x and y) are not independent each other, the covariance of X and Y (x and y) is needed to obtain confidence regions of the measurements, which is defined as

$$\mathrm{cov}(X,Y) \equiv \sigma_X \sigma_Y \rho_{XY} \tag{A5}$$

$$\mathrm{cov}(x,y) \equiv \sigma_x \sigma_y \rho_{xy} \tag{A6}$$

where σ_x and ρ_{XY} mean the standard deviation of X and the error correlation between X and Y, respectively.

For the calculation of the error correlations in eqs. (A5) and (A6), error propagation (Taylor, 1997) should be considered. As for $x = 1/Y$ from eq. (A3) and $y = uX/Y$ (u is a constant) from eq. (A4),

$$\sigma_x^2 = \left(\frac{\partial y}{\partial Y}\right)^2 \sigma_Y^2 = x^2 S_Y^2 \tag{A7}$$

$$\sigma_y^2 = \left(\frac{\partial y}{\partial X}\right)^2 \sigma_X^2 + \left(\frac{\partial y}{\partial Y}\right)^2 \sigma_Y^2 + 2\frac{\partial y}{\partial X}\frac{\partial y}{\partial Y}\mathrm{cov}(X,Y)$$

$$= y^2 \left(S_X^2 + S_Y^2 - 2S_X S_Y \rho_{XY}\right) \tag{A8}$$

where $S_x = \sigma_x/X$ and $S_y = \sigma_y/Y$ are relative errors in the measures. Then, eqs. (A7) and (A8) yield relative errors of

$$S_x^2 = S_Y^2 \tag{A9}$$

$$S_y^2 = S_X^2 + S_Y^2 - 2S_X S_Y \rho_{XY} \tag{A10}$$
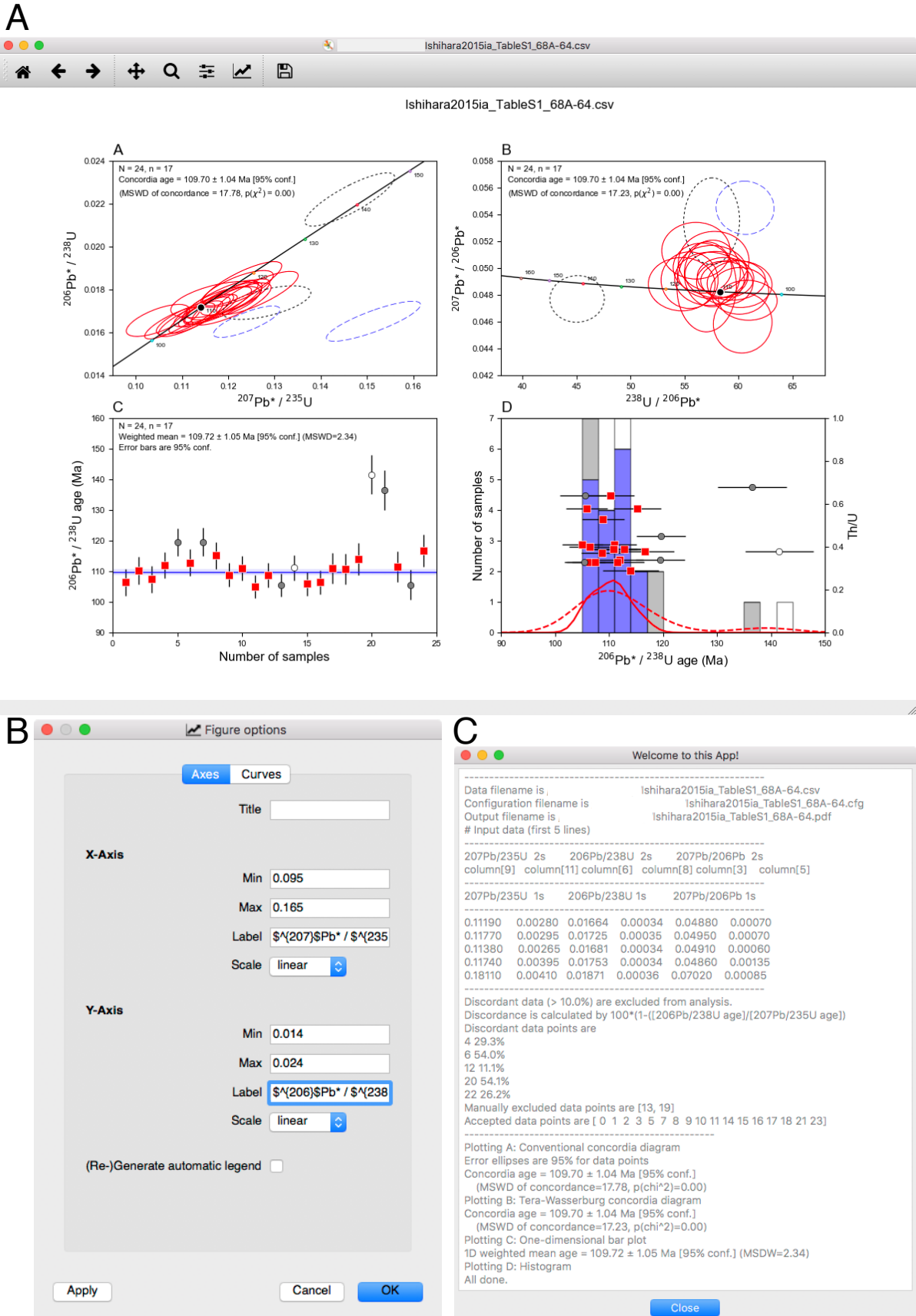
Figure 4   A collection of screenshots of the GUI mode. A: Main window of the diagrams. B: Preference panel to control ranges of axes and labels in the diagrams. C: Message window showing result of calculation. The U–Pb data are same with Figure 1.

where $S_x = \sigma_x/x$ and $S_y = \sigma_y/y$. For the inverse case of eq. (A8), $X = y/(ux)$, we obtain

$$S_X^2 = S_x^2 + S_y^2 - 2S_x S_y \rho_{xy}. \qquad (A11)$$

Therefore, the error correlations can be calculated from eqs. (A9)–(A11),

$$\rho_{XY} = \frac{S_X^2 + S_Y^2 - S_y^2}{2S_X S_Y} \qquad (A12)$$

$$\rho_{xy} = \frac{S_Y^2 - S_X S_Y \rho_{XY}}{S_x S_y}. \qquad (A13)$$

Please notice that eq. (A13) is different from the equation of ρ_{xy} in p. 27 of Ludwig (2012).

By using the covariances of eqs. (A5)–(A6) with error correlations of eqs. (A12)–(A13), we can draw error ellipses showing the two-dimensional "normally distributed" areas with certain confidences, especially 68% ($\approx 1\sigma$) and 95% ($\approx 2\sigma$).

A. 3　One-dimensional weighted mean

Weighted mean (weighted average) is a kind of mean with consideration of errors. For the one-dimensional case, the weighted mean is written as

$$\overline{X} = \sum_{i=1}^{N} \omega(X_i) X_i$$

where X_i is the measurement of the ith component of a total of N measurements, and $\omega(X_i)$ is weight of each measurement. The weight is an inverse square of the standard deviation σ_{X_i} divided by sum of them,

$$\omega(X_i) = (\sigma_{X_i})^{-2} \Big/ \sum_{i=1}^{N} (\sigma_{X_i})^{-2}.$$

Variance of the weighted mean is

$$\sigma_{\overline{X}}^2 = 1 \Big/ \sum_{i=1}^{N} (\sigma_{X_i})^{-2}$$

when each of the measurements are independent (McLean *et al.*, 2011).

If we use 95% confidence region of the weighted mean $\overline{X}$, it can be simply calculated by using $\sigma_{\overline{X}}$ times 1.96 (Student's t for an infinite sample size).

A. 4　Mean square of the weighted deviation (MSWD)

Mean square of the weighted deviation (MSWD) was originally developed for statistical evaluation of a regression line (e.g.,Wendt and Carl, 1991), which

indicates how well the line describes the data X_i. When a value of MSWD is less than 1, the observed deviations from the regression line are considered within analytical error. Otherwise, if it is more than 3, interpretation of such line may be doubtful. It is written as

$$\text{MSWD} = S \big/ df \qquad (A14)$$

where S is sum of "residual" that is sum of distances from each data point to the regression line (to the weighted mean for the one-dimensional case),

$$S = \sum_{i=1}^{N} \frac{(X_i - \overline{X})^2}{\sigma_i^2} \qquad (A15)$$

and df is degree of freedom, $N - 1$.

A. 5　Two-dimensional weighted mean

The two-dimensional weighted mean $(\overline{X}, \overline{Y})$ can be obtained by minimizing the sum of the squares of the N error weighted residuals (Ludwig, 1998) as,

$$\begin{aligned} S &= \sum_{i=1}^{N} v_i^T \Omega_i v_i \\ &= \sum_{i=1}^{N} \left(R_i^2 \Omega_i^{11} + r_i^2 \Omega_i^{22} + 2 R_i r_i \Omega_i^{12} \right) \end{aligned} \qquad (A16)$$

where v_i is a vector of residuals written as

$$v_i = \begin{pmatrix} X_i - \overline{X} \\ Y_i - \overline{Y} \end{pmatrix} = \begin{pmatrix} R_i \\ r_i \end{pmatrix} \qquad (A17)$$

and Ω_i is

$$\Omega_i = \begin{pmatrix} \Omega_i^{11} & \Omega_i^{12} \\ \Omega_i^{12} & \Omega_i^{22} \end{pmatrix} = \begin{pmatrix} \sigma_{X_i}^2 & \text{cov}(X_i, Y_i) \\ \text{cov}(X_i, Y_i) & \sigma_{Y_i}^2 \end{pmatrix}^{-1}. \qquad (A18)$$

Solving eqs. (A16)–(A18) gives $(\overline{X}, \overline{Y})$ that minimize S as

$$\overline{X} = \frac{\sum\limits_{i=1}^{N} \Omega_i^{22} \sum\limits_{i=1}^{N} (X_i \Omega_i^{11} + Y_i \Omega_i^{12}) - \sum\limits_{i=1}^{N} \Omega_i^{12} \sum\limits_{i=1}^{N} (Y_i \Omega_i^{22} + X_i \Omega_i^{12})}{\sum\limits_{i=1}^{N} \Omega_i^{11} \sum\limits_{i=1}^{N} \Omega_i^{22} - \left(\sum\limits_{i=1}^{N} \Omega_i^{12}\right)^2} \qquad (A19)$$

$$\overline{Y} = \frac{\sum\limits_{i=1}^{N} \Omega_i^{11} \sum\limits_{i=1}^{N} (Y_i \Omega_i^{22} + X_i \Omega_i^{12}) - \sum\limits_{i=1}^{N} \Omega_i^{12} \sum\limits_{i=1}^{N} (X_i \Omega_i^{11} + Y_i \Omega_i^{12})}{\sum\limits_{i=1}^{N} \Omega_i^{11} \sum\limits_{i=1}^{N} \Omega_i^{22} - \left(\sum\limits_{i=1}^{N} \Omega_i^{12}\right)^2} \qquad (A20)$$

Standard deviations of the means ($\sigma_{\overline{X}}$ and $\sigma_{\overline{Y}}$) are derived from eq. (9) in Ludwig (1998),

$$\sigma_{\overline{X}} = \sqrt{\frac{\sum_{i=1}^{N} \Omega_i^{22}}{\sum_{i=1}^{N} \Omega_i^{11} \sum_{i=1}^{N} \Omega_i^{22} - \left(\sum_{i=1}^{N} \Omega_i^{12}\right)^2}} \qquad (A21)$$

$$\sigma_{\overline{Y}} = \sqrt{\frac{\sum_{i=1}^{N} \Omega_i^{11}}{\sum_{i=1}^{N} \Omega_i^{11} \sum_{i=1}^{N} \Omega_i^{22} - \left(\sum_{i=1}^{N} \Omega_i^{12}\right)^2}}. \qquad (A22)$$

The MSWD can be calculated by eq. (A14) with S of eq. (A16) and the degree of freedom, $df = 2N - 2$.

A.6 Concordia ages
A.6.1 Conventional concordia curve

A point on the conventional concordia curve (X_c, Y_c) is expressed as a function of time t using eqs. (A1) and (A2). The vector of residuals v_i represents the difference between (X_c, Y_c) and each measurement (X_i, Y_i),

$$v_i = \begin{pmatrix} X_i - X_c \\ Y_i - Y_c \end{pmatrix} = \begin{pmatrix} R_i \\ r_i \end{pmatrix}. \qquad (A23)$$

The best t can be obtained, when the least sum of the weighted squared residuals of eq. (A16) with eqs. (A18) and (A23) is minimum. As mentioned in Ludwig (1998), the two-dimensional weighted mean of eqs. (A19)–(A20) and the standard deviation of eqs. (A21)–(A22) are practically used to calculate the minimum S and t for (X_c, Y_c). The least square method (the function of optimize. leastsq in SciPy) is applied in this script to calculate t to minimize S.

The variance in t is

$$\sigma_t^2 = \left(Q_{235}^2 \Omega^{11} + Q_{238}^2 \Omega^{22} + 2Q_{235}Q_{238}\Omega^{12}\right)^{-1}$$

where

$$Q_{235} = \lambda_{235U} \exp(\lambda_{235U}t)$$

$$Q_{238} = \lambda_{238U} \exp(\lambda_{238U}t)$$

$$\Omega^{11} = \sigma_{\overline{Y}}^2 \bigg/ \left(\sigma_{\overline{X}}^2 \sigma_{\overline{Y}}^2 - \mathrm{cov}(\overline{X},\overline{Y})^2\right)$$

$$\Omega^{22} = \sigma_{\overline{X}}^2 \bigg/ \left(\sigma_{\overline{X}}^2 \sigma_{\overline{Y}}^2 - \mathrm{cov}(\overline{X},\overline{Y})^2\right)$$

$$\Omega^{12} = -\mathrm{cov}(\overline{X},\overline{Y}) \bigg/ \left(\sigma_{\overline{X}}^2 \sigma_{\overline{Y}}^2 - \mathrm{cov}(\overline{X},\overline{Y})^2\right)$$

and

$$\begin{pmatrix} \sigma_{\overline{X}}^2 & \mathrm{cov}(\overline{X},\overline{Y}) \\ \mathrm{cov}(\overline{X},\overline{Y}) & \sigma_{\overline{Y}}^2 \end{pmatrix} = \begin{pmatrix} \sum_{i=1}^{N} \Omega_i^{11} & \sum_{i=1}^{N} \Omega_i^{12} \\ \sum_{i=1}^{N} \Omega_i^{12} & \sum_{i=1}^{N} \Omega_i^{22} \end{pmatrix}^{-1}.$$

Three MSWDs are considered for the concordia ages, which include the MSWD for X–Y equivalence that is sum of $S(X_i, Y_i)$ divided by $2N - 1$, the MSWD for concordance that is $S(\overline{X}, \overline{Y})$, and the MSWD for combined equivalence and concordance (p. 667 in Ludwig, 1998). The script outputs one of the MSWDs according to the settings in the configuration file.

A.6.2 Tera–Wasserburg concordia curve

Transformed ratios of (x_i, y_i), errors $(\sigma_{x_i}, \sigma_{y_i})$ and error correlation (ρ_{xy}) from the Tera–Wasserburg coordinate to the conventional coordinate (X_i, Y_i) are used to solve the concordia age on the Tera–Wasserburg curve (Ludwig, 1998). The best t and its standard deviation σ_t can be obtained by substituting $X_i = 137.818 y_i / x_i$ and $Y_i = 1/x_i$ from eqs. (A3)–(A4) with eqs. (A9), (A11), and (A13) into the procedures of the conventional concordia age (Appendix A.6.1).

A.7 Regression line by Maximum Likelihood Estimate (MLE)

The best fit line (X', Y') with the uncertainty can be expressed as Ludwig (1980),

$$Y' = a + bX' \pm \sqrt{\sigma_a^2 + \sigma_b^2 X'(X' - 2\overline{X})} \qquad (A24)$$

where a and b are intercept and slope, respectively, $\overline{X}$ is the centroid of measured data X, which can be calculated by the method of maximum likelihood estimate (York, 1969; Titterington and Halliday, 1979) of

$$\overline{X} = \sum_{i=1}^{N} Z_i X_i \bigg/ \sum_{i=1}^{N} Z_i$$

$$\overline{Y} = \sum_{i=1}^{N} Z_i Y_i \bigg/ \sum_{i=1}^{N} Z_i$$

where Z_i is

$$Z_i = \frac{\omega(X_i)\omega(Y_i)}{b^2\omega(Y_i) + \omega(X_i) - 2b\rho_{XY}\sqrt{\omega(X_i)\omega(Y_i)}}$$

with

$$\omega(X_i) = \sigma_{X_i}^{-2}, \; \omega(Y_i) = \sigma_{Y_i}^{-2},$$

and

$$\rho_{XY} = \text{cov}(X_i, Y_i)/\sigma_{X_i}\sigma_{Y_i}.$$

The best-fit line can be obtained, when

$$S = \sum_{i=1}^{N} Z_i(Y_i - bX_i - a)^2$$

is minimized. Because this equation cannot be solved explicitly, the MLE method is used to calculate the best b,

$$b = \frac{-B \pm \sqrt{B^2 + 4AC}}{2A}$$

where

$$A = \sum_{i=1}^{N} Z_i^2 \left(\frac{(X_i - \overline{X})(Y_i - \overline{Y})}{\omega(X_i)} - \frac{\rho_{XY}(X_i - \overline{X})^2}{\sqrt{\omega(X_i)\omega(Y_i)}} \right)$$

$$B = \sum_{i=1}^{N} Z_i^2 \left(\frac{(X_i - \overline{X})^2}{\omega(Y_i)} - \frac{(Y_i - \overline{Y})^2}{\omega(X_i)} \right)$$

$$C = \sum_{i=1}^{N} Z_i^2 \left(\frac{(X_i - \overline{X})(Y_i - \overline{Y})}{\omega(Y_i)} - \frac{\rho_{XY}(Y_i - \overline{Y})^2}{\sqrt{\omega(X_i)\omega(Y_i)}} \right).$$

Therefore, b has two solutions, meaning two lines are obtained.

The variances of a and b are given by

$$\sigma_a^2 = \sum_{i=1}^{N} X_i^2 Z_i \left/ \sum_{i=1}^{N} Z_i \sum_{i=1}^{N} (X_i - \overline{X})^2 Z_i \right.$$

$$\sigma_b^2 = 1 \left/ \sum_{i=1}^{N} (X_i - \overline{X})^2 Z_i. \right.$$

The concordia-intercept age is the age (t) at which the regression line of eq. (A24) intersects the concordia curve, meaning $|Y_c - Y'|$ is zero.

A. 8   Data rejection

Discordant data can be excluded from calculation of the weighted mean, concordia, and concordia-intercept ages. The script can choose one from among the following three methods to calculate the discordance (%).

$$\text{Discordance} = \left(1 - \frac{^{206}\text{Pb}^*/^{238}\text{U age}}{^{207}\text{Pb}^*/^{206}\text{Pb}^* \text{ age}} \right) \times 100,$$

$$= \left(1 - \frac{^{207}\text{Pb}^*/^{235}\text{U age}}{^{207}\text{Pb}^*/^{206}\text{Pb}^* \text{ age}} \right) \times 100, \text{or}$$

$$= \left(1 - \frac{^{206}\text{Pb}^*/^{238}\text{U age}}{^{207}\text{Pb}^*/^{235}\text{U age}} \right) \times 100$$

where

$$\frac{^{207}\text{Pb}^*}{^{235}\text{U}} \text{ age} = \frac{1}{\lambda_{235\text{U}}} \log\left(\frac{^{207}\text{Pb}^*}{^{235}\text{U}} + 1 \right)$$

$$\frac{^{206}\text{Pb}^*}{^{238}\text{U}} \text{ age} = \frac{1}{\lambda_{238\text{U}}} \log\left(\frac{^{206}\text{Pb}^*}{^{238}\text{U}} + 1 \right).$$

$^{207}\text{Pb}^*/^{206}\text{Pb}^*$age is the time t, when

$$\left| \frac{^{238}\text{U}}{^{235}\text{U}} \frac{^{207}\text{Pb}^*}{^{206}\text{Pb}^*} - \frac{\exp(\lambda_{235\text{U}}t) - 1}{\exp(\lambda_{238\text{U}}t) - 1} \right| = 0.$$

References

Bowring, J. and PI CIRDLES.org Open Source Development Team (2016) Topsoil: A community driven replacement for ISOPLOT. Apache License, Version 2.0, https://github.com/CIRDLES/topsoil, Topsoil v1.0.0-alpha.10 (accessed 2016-04-05).

Hiess, J., Condon, D. J., McLean, N. and Noble, S. R. (2012) ^{238}U/^{235}U systematics in terrestrial Uranium-bearing minerals. *Science*, **335**, 1610–1614, doi: 10.1126/science.1215507.

Hunter, J. D. (2007) Matplotlib: A 2D graphics environment. *Comput. Sci. Eng.*, **9**, 90–95, doi: 10.5281/zenodo.61948.

Iida, K., Iwamori, H., Orihashi, Y., Park, T., Jwa, Y.-J., Kwon, S.-T., Danhara, T. and Iwano, H. (2015) Tectonic reconstruction of batholith formation based on the spatiotemporal distribution of Cretaceous–Paleogene granitic rocks in southwestern Japan. *Island Arc*, **24**, 205–220, doi: 10.1111/iar.12103.

Ishihara, S. and Orihashi, Y. (2015) Cretaceous granitoids and their zircon U-Pb ages across the south-central part of the Abukuma Highland, Japan. *Island Arc*, **24**, 159–168, doi: 10.1111/iar.12105.

Jaffey, A. H., Flynn, K. F., Glendenin, L. E., Bentley, W. C. and Essling, A. M. (1971) Precision measurement of half-lives and specific activities of ^{235}U and ^{238}U. *Phys. Rev. C*, **4**, 1889–1906, doi: 10.1103/PhysRevC.4.1889.

Jones, E., Oliphant, T., Peterson, P. *et al*. (2001–) SciPy: Open source scientific tools for Python. http://www.scipy.org/ (accessed 2016-09-16).

Ludwig, K. R. (2012) *Isoplot 3.75: A geochronological toolkit for Microsoft Excel*, Spec. Publ., no. 5, Berkeley Geochronology Center, Berkeley, California, 75p.

Ludwig, K. R. (1980) Calculation of uncertainties of U-Pb isotope data. *Earth Planet. Sci. Lett.*, **46**, 212–220, doi: 10.1016/0012-821X(80)90007-2.

Ludwig, K. R. (1998) On the treatment of concordant Uranium-Lead ages. *Geochim. Cosmochim. Acta*, **62**, 665–676, doi: 10.1016/S0016-7037(98)00059-3.

McKinney, W. (2010) Data structures for statistical computing in Python. *In* van der Walt, S. and

Millman, J. eds. *Proceedings of the 9th Python in Science Conference*, 51–56.

McLean, N. M., Bowring, J. F. and Bowring, S. A.（2011）An algorithm for U-Pb isotope dilution data reduction and uncertainty propagation. *Geochem. Geophys. Geosyst.*, **12**, Q0AA18, doi: 10.1029/2010GC003478.

Noda, A. (2016) *UPbplot.py: A python script for U-Pb age data analysis*, Open-File Report, no. 634, Geol. Surv. Japan, AIST.

Schoene, B.（2014）U-Th-Pb Geochronology. *In* Rudnick, R. L. ed. *The Crust*. Treatise on Geochemistry, 2nd ed., **4**, Ch. 4.10, 341–378, Elsevier, Oxford, doi: 10.1016/B978-0-08-095975-7.00310-7.

SciPy.org (2016) scipy.stats.gaussian_kde. https://docs.scipy.org/doc/scipy/reference/generated/scipy.stats.gaussian_kde.html (accessed 2016-11-14).

Steiger, R. H. and Jäger, E.（1977）Subcommission on geochronology: Convention on the use of decay constants in geo- and cosmochronology. *Earth Planet. Sci. Lett.*, **36**, 359–362, doi: 10.1016/0012-821X(77)90060-7.

Taylor, J. R.（1997）*An Introduction to Error Analysis, 2nd ed.*, Ch. 9, 209–226, University Science Books, Sausalito, California, United States.

Tera, F. and Wasserburg, G. J.（1972）U-Th-Pb systematics in three Apollo 14 basalts and the problem of initial Pb in lunar rocks. *Earth Planet. Sci. Lett.*, **14**, 281–304, doi: 10.1016/0012-821X(72)90128-8.

Titterington, D. M. and Halliday, A. N.（1979）On the fitting of parallel isochrons and the method of maximum likelihood. *Chem. Geol.*, **26**, 183–195, doi: 10.1016/0009-2541(79)90045-7.

Wendt, I. and Carl, C.（1991）The statistical distribution of the mean squared weighted deviation. *Chem. Geol.*, **86**, 275–285, doi: 10.1016/0168-9622(91)90010-T.

Wetherill, G. W. (1956) Discordant uranium-lead ages. *Trans. Amer. Geophys. Union*, **37**, 320–326.

York, D.（1969）Least squares fitting of a straight line with correlated errors. *Earth Planet. Sci. Lett.*, **5**, 320–324, doi: 10.1016/S0012-821X(68)80059-7.

U–Pb 年代データのための新しい計算・可視化ツールの開発：UPbplot.py

野田　篤

要　旨

本稿は, U–Pb年代データの計算・可視化のために新しく開発したスクリプト（UPbplot.py）の使用方法と使用例及び数学的背景についての解説である. このスクリプトは, U–Pb年代値の1次元または2次元の加重平均, 標準（Wetherill）及び Tera–Wasserburg コンコーディア図におけるコンコーディア年代・コンコーディア曲線とのインターセプト年代を求めるための関数を含んでおり, それらの計算結果やコンコーディア図・棒グラフ・ヒストグラムなどのグラフを出力することができる.

地質調査総合センター研究資料集

地質調査総合センターの最新出版物

---

5 万分の 1 地質図幅	茂原・母島列島・新潟及び内野・播州赤穂
20 万分の 1 地質図幅	横須賀（第 2 版）・大分（第 2 版）・松山（第 2 版）
200 万分の 1 地質編集図	No. 4　日本地質図（第 5 版）
	No. 11　日本の火山（第 3 版）
特殊地質図	No. 12　富士火山地質図（第 2 版）
海洋地質図	No. 87　金華山沖表層堆積図（1:20 万）
	No. 88　見島沖海底地質図（1:20 万）
鉱物資源図	No. 7　南西諸島（1:50 万）
構造図	No. 14　全国主要活断層活動確率地図
火山地質図	No. 18　蔵王火山地質図（1:2.5 万）
	No. 19　九重火山地質図（1:2.5 万）
水文環境図	No. 9　富士山
空中磁気図	No. 46　養老断層地域高分解能空中磁気異常図
	No. 47　富士火山地域高分解能空中磁気異常図
重力図	No. 30　徳島地域重力図（ブーゲー異常）
	No. 31　京都地域重力図（ブーゲー異常）
	S3　甲府地域重力構造図（ブーゲー異常）
海外地球科学図	アジア鉱物資源図（1:500 万）
	東アジア地域地震火山災害情報図（1:1000 万）
海陸シームレス地質図	S-5　海陸シームレス地質情報集「駿河湾北部沿岸域」
燃料資源図	FR-3　燃料資源地質図「関東地方」
土壌評価図	E-6　表層土壌評価基本図　「茨城県地域」
数値地質図	G-16　20 万分の 1 日本シームレス地質図　DVD 版
	G-17　九州地質ガイド
	GT-4　全国地熱ポテンシャルマップ
	S-2　海陸シームレス地質情報集「新潟沿岸域」
	S-3　海陸シームレス地質情報集「福岡沿岸域」
	V-3　口永良部島火山地質データベース
	P-2　日本重力データベース　DVD 版
	G20-1　20 万分の 1 数値地質図幅集「北海道北部」第 2 版
	G20-2　20 万分の 1 数値地質図幅集「北海道南部」第 2 版
その他	日本の熱水系アトラス
	海と陸の地球化学図
	関東の地球化学図

BULLETIN
OF THE
GEOLOGICAL SURVEY OF JAPAN

Vol. 68　No. 3　2017

CONTENTS

Geological Survey of Japan, AIST